Analysis of nucleation kinetics in pH-shift crystallization using agitated and microfluidic systems.

Daniel Powell

Supervisors: **Jan Šefčik**, Joop ter Horst & Michele Zagnoni

Centre for Continuous Manufacturing and Advanced Crystallisation

Strathclyde Institute for Pharmacy and Biomedical Sciences

University of Strathclyde, Glasgow

December 12, 2023

Declaration

This thesis is the result of the authors original research. It has been composed by the author and has not been previously submitted for examination which has led to the award of a degree.

The copyright of this thesis belongs to the author under the terms of the United Kingdom Copyright Acts as qualified by University of Strathclyde Regulation 3.50. Due acknowledgement must always be made of the use of any material contained in, or derived from, this thesis.

Signed:

23 March 2023

Acknowledgements

Firstly, I would like to thank my supervisors, Prof Jan Šefčik, Prof Joop ter Horst and Dr Michele Zagnoni. Their wisdom, knowledge and support has been invaluable during this project.

It has been a delight to work in CMAC. Everyone has been incredibly encouraging, engaging and fun to work with. After being taken out of the office due to the COVID-19 pandemic shortly after starting; coming back, learning from and laughing with other researchers has been a joy; building my confidence and a passion for this field. In particular, I would like to thank Dr David McKechnie for his academic support and for sharing the experience from his own PhD and Dr Elke Prasad for performing the potentiometric titrations of DL-phenylalanine.

My family have been the Daniel driving force behind this thesis, motivating and encouraging me through it all. My Mum, who passed away this year, Dad, my beautiful wife, Louise and my two sons: Asher and Micah. Nothing motivates you to finish your PhD like two children who you have to support!

Soli Deo Gloria

Abstract

Crystal nucleation is a key event in the process of crystallization and is important in a number of processes in the pharmaceutical industry. Nucleation kinetics impact the crystal quality attributes of the product of a crystallization process. For example, increased crystal nucleation rate can lead to a smaller particle size distribution or increase the likelihood of presence of impurities or inclusions. A greater understanding of the fundamental principles underlying crystal nucleation allows for the development of better processes and tools for controlling this important element of crystallization.

The aim of this work was to study nucleation kinetics in pH-shift crystallization of the amino acid DL-phenylalanine (a model compound) through data generated from isothermal induction time experiments in small scale agitated vials and in a novel microfluidic device. The objectives were to gain a detailed understanding of the model system, to accurately determine solubility and supersaturation, collect nucleation rate data in the model system using an established methodology based on the Crystal16 multiple reactor system, develop a novel microfluidic device for collecting nucleation rate data and finally, to compare the nucleation rate data collected from the established and novel techniques.

In order to work in this complex system, a model was developed using MATLAB for predicting the pH and supersaturation from the solution composition and the dissociation constants for each component and applying the Davies extension of Debye-Huckel theory. This model was vital for designing experiments as it was not always possible to directly measure solution pH. Nucleation rates were estimated by fitting induction time data collected isothermally, under relevant conditions, to a cumulative probability distribution.

A microfluidic device was developed as a tool for induction time determination in a pH-shift crystallization system. The nucleation rates determined with this new technique were compared with data collected through a previously established methodology utilizing the Crystal 16 multiple reactor system. We report that nucleation in the microfluidic system behaves in a similar manner to other non-agitated systems with different regimes of nucleation kinetics: a non-nucleating regime, a slowly nucleating regime and a fast nucleating regime. As such, this type of data is best fitted to a double exponential curve. This behaviour is not yet fully understood, as agitated systems generally show a single nucleation regime, where induction time data can be fitted by a simple exponential curve. Therefore, it is not straightforward to directly compare nucleation rate obtained under agitated and non-agitated conditions. The microfluidic device presented can be used for non-agitated nucleation rate studies, however, further refinement of the design could improve control of crystallization conditions and extend its operational capacity and range.

Contents

3 pH Dependent Solubility of DL-Phenylalanine 25

4 The Study of DL-Phenylalanine Crystal Nucleation Kinetics Using a Small Scale Agitated Crystallizer 50

List of plots

Chapter 1

Introduction

1.1 Motivation

Crystallization is the process by which a new ordered solid phase is generated from a dissolved or disordered state. The molecules in a crystalline material are highly organised, comprising of a consistent, 3-dimensional structure organised around the crystal unit cell[1]. Crystallization plays a significant role in a variety of biological, environmental, and industrial processes. For instance, in geology, it is essential for the formation of minerals[2]. The process of water vapor turning into ice in the atmosphere is also a form of crystallization [3]. Moreover, in the field of medicine, ailments such as gall stones[4] and cataracts[5] can occur as a result of crystallization.

Within the pharmaceutical industry, crystallization holds great importance. It enables the production of highly pure and stable materials. Furthermore, advancements in understanding the crystallization process allow for process customization to achieve specific crystal quality attributes. The significance of crystallization is further emphasized by the fact that over 80% of pharmaceutical products contain a crystalline active pharmaceutical ingredient (API) [6].

Supersaturation is the state in which a solution contains more solute than the equilibrium solubility would allow under normal conditions. This is the key driving force for crystallization. Among the many techniques used to generate supersaturation for driving crystallization, pH-shift is one of the least commonly investigated and also among the least understood. Challenges related to determination of the supersaturation of a pH-shifted solution and the tight control required to achieve desired pH values make such systems challenging to work in. Studying crystallization kinetics in such a system can be done using cooling induced supersaturation at set pH values. While work has been published determining metastable zone width in an electrochemically induced, pH-shift system[7], a methodology for quantitatively measuring nucleation rate directly within a mixing-induced pH-shift crystallization has not previously been reported.

Microfluidic technology provides new tools for scientific investigation of crystallization processes. The ability to conduct hundreds of tightly controlled experiments simultaneously gives the opportunity to observe crystallization phenomena in a new and detailed way that is not accessible through traditional experimentation [8]. Crystal nucleation kinetics are a key phenomenon in the crystallization process and, yet, the quantitative understanding of nucleation is limited. Using microfluidics to study nucleation kinetics presents an exciting opportunity to gain new insight into this complex fundamental area. The application of microfluidics to pH-shift crystallization for the study of nucleation kinetics has not been previously reported.

1.2 Aims and Objectives

This work aims to develop new methodologies for the quantification of crystal nucleation rates utilizing microfluidic devices to study pH-shift crystallization. pH shift crystallization was chosen as a model system for study due to the importance of such systems in an industrial context and the challenges of pH control, prediction and resultant crystallization process design.

In order to achieve this it is necessary to develop predictive tools for quantifying the solubility and supersaturation of solutions. Utilizing the dependence of solubility on pH to control crystallization presents a complex problem. Supersaturation, a commonly used approximation of the driving force of crystallization, is dependent on both solubility and solution species distribution, which changes as the pH changes. Chapter 3 aims to develop a model for predicting a solution's pH and speciation, without requiring direct measurement, from solution composition information, utilizing pKa as a semi-empirical fitting parameter. The model will be validated with experimentally collected pH and solubility data.

The objective of Chapter 4 is to gain reference data for nucleation kinetics with an established methodology. Probability distributions of induction times obtained using cooling induced supersaturation will be used to calculate nucleation rates for DL-phenylalanine at different pH values. Using the Crystal16 Multiple Reactor System, the metastable zone will be charted in detail through a set pH range, establishing the metastable zone limit and the region by which nucleation rates can be gathered using this method.

Chapter 5 seeks to develop a microfluidic device for the collection of nucleation rate data. The device will mix high pH solution and low pH solution in situ to form $\tilde{1}$ nl droplets before storing for observation of onset of crystal nucleation.

Chapter 6 will utilize the microfluidic device developed to acquire induction times obtained using mixing induced supersaturation. These will be used to calculate nucleation rate data which will be analyzed and compared with the data obtained from agitated vial experiments at corresponding pH values (chapter 4).

Chapter 2

Background

2.1 Crystallization Overview

2.1.1 What is Crystallization?

Crystallization is a widely used industrial process for phase separation of solid from liquid. It is utilised in the manufacture of many modern products from simple table salt to the fine chemicals used in the pharmaceutical industry. Crystallization is largely used as a purification process, resulting in near pure, crystalline product through the processes of crystal nucleation, growth and agglomeration [9].

2.1.2 Crystallization Driving Force

The crystal driving force is a widely discussed topic in various academic resources [9][10]. Crystallisation is the phase separation of a solid crystalline material from a solution of solvent and dissolved material. For such a solution to be stable it must reside in the state of lowest Gibbs free energy. At equilibrium the free energy of the solution μ must be equal to the free energy of the solution when saturated with respect to the crystal solid phase μ^*. Therefore, the driving force of crystallisation can be described as the difference in the chemical potential of μ and μ^*.

$$\Delta\mu = \mu - \mu^* \tag{2.1}$$

When a solution is saturated, $\Delta\mu$ is zero and therefore the solution is stable. If the solution has a lower concentration than saturation the difference in chemical potential is negative and dissolution can occur from the solid into the liquid phase. Conversely, when the concentration of solution is greater than saturation, the potential difference is positive, allowing crystallisation to occur. The chemical potential for a solution can be calculated from the standard potential, μ_0, the activity, a, of the solution (or $a*$ for the saturated solution), the universal gas constant and the absolute temperature, T:

$$\mu = \mu_0 + RT\ln(a) \tag{2.2}$$

$$\mu^* = \mu_0 + RT\ln(a^*) \tag{2.3}$$

Combining equations 2 and 3 gives the dimensionless fundamental driving force of crystallisation:

$$\frac{\Delta\mu}{RT} = \ln\left(\frac{a}{a^*}\right) = \ln(S) \tag{2.4}$$

Where S is the supersaturation of the solution.

$$S = \exp\left(\frac{\Delta\mu}{RT}\right) \tag{2.5}$$

While activity is the fundamental driver of crystallization, it is often approximated with concentration. Therefore, the difference in concentration, ΔC, between the solution concentration, C, and the saturation concentration, C^*, is used to describe the driving force.

$$\Delta C = C - C^* \tag{2.6}$$

As a result, the supersaturation, S, which is determined from the concentration of the solution and the saturation concentration (Eq. 2.7) can also be used to represent the crystal driving force.

$$S = \frac{C}{C^*} \tag{2.7}$$

Rather than by S, the driving force of the solution is often alternatively quantified by the relative supersaturation, σ[11]:

$$\sigma = S - 1 \tag{2.8}$$

2.1.3 Solubility and Supersaturation

The solubility of a crystalline compound is an essential factor in the design of crystallization processes. Solid-liquid equilibrium occurs when a compound which is in the solid state is in contact with a solution of that compound which is saturated with respect to the solid phase, i.e. the solution concentration is equal to the solid phase solubility at given conditions. The nature of this equilibrium is determined by numerous factors including most significantly: temperature and solvent composition.

The solubility of a compound varies depending on the solvent used. Water is often a preferred solvent due to its ubiquity and its ability to dissolve a large number of different chemical compounds. Organic solvents frequently used include lower alcohols, ketones, esters and light alkanes, among others. Mixed solvents can be used to produce different effects on the crystallization process and crystal product quality attributes, most notably, changes in solubility.

The Van't Hoff equation is used to describe the relationship between mole fraction solubility at certain temperature T (Eq. 8)

$$\ln x = \frac{\Delta H}{R}\left(\frac{1}{T_m} - \frac{1}{T}\right) \tag{2.9}$$

The Van't Hoff equation describes ideal solubility behaviour through the heat of fusion ΔH and the melting temperature T_m. When used with a small range of temperatures, this equation can be used empirically by fitting ΔH and T_m. However, the non-ideality of the system causes fitted values to deviate from the actual heat of fusion and melting temperature leading to poor fits at larger temperature ranges[10].

In the context of crystallization, solubility can be easily described through the use of a phase diagram for a given solute - solvent system (Figure 2.1). Below the binodal, or solubility line

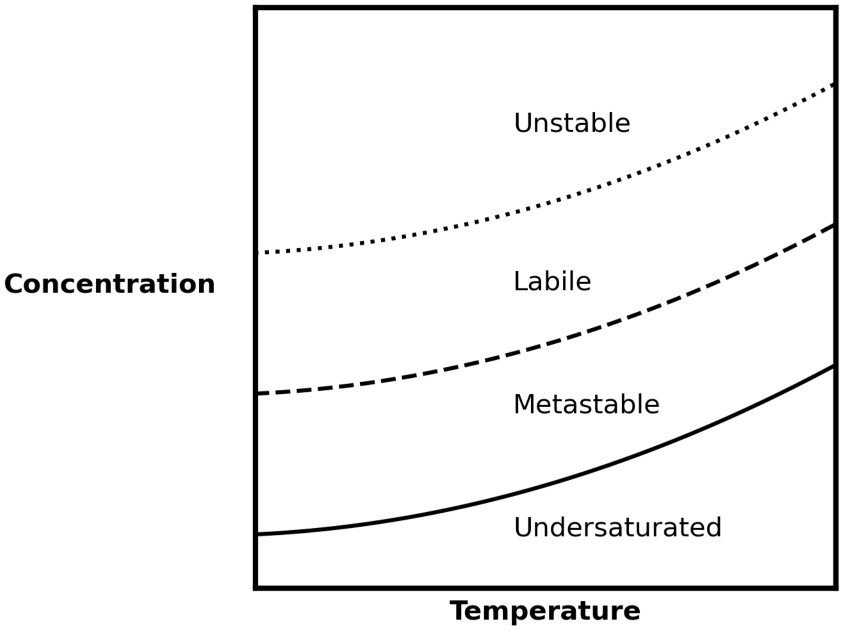

Figure 2.1: Example phase diagram showing the binodal or solubility line between undersaturated and supersaturated, the dashed line representing the metastable zone limit, and the dotted line representing the spinodal line.

solutions accept more solute and no crystallization will occur. Solutions in the metastable region are supersaturated but the driving force is insufficient to immediately overcome the energy barrier to form nuclei. Given enough time, nuclei will form and growth will occur, returning the solution to thermodynamic equilibrium at the binodal. Within the labile zone nucleation is immediate and this line represents the upper limit of the metastable zone. Above the spinodal line, the system is thermodynamically unstable and spinodal decomposition occurs here, however, this is unlikely to occur in cooling crystallization systems of small molecules before nucleation and growth occurs, although it is more common in anti-solvent systems, where it leads to oiling out by liquid-liquid phase decomposition.

2.1.4 Supersaturation generation

Supersaturation is an effective approximation for the crystal driving force. Generating supersaturation is essential to any crystallization process and there are various techniques for doing this.

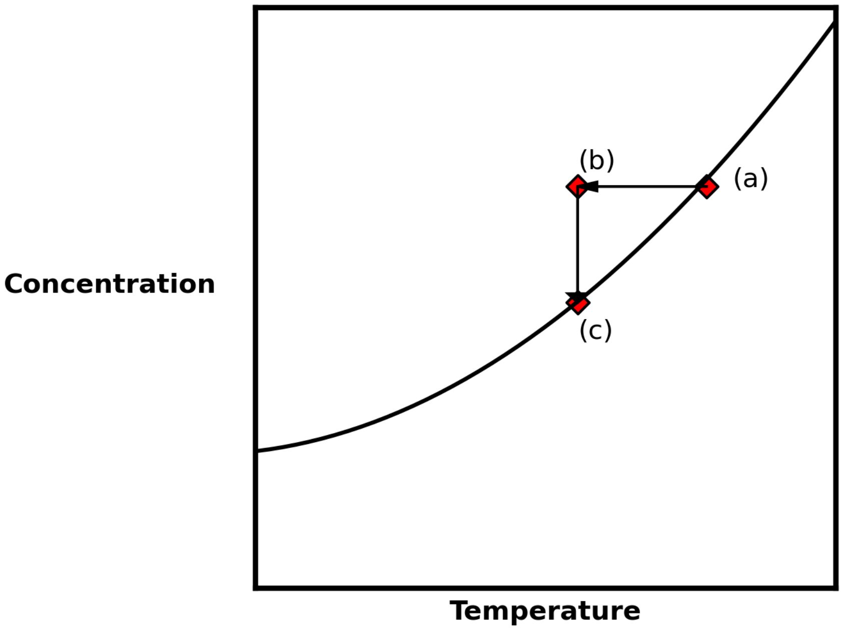

Figure 2.2: Example phase diagram showing the generation of supersaturation by cooling. (a) represents the initial solution composition and temperature. (b) is the cooled solution which is supersaturated. (c) is the final equilibrium solution composition and the solubility at the lower temperature.

Cooling crystallization, used in systems where the solubility has a large degree of dependence on temperature, is one of the most common techniques for generating supersaturation. A solution which is saturated or near saturated at high temperature (Figure 2.2 (a)) and cooling to a lower temperature where the solution concentration is now greater than the solubility (Figure 2.2 (b)). This method is not effective in solute - solvent systems where solubility is not strongly related to temperature. In such systems an alternative method that is commonly used is evaporative crystallization. In this type of system the solvent is removed from the solution by evaporation, causing an increase in the solution concentration, eventually exceeding the solubility and generating supersaturation (Figure 2.3).

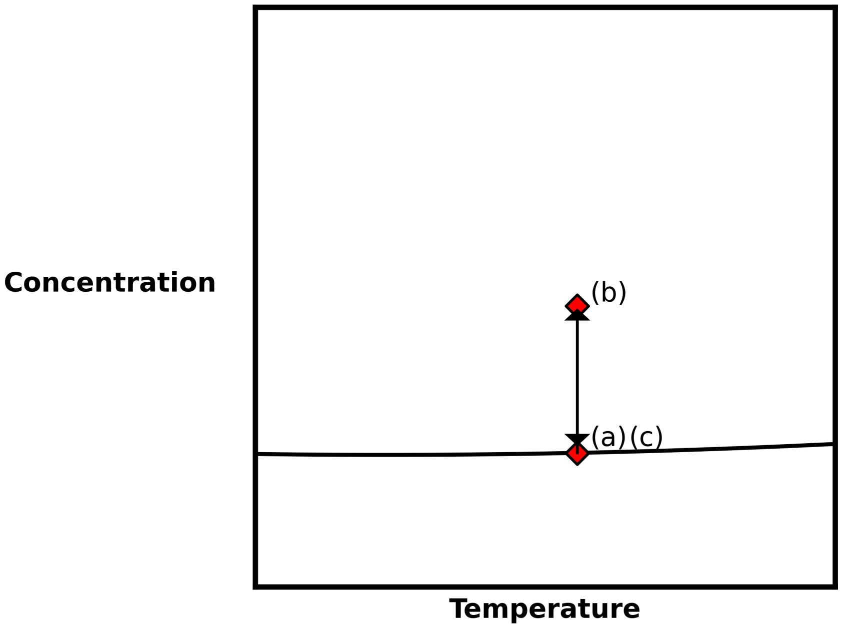

Figure 2.3: Example phase diagram showing the generation of supersaturation by evaporation. (a) represents the initial solution composition. (b) is the supersaturated solution after solvent has evaporated at which point nucleation or seeding occurs. (c) is the original solution concentration, however, at a lower volume of solvent and lower mass of solute which has been removed as crystallized product.

Antisolvent crystallization (Figure 2.4) is commonly used for generating supersaturation, relying on the difference of solubilities of a compound in different solvent. A solvent with much lower solubility than another can be treated as an antisolvent. By adding a miscible antisolvent to a saturated solution the effective solubility of the system is reduced, generating supersaturation. However, the addition of more solvent to a solution dilutes the solvent, creating a slightly more complex system where dilution must be taken into account. Antisolvent crystallization is only viable where the difference in solubility at a given antisolvent fraction is greater than the decrease in concentration due to dilution.

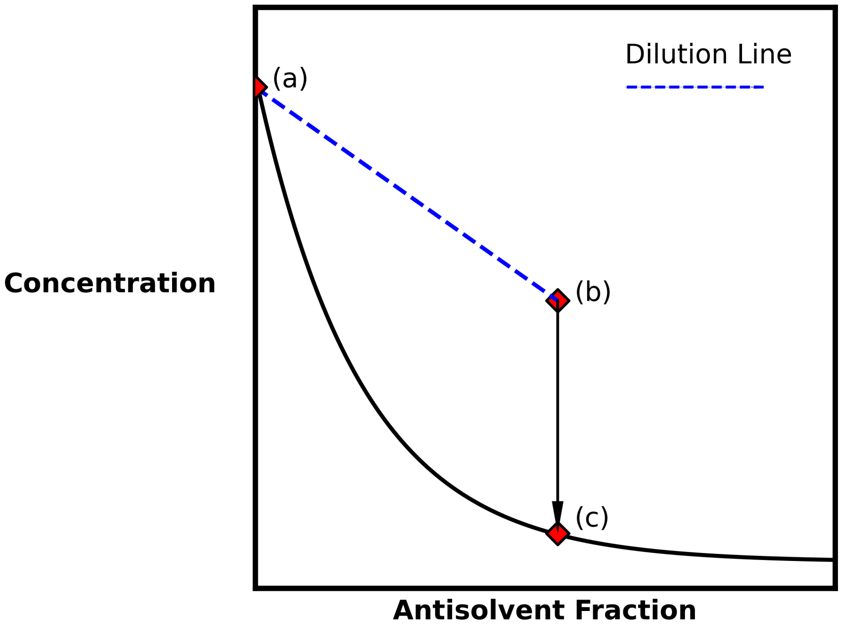

Figure 2.4: Example phase diagram showing the generation of supersaturation by antisolvent addition. As antisolvent fraction increases the solubility decreases (although, in some systems, a small amount of antisolvent can enhance solubility). (a) represents the initial solution composition at 100% solvent. (b) is the supersaturated solution after antisolvent has been added, at which point nucleation or seeding occurs. Dilution is seen by the decrease in concentration. (c) is the final solution concentration after crystallization is complete.

Another, relevant method for generating supersaturation is reactive crystallization. Reactive crystallization is where the progress of a chemical reaction changes the conditions in a solution that leads to the generation of supersaturation and the precipitation of crystals. One example of this is pH-shift crystallization (Figure 2.5). For solutes that are weak acids or bases their molecules become more dissociated as the pH of the solution reaches the extremities of the range (see section 3.3.3). The neutral species will have the lowest solubility and dissociated ions will have a much greater aqueous solubility[12]. If such a solution of dissociated ions is brought to neutral pH via a neutralization reaction the dissociated ions will be forced to associate forming either the neutral species, which will then be supersaturated, or form a salt which may be less soluble than the free ions.

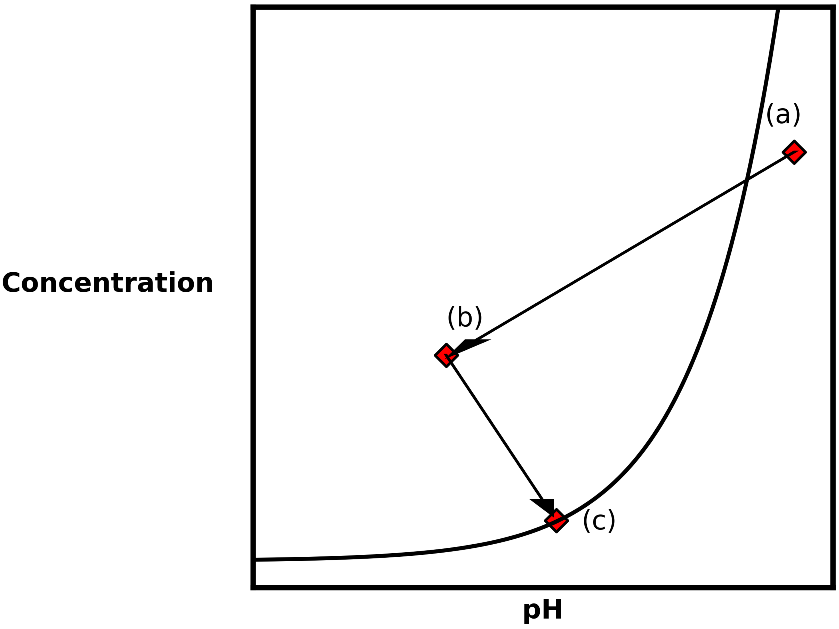

Figure 2.5: Example phase diagram showing crystallization by pH shift. In the example given the solute would be a weak acid, contributing H+ ions to the solution. (a) represents the initial solution composition high pH, high dissociation of the solute and therefore, high solubility. (b) is the supersaturated solution after the addition of neutralizing agent. At this point nucleation or seeding occurs. After crystallization the solute is removed from the solution, removing H+ ions and causing pH to increase. The final solution concentration is observed at (c) after crystallization is complete at a higher pH than crystallization originally occurred.

The practical application of this type of crystallization can behave in a manner similar to anti-solvent crystallization. In order to cause the pH change that initiates crystallization, a reactant, a neutralizing agent must be added to the solution, causing dilution. In addition to this, there is an added complication when crystallization occurs. Crystallization leads to the removal of solute from the system. That solute in solution is potentially contributing or removing hydrogen ions from the solution. The removal of said solute will cause the pH to change relative to the pH at the point of crystallization which in turn affects the solubility. This creates a complex system where the resulting pH needs to be measured or predicted using suitable solution equilibrium models.

2.2 Nucleation

Nucleation is the formation of new crystalline particles from a supersaturated solution. It has key effects on various crystal product quality attributes including polymorphism and particle size distribution[13]. Polymorphism is the structure in which the crystal molecules align themselves and is primarily determined at the point of nucleation. Particle size distribution can be affected by nucleation rate as a a large nucleation rate will dominate any growth and will lead to a larger number of smaller particles, while slower nucleation will lead to fewer, larger particles. The nucleation of new crystals is divided into two categories: primary and secondary. Primary nucleation occurs in the absence of crystalline material of a given substance and is the main focus of this work. It is defined as the moment of phase separation of a new solid phase from a liquid solution. It is stochastic and spontaneous but relies on sufficient driving force to overcome nucleation energy barriers. Primary nucleation can occur as heterogeneous or homogeneous nucleation. Heterogeneous nucleation occurs at foreign surfaces, particles and interfaces within a solution. These sites reduce the energy barrier to nucleation. Homogeneous nucleation occurs in the bulk of the supersaturated solution (Figure 2.6). Secondary nucleation only occurs if parent or seed crystals are present in the solution. This can happen once initial crystals have been formed by primary nucleation or through the addition of seed crystals.

2.2.1 Primary Nucleation

There are many theories as to how primary nucleation occurs: the classical nucleation theory (CNT) being the most prominent. CNT is the common framework under which the nucleation mechanism is understood. It posits that through random fluctuations within a solution, pre-

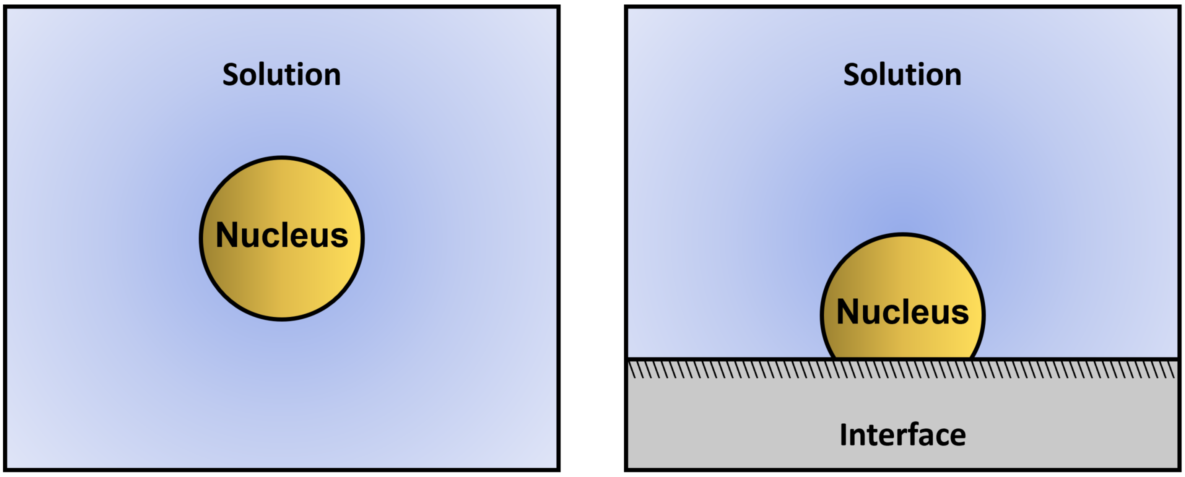

Figure 2.6: The left image displays homogeneous nucleation occuring in the bulk of a solution. The right features heterogeneous nucleation with a reduced surface area in contact with the surrounding solution of a nucleus forming on a surface.

nucleation crystalline clusters form. If a cluster is of a sufficiently large size to overcome the energy barrier to nucleation it will form a nucleus and grow into a crystal. If a cluster does not meet this critical size, it will be more favourable to return to the solution. The two-step mechanism of nucleation[14] is an example of a non-classical nucleation theory. It theorises that nucleation occurs in two steps, the formation of a dense droplet of metastable liquid within the solution. The molecules within the droplet then become ordered which produces the crystal nucleus.

2.2.2 Classical Nucleation Theory

The classical nucleation theory is well described in numerous textbooks[1][10]. According to this theory molecules within the bulk solution spontaneously begin to cluster together. Indeed, even within a solution at equilibrium the molecules will cluster together through random fluctuations of density. The theory postulates that clusters that exceed a certain critical size will form into a nucleus, while clusters below that size will dissolve back into solution. The formation of a cluster of molecules in the new phase requires a change in free energy, ΔG. This is given by the sum of

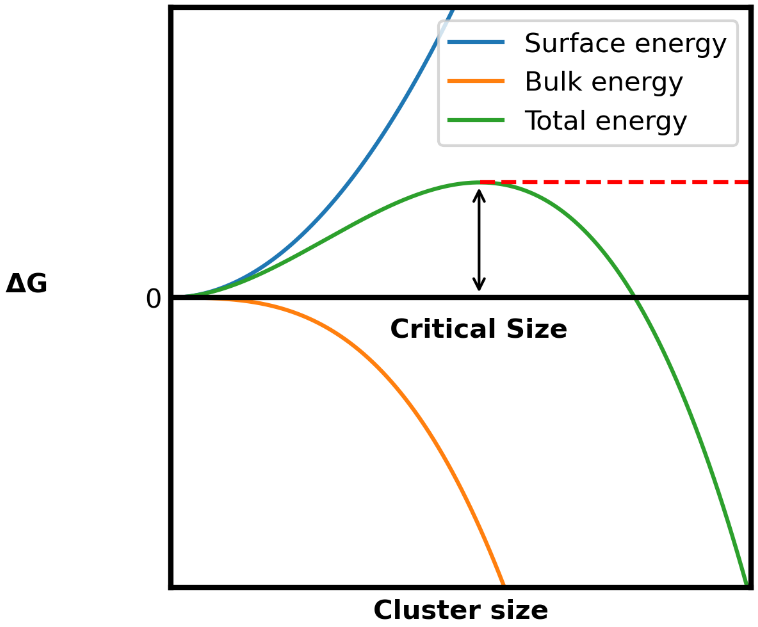

Figure 2.7: The free energy associated with the formation of a new critical nucleus as cluster size increases.

two terms: the free energy gained by the transfer of molecules out of the supersaturated phase into a new phase ($-n\Delta\mu$) and the free energy required to form a new interface between the new particle and the mother liquor (θ). This is expressed by:

$$\Delta G = -n\Delta\mu + \theta \tag{2.10}$$

where n is the number of molecules in a cluster. Alternatively expressed as:

$$\Delta G_{total} = \Delta G_{bulk} + \Delta G_{surface} \tag{2.11}$$

The critical nucleus size is reached at the point of maximum ΔG. As the size of a pre-nucleic cluster increases the energy gain from the bulk increases. Similarly, as the size of the cluster increases the surface area of that cluster too grows leading to a larger energy requirement to form the interface. However, the bulk energy is directly proportional to the volume. Assuming a spherical cluster:

$$\Delta G_{bulk} \propto \frac{4}{3}\pi r^3 \tag{2.12}$$

while the surface energy increases proportionally to the surface area:

$$\Delta G_{surface} \propto 4\pi r^2 \tag{2.13}$$

The bulk energy term is initially smaller than the surface energy term and so, when the size of a cluster is very small the interface energy will exceed that of the bulk energy. In a cluster with greater number of molecules, the surface energy will be greater than a smaller cluster but the bulk energy will be greater still. This principle will apply regardless of the form of the cluster. A critical point is reached when the cluster size is subject to the greatest net free energy loss. The free energy barrier is indicated by the red-dashed line in Figure 2.7. This is in effect a tipping point. Addition of a single molecule to such a cluster will cause it to have a lower ΔG than the critical nucleus size and therefore it will only grow from that point on as there is no driving energy for it to lose molecules (Figure 2.7).

Nucleation can be enhanced by the presence of surfaces in contact with a supersaturated solution. A surface, such as the walls of the crystallizing vessel, can provide a site for nucleation. The surface will reduce the surface area of the cluster (Figure 2.6) and therefore the surface energy will be reduced. This results in a smaller barrier to nucleation and a lower critical nucleus size, leading to faster nucleation than in a purely homogeneous system. In addition the form of the surface can have deeper impacts on the types of crystal formed [15] and recent work has shown that template particles can control and enhance nucleation rate [16].

According to CNT the nucleation rate can be determined by the following equation [10]

$$J = v \times Z_n \exp\left(\frac{-G^*}{k_B T}\right) \tag{2.14}$$

where v is the rate of attachment of molecules to a cluster, Z_n is the Zeldovich factor, which accounts for the width of ΔG, n is the number density of molecules in the solution and k_B is the Boltzmann constant. However, experiments have shown that CNT can overestimate J by many orders of magnitude [14]. The two step nucleation theory attempts to address this reported discrepancy and proposes an alternative mechanism to nucleation.

The Two-Step Theory

The two-step theory states that there are three phases involved in nucleation. A dilute solution phase, a crystal phase and a phase in between called the dense liquid phase. It is within the dense liquid phase that the molecules orient themselves and form into a crystal. The two-step theory proposes an alternative equation for nucleation rate[14] however, there is no consensus as yet on which theory is appropriate for which systems[17].

Recent investigations into this theory have applied classical nucleation theory to a two-step nucleation process. In this model, the pre-nucleic cluster described by the classical theory forms a composite with the metastable, dense liquid cluster. The master equation of the classical nucleation theory is applied to the composite-cluster model; finding that, with a degree of generalization, CNT provides a suitable mathematical framework for describing the two-step process [18], producing a master equation for calculating nucleation rate in a two-step nucleating system [19].

2.2.3 Experimental Methods for Nucleation Rate Determination

In the classical theory of nucleation the nucleation event occurs simultaneously with the generation of supersaturation. However, there is always a period of time between this moment and the detection of crystals in a solution. The solution in this state is said to be metastable. Experimental conditions for nucleation rate determination can be polythermal, where the solution is cooled at constant rate until crystals are detected, or isothermal, where a solution is held at constant temperature throughout[20].

In the case of cooling crystallization, the metastable zone width (MSZW)[21], is the difference between the temperature of solid-solution equilibrium solubility for a given concentration and the temperature at which nucleation occurs[22]. Under isothermal conditions, induction time is measured. Induction time is defined as the time difference between the generation of supersaturation and the detection of crystals. This can be defined according to the equation:

$$t_{ind} = t_r + t_n + t_g \tag{2.15}$$

where t_r is the time to reach a steady state distribution of pre-nucleation clusters, t_n is the nucleation time required for the formation of crystal nuclei and t_g, the time taken for crystals to grow to detectable size [1]. Detection of crystals is of key importance to both polythermal and isothermal experiments[23]. Critical nuclei can be composed of as few as tens of molecules [24] and the detection of such nuclei in a convenient way is beyond the limitations of current technology. It is therefore inevitable that a time-lag will occur between the moment of nucleation and the moment of detection. The duration of that time-lag is of critical importance to measurement of MSZW and induction time. Detection can be carried out by numerous analytical methods of variable minimum detection limits. Detection can occur via image analysis through tools such as particle vision measurements or optical microscopy; detection of the first crystal methods such as light transmission in the Crystal16 or focused beam reflectance measurement; or through detection of changes in solution composition using spectroscopic techiniques such as FTIR or Raman spectroscopy.

A variety of polythermal and isothermal techniques for determining nucleation rate have been proposed based on differing theories of how nucleation occurs[20]. Of particular interest to this work is the isothermal method in stirred microvials proposed by Jiang and Ter Horst [25]. The method posits that the probability of a nucleus being detected at time t can be found by taking the ratio of experiments in which a crystal has been detected before time t:

$$P(t) = \frac{M^{+}(t)}{M} \tag{2.16}$$

The stochastic nature of nucleation links the nucleation rate to the number of nuclei formed in a period of time given a certain volume.

$$N = JVt \tag{2.17}$$

Models have been developed to extract the nucleation rate from the variability, with the Markovian Poisson description being the most commonly used:

$$P(t) = 1 - exp\left(-JV(t - t_g)\right) \tag{2.18}$$

When the probability of nucleation at time t acquired from equation 2.16 is fitted to this model, the nucleation rate can be determined. This method has limitations. For the data collected to be optimally fitted to collect nucleation rate there ought to be at least 80 induction time measurements recorded, which can be time consuming. However, alternative methodologies such as maximum likelihood estimation have been shown to produce adequate fitting with as few as 5 nucleation observations [26]. In addition, the time for crystals to be detected is subject to the growth rate and the mechanism by which a new crystal is detected.

2.3 Microfluidics Overview

In order to develop microfluidic systems for use in crystallization it is essential to understand some of the key physical concepts that underpin microfluidic flow, particularly the difference between fluid flow at microscale compared to that at macroscale. Fluid flow can be characterised using a dimensionless number: the Reynolds number (Re) and is defined as the ratio of inertial forces to viscous forces expressed in the following equation:

$$Re = \frac{\rho v L}{\mu} \tag{2.19}$$

where ρ is the fluid density (g/cm^3); v is the velocity (cm/s); L is the diameter of the channel (cm) and μ is the dynamic viscosity of the fluid (g/cm $\cdot$ s)[27]. Inertia is the resistance of an object to changes in velocity. Viscosity is a measure of a fluid's ability to resist deformation due to shear or tensile stress.

Three different flow regimes can be distinguished from Re: If $Re < 2300$, the flow is laminar. If $2300 < Re < 4000$, the flow is in transition between laminar and turbulent. If $Re > 4000$, flow is fully turbulent.

Due to the small size of microfluidic devices, flow is always laminar. Flow velocity rarely exceeds 1 cm s^{-1} and microchannels have a diameter that seldom exceed 100 μm which results in very low inertial forces. This leads to a Reynolds number that rarely exceeds 10^{-1}. Far below the threshold of laminar and transitional flow. Low inertial forces allow greater control of fluid flow.

One of the major advantages of microfluidic devices (also referred to as “lab-on-chip” devices) is that they can be fabricated using photo- and soft-lithography techniques, allowing for rapid prototyping of new devices. This allows quick changes to be made to devices in order to adapt to new situations and compounds. Such devices are fabricated using polymers. Among the most popular of these is polydimethylsiloxane (PDMS). Some of the valuable qualities of PDMS include compatibility with many solvents and oils, optical transparency and low cost.

2.3.1 Droplet Microfluidics

Droplet microfluidics presents an interesting environment for the study of crystallization [8]. Droplets can be used to implement a micro-batch method of crystallization. This technique utilises the formation of a micron-sized emulsion of two immiscible fluids: one continuous phase and a dispersed phase. Micro-batch crystallization involves dissolving crystalline material and any precipitating agents in an aqueous solution which is then dispersed in an oil continuous phase. If stored correctly, these droplets are effectively isolated from one-another, each becoming a batch reactor for an experiment to be performed in. This allows for a large number of simultaneous experiments under almost identical conditions.

2.3.2 Droplet Formation

T-junctions are a well established geometry which can be used to form droplets[28]. A T-junction is comprised of a main channel containing the continuous phase and a perpendicular channel containing the phase for dispersal. At the junction where these two channels interface the tip of the dispersed phase flows into the continuous phase stream. As the flow of the dispersed phase continues into the main channel it blocks the flow of the continuous phase. This restriction causes an increase in upstream pressure of the continuous phase, causing the neck of the dispersed to thin out and finally break off, forming a droplet encapsulated in the continuous phase. However, for this to occur the capillary number must exceed a critical value.

The capillary number is dimensionless and is calculated by:

$$Ca = \frac{\mu v}{\gamma} \tag{2.20}$$

Where μ is the dynamic viscosity of the continuous phase (expressed in Pa s); v is the velocity of the continuous phase (expressed in m s^{-1}) and γ is the interfacial tension between to the two phases (expressed in n m^{-1}). The capillary number relates directly to the extent of deformation in the droplet interface and therefore influences droplet size [29].

Droplet size is influenced by other factors, including the junction aperture, the surface functionalisation, the ratio of channel widths and the ratio of flow rates. The flow rate ratio (Q') is calculated by:

$$Q' = \frac{Q_o}{Q_w} \tag{2.21}$$

where Q_o is the flow rate of the continuous phase and Q_w is the flow rate of the dispersed phase.

Flow rate in a channel is a function of the pressure difference and hydraulic resistance across the channel:

$$Q = \frac{\Delta P}{R_h} \tag{2.22}$$

where Q is the flow rate; ΔP is the pressure difference and R_h the hydraulic resistance.

In order to ensure that a stable water in oil emulsion is formed it is essential that the channel walls be treated with a hydrophobic coating, preventing adhesion of the aqueous phase.

2.3.3 Droplet Storage

In order to perform crystallization, an experiment requires time to undergo the processes of nucleation and growth. Therefore, when conducted in droplets, stable storage of those droplets for the requisite time period is essential. It is possible to store droplets formed in a microfluidic environment both either off-chip or within the device. Off chip storage can be achieved within a syringe or a standard 96 well plate, petri dish or flask, though this comes with the limitations of the storage medium. On chip storage allows the tailoring of the device to suit any storage and analytical needs.

2.3.4 Droplet Stability

Emulsions of droplets are thermodynamically unstable mixtures of immiscible liquids. The droplets have a high surface area leading to a high interfacial free energy. In response to this, the droplets are driven to coalesce, increasing their size, reducing the surface area and the interfacial free energy. Ultimately this leads to full separation of the two phases into layers. In order to stabilise such an emulsion, surfactants are used. Surfactants are amphiphilic molecules consisting of a hydrophilic head and a hydrophobic tail. When incorporated into an emulsion, this property causes surfactant molecules to accumulate at the oil / water interface which causes a decrease in the interfacial free energy allowing the droplets to remain stable [30].

Chapter 3

pH Dependent Solubility of DL-Phenylalanine

3.1 Introduction

The importance of crystallization processes in pharmaceutical and food science has led to the development of numerous methods for process control. The crucial parameter during crystallization is the solution saturation concentration (usually referred to as solubility) due to its effects on crystallization kinetics [1]. This factor usually influences kinetic equations through the term supersaturation: the ratio between the solute concentration and saturated concentration.

One method for controlling solution solubility is by controlling pH [31], one of the benefits being the large yields available, even in sparingly soluble compounds which can be protonated or deprotonated in aqueous solutions. pH is a measure of the acidity or alkalinity of an aqueous solution. It is an inverse logarithmic scale of the hydrogen ion concentration. Many pharmaceutical compounds are either weak acids or weak bases. The pH of a solution of a weak acid is related to the acid dissociation constant (K_a) and the ratio of the concentrations of the acid and its conjugate base. As the pH of such a solution is increased the ratio shifts in favour of the dissociated, conjugate base. The solubility of dissociated ions is often significantly greater than the solubility of the undissociated acid. This means that, in the case of a weak acid, as the pH is increased, the solubility is increased and, likewise, as the pH is lowered, the solubility lowers. This can be used to generate supersaturated solution by lowering the pH of a saturated solution of weak acid at high pH.

The model compound used, racemic phenylalanine, is amphoteric, meaning that it can behave as both an weak acid and a weak base. This is also dependent on the pH. In an aqueous solution as the pH trends towards the acidic; the amine functional group of the amino acid will accept protons from the solution forming a cation. Conversely, as the pH trends to the basic the carboxyl group will dissociate, donating protons to the solution.

These factors have the effect of creating a complex system where small changes in pH can have disproportionate and difficult to predict effects on solubility. For example: in an aqueous solution with excess solute present, the solute will dissolve until equilibrium is reached. However, as pH is increased, the effective solubility is also increased and more solute will dissolve until a new equilibrium is established. As the quantity of dissolved solute increases, the increased quantity of dissociated solute will contribute more H^+ ions to the solution, reducing the pH and thereby reducing the solubility. This makes solubility prediction challenging, however, the crystallization process requires that the solution be more concentrated than its equilibrium solubility. This compounds the problem. As the solution is supersaturated, the pH decreases further, thereby suppressing the solubility. When the solution crystallizes, the concentration decreases and the pH increases again, thereby increasing the solubility.

Furthermore, pH in a complex system usually has to be measured[32]. Without knowing the pH of a supersaturated solution the degree of supersaturation cannot be determined. However, this is nearly impossible in highly supersaturated solutions as introduction of a pH probe is likely to precipitate nucleation, reducing the concentration of solute and decreasing the buffering effect on pH.

In addition, the effect of solute concentration on pH makes experimental design significantly more difficult. In cooling crystallization, the relative supersaturation required for the process can be easily targeted by using

$$S = \frac{C}{C^*} \tag{3.1}$$

where C^* is the solubility at the target temperature. However, in pH-shift crystallization the pH of the supersaturated solution will affect a certain solubility at that pH, however, when that solution crystallizes, the pH will change and affect a different solubility. Therefore, the kinetics of the system changes after nucleation and yields are difficult to predict.

All of this serves to make pH-shift crystallization a particularly unpredictable and challenging system to work in. Previous work in this area has relied on the continuous addition of strong acid to a basic solution until the desired pH level is recorded[33][34]. However, such a system would not be feasible where pH cannot be directly monitored such as nucleation studies where the presence of a pH probe in solution could enhance heterogeneous nucleation. Other studies have used models that require the initial pH values of the solution and will predict the value when a known quantity of acid is added[35–39] This could be effective in many scenarios but would be more labour intensive.

3.2 Aim and Objectives

Utilizing DL-phenylalanine as a model system, this work seeks to establish a deep understanding of pH-shift crystallization in order to design further experiments in this experimental space. Solubility and pK_a data will be experimentally collected using gravimetric equilibrium concentration measurements and potentiometric titrations, respectively, to gain an initial reference points for further study of the model system. The collected data will be used to develop a predictive model that utilizes pK_a and solution composition to determine solution speciation and predict the solubility and supersaturation of a system with sufficient accuracy to design future experiments. This model will be validated by comparison to experimental pH-dependent solubility measurements and titration experiments.

3.3 Materials and Methods

3.3.1 Materials

Solutes

DL-phenylalanine (DL-phe; Sigma-Aldrich,$\geq$ 99%),was used as purchased. Sodium Hydroxide (anhydrous, Sigma-Aldrich, $\geq$98%) was used as purchased. Hydrochloric acid was purchased as 37% HCl (ACS, Sigma-Aldrich, reagent).

Solvents

The solvents and media used were aqueous Sodium Hydroxide (NaOH) solution, aqueous Hydrochloric Acid (HCl) and Milli-Q water. The Milli-Q water was taken from a Merck Millipore purification system and had a resistivity of 18.2 MΩ·cm at 25°C (Milli-Q water is referred to as water later on in the text unless otherwise indicated). Aqueous solutions of NaOH were prepared by dissolution of a known accurate quantity of pure NaOH pellets in approximately 70 mL of water in a volumetric flask. Water was then added to the flask up to the volume line, indicating 100 mL of solution to produce a solution of predetermined concentration. The flask was then inverted multiple times to ensure robust mixing. Aqueous solutions of HCl were prepared by mixing a known accurate mass of 37% HCl solution in approximately 70 mL of water in a volumetric flask. Water was then added to the flask up to the volume line, indicating 100 mL of solution to produce a solution of predetermined concentration. The flask was then inverted multiple times to ensure robust mixing.

3.3.2 Methods

Determination of solubility

Three methods were used to determine binary phase diagrams for solubility. The methods used are temperature variation (TV) and equilibrium concentration (EqC).

Temperature variation (TV) method The temperature variation protocol is a well established method that relies on changing the temperature to adjust the solubility and measure clear points[40–42]. Samples were prepared by adding a known accurate quantity of solid and 1 mL of water to each 1.5ml vial (VWR-548-0018). The samples were analysed in the Crystal16 multiple reactor setup (Technobis Crystallisation Systems, Alkmaar, Netherlands). Samples were agitated at 700 rpm stirring rate using a magnetic stirrer bar. The temperature was cycled three times between 80.0 °C and 5.0 °C with a heating and cooling rate of 0.3 °C min^{-1}. At maximum and minimum temperature, a hold time was applied for 30 minutes to ensure full dissolution and crystallization of solute respectively. Clear and cloud points were registered according to the turbidity measurement recorded by the transmission of light through each vial. Clear point temperature is the temperature at which the suspension at equilibrium becomes a clear liquid. When dissolution kinetics can be neglected, the clear point can be used as an indication of the saturation temperature of the sample with known concentration. Cloud point temperature is the temperature at which a supersaturated solution crystallizes. This is marked by a decrease in transmittivity through the solution, indicating the presence of crystals. Cloud point is used as an indicator of the upward limit of the metastable zone. The saturation temperature was recorded as the mean of three clear point measurements. This method was used for the solubility measurement of DL-Phenylalanine.

Equilibrium concentration (EqC) method The gravimetric protocol used was adapted from literature [1]. An excess of compound was added to a 2 mL mixture of aqueous medium (1.0 M HCl solution and 1.0 M NaOH solution) in each 8 mL vial (VWR-548-0821). The suspensions were then equilibrated at constant temperature for 24 hours in the Crystalline multiple reactor setup (Technobis Crystallisation Systems, Alkmaar, Netherlands). Crystals were agitated at 700 rpm stirring rate using magnetic stirrer bars. A sample of the saturated solution was taken using a syringe. The sample was then filtered. The pH of the equilibrated solution was recorded by a pH meter (HALO® Wireless pH Meter with Microbulb, Hanna Instruments, RI, USA). The calibration of the pH meter was conducted using buffer solutions of pH 4.01, 7.00 and 10.01. The mass of the saturated solution was measured and the solvent was evaporated using a vacuum oven at 40 °C. The dry mass remaining from the sample was then weighed. The difference between the mass of the sample solution added and the mass remaining after dissolution indicated the amount dissolved in the aqueous medium, giving an indication of solubility This method was used for the solubility measurements of DL-phenylalanine.

Model Validation via Batch Titration

Potentiometric (acid – base) titrations were performed on the Sirius Inform instrument (Pion, UK) as pH-metric pK_a assays. These are small volume (40 mL) acid-base titration assays. Ionic strength adjusted (ISA) water (0.15 M NaCl) was used as titration medium to allow pH adjustment over the pH range from pH 1.8 – pH 11. The pH was cycled from the bottom of the range to the top two times. pH adjustments were performed with 0.5 M NaOH and 0.5 M HCl, respectively. Titrations were performed at 25C. Phenylanine powder ∼ 10-15mg (12.30mg) was presented in powder form and after ISA water addition, the medium was stirred for 300 sec at 300 rpm to allow for temperature equilibration and sample dissolution.

3.3.3 Solution Speciation and pH

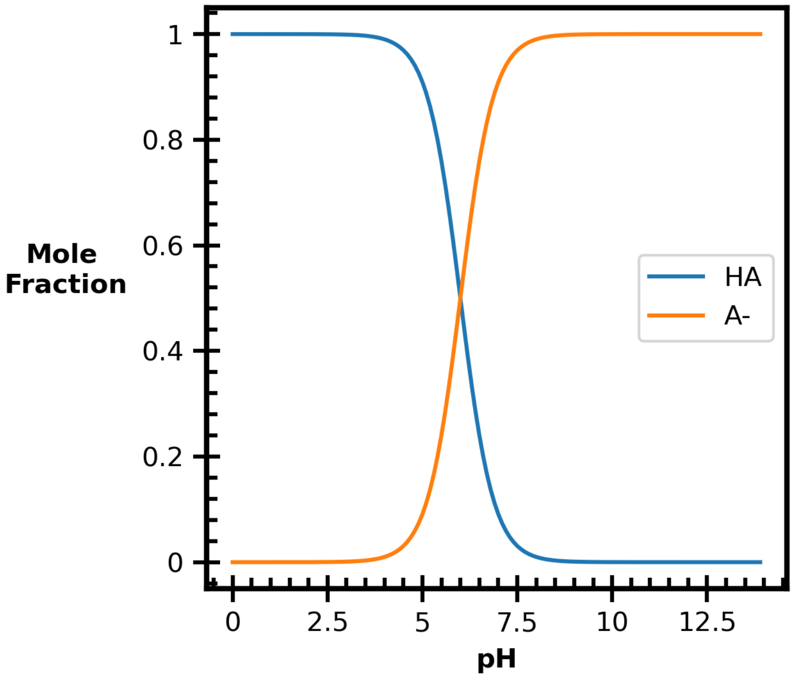

Figure 3.1: Example speciation diagram for a weak acid with pK_a 6

Solution speciation refers to the distribution of a dissolved substance among its various forms[32]. Depending on the chemical properties of the solution, the distribution of forms will be different. A strong acid or base in solution is assumed to be fully dissociated and so all components will be in the form of ions. Conversely, in a weak acid or base, the speciation is more complicated to determine as speciation is dependent on other factors. For example, a monoprotic weak acid in solution will be split between across its dissociated and neutral species according to the pH of the solution and the dissociation constant (e.g. Figure 3.1).

$$K_a = \frac{[H^+][A^-]}{HA} \tag{3.2}$$

where $[H^+], [A^-]$ and $[HA]$ are the concentration of hydrogen ions, conjugate base and undissociated acid, respectively. The pK_a value $(-logK_a)$ of weak acid can be used to calculate the species concentrations, whereby the pK_a, is the pH at which the weak acid is 50% dissociated. The Henderson-Hasselbalch equation (3.3) can be rearranged to determine the solution speciation for a solute at given pH.

$$pH = pK_a + log\left(\frac{Base}{Acid}\right) \tag{3.3}$$

However, there are several factors that complicate calculation of speciation. For example, the dissociation of a weak acid contributes more hydrogen ions to the solution and so affect the pH and effect a change in the dissociation of the solute. Solution activity effects play a crucial role in solution speciation, especially for highly concentrated or non-ideal solutions. The activity of a species in a solution is defined as its effective concentration, which may differ from its actual concentration due to interactions with other species or deviations from ideal behavior. Indeed, precise measurement of K_a can only be done when observed at constant ionic strength, a key determinant of solution activity. This can be imperfectly compensated for by applying a corrective term, the solution activity coefficient.

3.4 Results and Discussion

3.4.1 Aqueous Temperature-Dependent Solubility of Neutral Species DL-Phenylalanine

The solubility model used in this work relies on two fundamental physical properties of the model compound, one of which is neutral species solubility. Neutral species solubility determination was initially attempted with a temperature variation method. However, the hydrophobic nature of DL-phenylalanine causes many of the crystals formed during cooling to float on top of the solvent. This, combined with the low solubility of the model compound, ensured that the quantity of crystalline material suspended in the agitated solution was lower than the minimum detection limit of the Crystal16 equipment, thereby hindering the collection of clear points for solubility. Therefore, a gravimetric protocol was used to determine solubility. This method is regarded as a more precise method but is labor intensive (Figure 3.2 (a)).

There is limited reporting of the solubility of DL-phenylalanine, perhaps because it is less common than the L form, which is more commonly found in life and therefore better studied[43]. However, it was selected as a model compound due to its low aqueous solubility and the high dependence of solubility on pH, allowing for generation of a high degree of supersaturation. The available literature data[44][45] was compared with experimental data and the acquired solubility was found to conform reasonably to the literature within the expected normal variance between data collected in different labs under slightly different conditions. It should be noted that the experimental solubility from Dalton et al. [44] was collected at 10 temperatures between 0 and 75 °C. However, the data reported by them was an empirically fitted logarithmic function of the

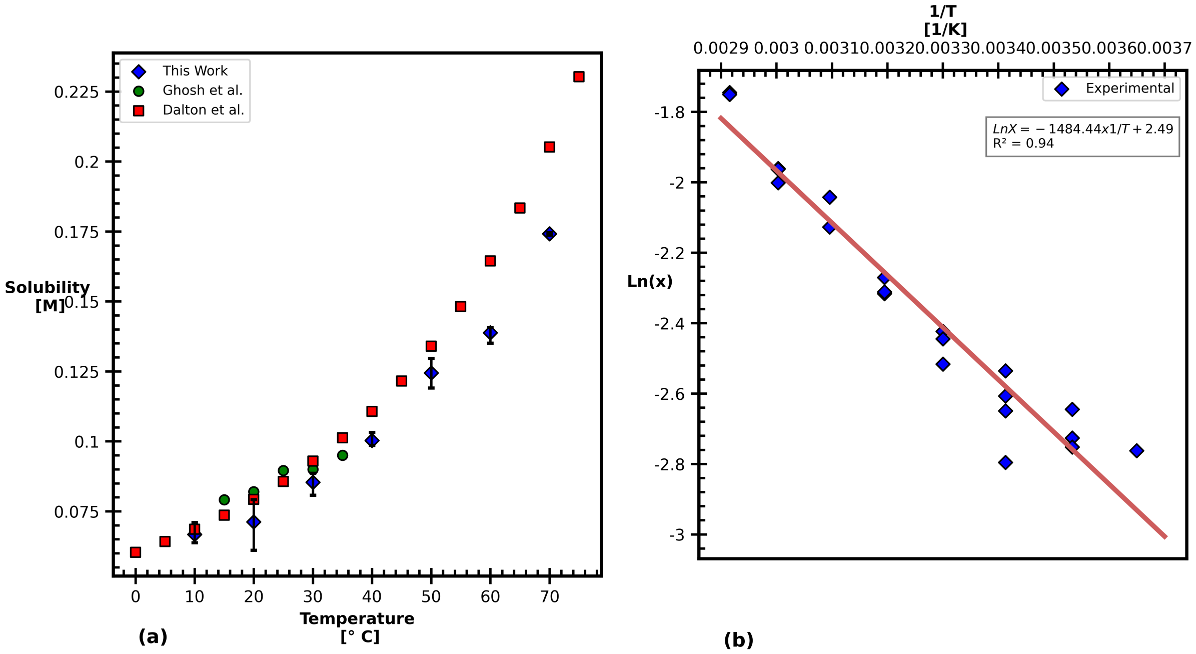

Figure 3.2: Graph of experimentally obtained temperature dependent solubility of DL-phenylalanine at the isoelectric point including literature data.

data and therefore is not precisely speaking solubility data. The data presented from this work in Figure 3.2 (a) are an average of values at each temperature point

A Van't Hoff plot was fitted to all solubility data collected (Figure 3.2 (b)). The relatively high R^2 value indicates good fitting with the data. Solubility data of this nature will often have a degree of variance related to variation in weighing and drying of material. Care was taken to ensure that all solvent was fully evaporated to minimise any error. DL-Phenylalanine solubility shows a reasonable degree of temperature dependence, however, the maximum supersaturation ratio that can be achieved in the temperature range investigated is 2.5. While this supersaturation would obviously be adequate for inducing crystallization in the small volume reactors of a Crystal16. The probability of nucleation occurring in a vessel is a function of the volume of the reaction vessel. Therefore, it is anticipated that crystallization in a microfluidic device will require greater supersaturation than is available to a cooling crystallization experiment in order to increase the probability that nucleation will occur in a reasonable time frame. It was therefore determined that an alternative method for generating a crystal driving force was required.

3.4.2 Aqueuous pH-Dependent Solubility of DL-Phenylalanine

pH-dependent solubility for amino acids in general is not well reported in the literature. There are some papers covering other amino acids[46–48]. However, there is only one paper in the literature reporting pH-dependent solubility of DL-phenylalanine[31]

pH-dependent solubility data was collected at 293.15K using the gravimetric protocol covering a pH range from 8.5 - 11.5. Figure 3.3 shows a marked increase in measured solubility as pH is increased.

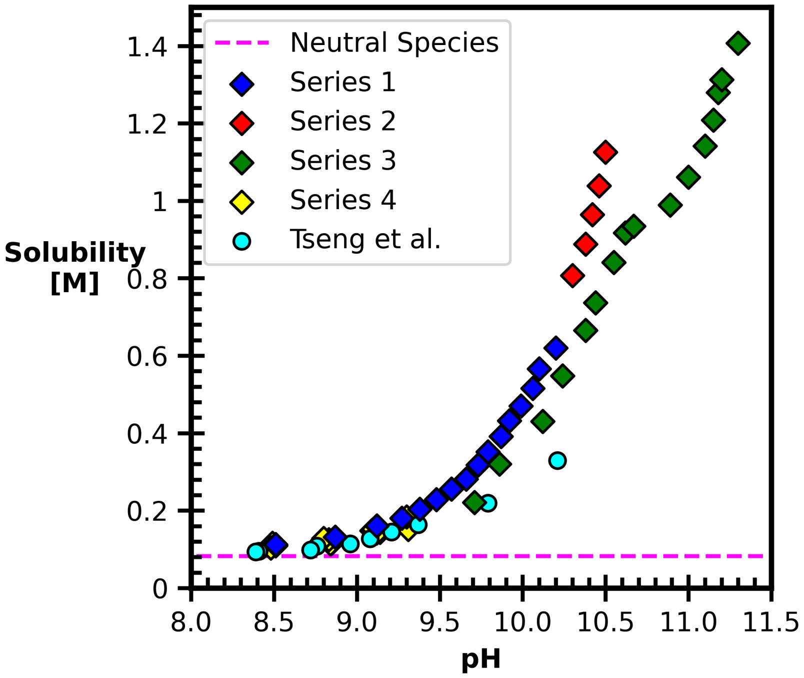

Figure 3.3: Experimentally obtained pH dependent solubility of DL-phenylalanine in pH controlled water from gravimetric measurement of equilibrium solubility conducted at 293.15K. In Series 1, 2 & 4 pH was controlled using a mixture of sodium hydroxide and hydrochloric acid. For series 3, the pH was controlled using dilute solutions of sodium hydroxide.

The lowest point of solubility is that of the neutral species at the isoelectric point (pH 5.5) as expected. The pH increase does not appreciably affect the solubility until it approaches the upper pK_a of the solute ($pK_a \sim 9.1$). As the pH tends towards the pK_a the pH increase causes the ionization of amino acid. The resulting conjugate base has a significantly greater solubility than the neutral species. There also appears to be a change in the trend of solubility above pH 10.5. This could be due to potential salt formation above this pH, although further exploration of this phenomenon was not within the scope of this work as it exceeds the region of pH values for study. The data reported by Tseng et al.[31] is reported as molality, however, it is reported without any reference to density values. It is included here (assuming a density of 1 g/ml) for the sake of completeness (as there is no other source for the pH dependent solubility of DL-phenylalanine in the literature). However, it cannot be used as a definitive comparison due to the limitations of the reported values in the paper. Comparison of measured pH data is only accurate at constant ionic strength. Solution ionic strength (Equation 3.4) has numerous effects on pH and solubility through activity effects[1]. The presence of cations and anions in solution leads to coloumbic interactions between ions. Oppositely charged ions attract and similarly charged ions repel. In a solutions where ions are able to move freely, a high ionic strength will have lower energy due to the decreased average distance between ions. This lowered energy leads to a weak dependence of solution equilibria on ionic strength. The ionic strength can be calculated by the following equation:

$$I = \frac{1}{2} \sum c_i z_i^2 \tag{3.4}$$

where c_i is the concentration of the ith ionic species, and z_i the valency.

Experimentally observed pH-dependent solubility varied in ionic strength for each series and from the literature data and this explains the wider spread of solubility values between the different data. As series 3 was conducted without addition of hydrochloric acid, the solutions contained fewer ions at low pH than the other series and therefore, the ionic strength was lower for pH values between pH 9.5 - 10.2 than series 1 (Figure 3.4).

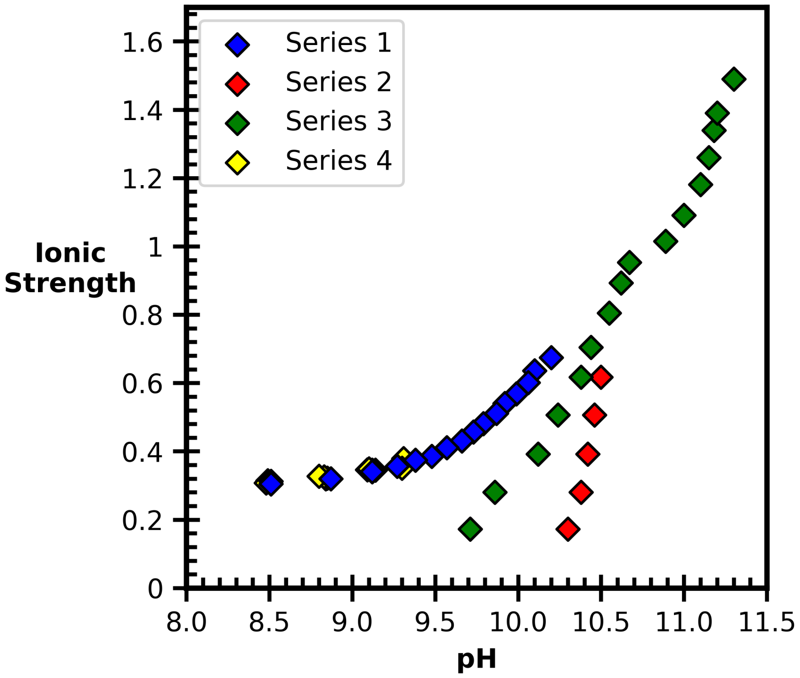

Figure 3.4: Ionic strength data for all experimental solubility series

The solution activity was, therefore, also lower and this likely led to a reduction in observed pH-dependent solubility. Collecting data at higher pH requires a greater concentration of sodium hydroxide leading to a greater ionic strength at higher pH as seen by the increased ionic strength of series 3 in the higher pH range. Using hydrochloric acid to further aid pH control also impacts ionic strength. At higher concentrations of NaOH, more HCl is required to lower the pH. As the NaOH is in excess of the HCl, all of the HCl added is converted to NaCl and water. The water makes no contribution to the ionic strength and the NaCl makes a lower contribution than the total ionic strength of its reactants. Therefore, the use of HCl to control pH at higher values leads to lower ionic strength relative to using pure NaOH. These slight differences in control show that a fully mechanistic model for predicting pH and solubility ought to include ionic strength. There is an apparent change in the solubility in series 3 at pH greater than 10.5, however, there is not enough data available to confirm this. A possible explanation for this might be the formation of the sodium phenylalanate salt in the solution. Future investigation would require crystallization at pH greater than 10.5 and the X-ray powder diffraction of the dried crystals for change in crystal form, which would indicate whether or not a salt had formed. The experimental data shows a greater degree of variability at higher pH. As such, future experiments were not conducted at pHs greater than 10. The experimental data correlates reasonably well with the limited literature data available.

3.4.3 pK_a value for DL-Phenylalanine

A pH metric titration assay was conducted to determine pK_a of DL-phenylalanine and to provide data points for validation of the mathematical model (Figure 3.5).

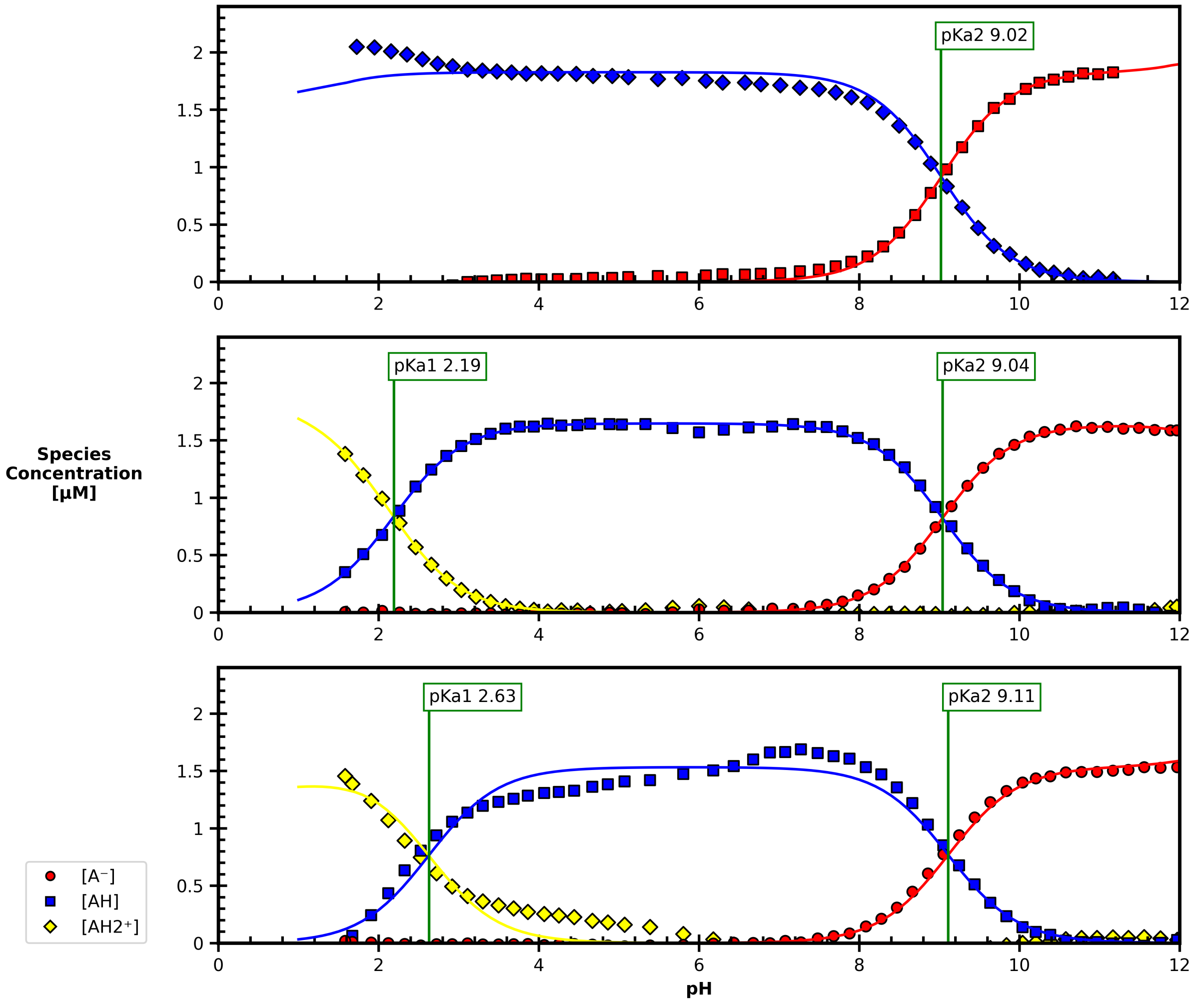

Figure 3.5: pK_a data observed from a single potentiometric titration in the presence of DL-phenylalanine at 298.15K. pH was titrated from 1.8 - 11 - 1.8 - 11 giving 3 values for pK_a at high pH and 2 values at low pH. The pK_a values recorded were infered from the intercepts of the fitted lines generated by the inform software. .

The pK_a was observed using the Sirius inform, which uses proprietary software to fit the acquired titration data to a dissociation model. It is unknown if this model uses an ideal or non-ideal fitting. The point at which the concentrations of species cross over is recorded as the pK_a for that functional group. The pK_a observed at the higher pH was consistent and easily determined from the recorded species concentration. However, the model data was less consistent at the lower pK_a. This was deemed not to be an issue as all experiments conducted in further chapters occurred at pH greater than 8 and therefore were only reliant on the higher pK_a. Observed pK_a for phenylalanine at the higher pH (9.0 - 9.1) was seen to conform reasonably with literature data (Figure 3.6) [49][50][51][52][53][54]. The literature reported values were conducted at a range of ionic strengths and the pK_a was observed to be higher at low ionic strength. The values observed experimentally were collected at higher ionic strength and gave a lower value than the majority of the literature values. The pK_a in literature was also determined by potentiometric titration.

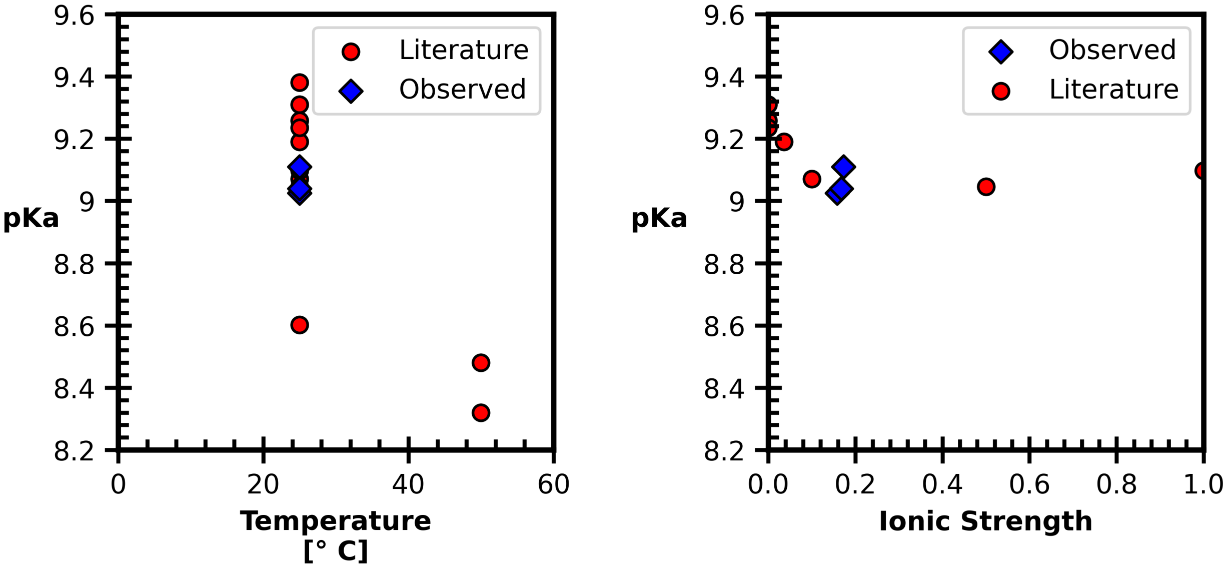

Figure 3.6: Collation of pK_a values for Phenylalanine from the literature

3.4.4 Mathematical Models

Crystallization process design requires a precise understanding of solution conditions including solubility and supersaturation. The pH dependence of solubility renders pH a critical condition to understand. For induction time experiments conducted in chapter 4 pH could be measured at the end of the experiment, however, the solutions tested were supersaturated at the experimental temperature. Therefore, introduction of a pH probe into the solution was prone to inducing crystal nucleation. Nucleation would consume supersaturation, reducing the solution concentration and thereby altering the pH. To avoid this problem the pH was measured at 50 °C where the higher temperature meant a higher solubility and therefore reduced supersaturation or undersaturation. However, pH measurements change with temperature and a value recorded at 50 °C is not the same as one recorded at 20 °C. A calibration line was determined and used to predict the pH at 20 °C. However, this method is inaccurate and it was therefore deemed more consistent to utilize the model for predicting pH both for experimental design purposes and for clarification of solution pH of conducted experiments.

The mathematical model developed utilizes commonly understood equations, well reported in the literature. However, they are most often applied in situations where pH is known and it is uncommon to use the equations in a predictive capacity. With the aid of modern computing power, these equations can be numerically solved simultaneously, enabling the prediction of pH and complete speciation of components based solely on solution composition and dissociation constants as inputs. Analytically solving these equations is not possible, necessitating the use of numerical methods for their solution. Once a value for pH is known further equations can be applied to make predictions for solution solubility based on the neutral species solubility and this in turn allows the calculation of a consistent supersaturation ratio. The model presented here is an adaptation for amphoteric, amino acids of models initially applied to organic salt crystallization[55].

Speciation and pH

Designing and conducting pH-shift crystallization of organic molecules requires a detailed understanding of acid/base speciation and ionic equilibria. Most pharmaceutically active compounds are weak acids or bases and have complex solution speciation dependent on solvent, temperature and most critically: pH.

The acid dissociation constant K_a is the ratio between the dissociated and undissociated species of a weak acid or base when it is at equilibrium. Much like pH is an easier to use value than [H^+]; pK_a (Equation 3.5) is more useful than K_a.

$$pK_a = -logK_a \tag{3.5}$$

pK_a can be used to characterise the dissociation of a weak acid or base from the overall pH of the solution and from dissociation, concentration of this species can be determined.

Solution activity coefficient was calculated through ionic strength using the Davies equation[56] (Equation 3.6).

$$log\gamma = -A|z_+z_-| \left\{ \left[\frac{I^{0.5}}{I + I^{0.5}} \right] - 0.3I \right\} \tag{3.6}$$

The Davies equation is deemed to be one of the most reliable for concentrations below 0.2 molar[1], however, it was deemed sufficiently accurate for this model to be useful.

The concentration of all species can be calculated by simultaneously solving a block of equations utilizing the solution composition and the dissociation. γ is multiplied by the concentration of each dissociated species with regard to their dissociation equilibria. From solving this block, hydrogen ion concentration can be determined and therefore, pH calculated.

Model equations

The model used in this work was designed to apply to single phase solutions where all components were fully dissolved in solution regardless of degree of supersaturation. In order to fully determine speciation, several physical phenomena must be incorporated into the model: the acid-base equilibria of the deprotonation of the carboxylic acid group at high pH and the protonation of the amino group at low pH, the dissociation of the water solvent, the overall charge balance which accounts for the presence of strong acid and strong base and the materials balance and the overall materials balance.

$$[Phenylalanine] = [AH] + [A^-] + [AH_2^+] \tag{3.7}$$

The water dissociation constant was included along with the relevant solution activity coefficients:

$$K_W = [OH^-]\gamma[H^+]\gamma \tag{3.8}$$

The acid-base dissociation constants from equation 3.5 can be updated with the solution activity coefficients

$$K_a1 = \frac{[A^-]\gamma[H^+]\gamma}{[AH]} \tag{3.9}$$

$$K_a2 = \frac{[AH_2^+]\gamma[OH^-]\gamma}{[AH]} \tag{3.10}$$

Finally, the overall charge balance must be modelled to account for the strong acid and base present.

$$[Na^+] + [H^+] + [AH_2^+] = [A^-] + [OH^-] + [Cl^-] \tag{3.11}$$

In the model, concentration values for all components is known (including the fully dissociated strong acid and base) and the dissociation constants are known. When all equations (3.7-3.11) are treated as a system and solved for the four unknowns: the species concentrations are returned. This was achieved utilizing the symbolic numerical solver, vpasolve, found in the Symbolic Math Toolbox of MATLAB. The proton concentration is then known and therefore, the pH can be known.

3.4.5 Model Validation

pH Prediction

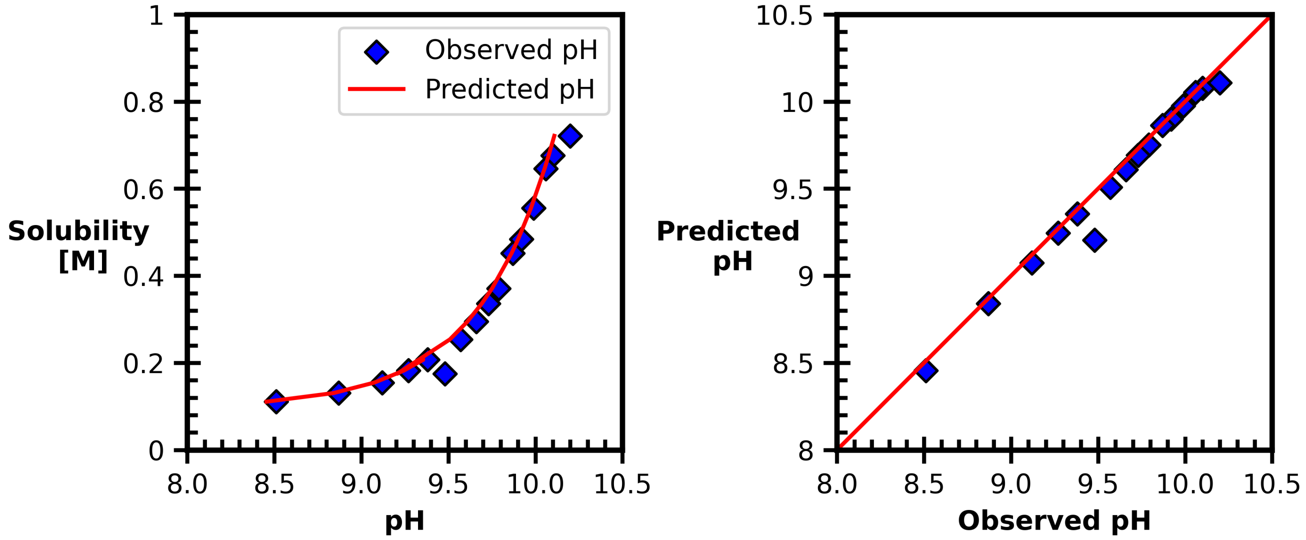

Figure 3.7: Using the solution compositions of DL-Phenylalanine pH-dependent solubility data collected in Crystal16 (Figure 3.3 series 1) the model was used to predict the pH. The predicted pH is then plotted against the observed pH. The model utilized a pK_a of 9.3 and ideal solution activity.3.6

To validate the efficacy of the model in predicting solution pH, solution composition from solubility experiments was input into the model and the returned predicted pH compared to the experimentally observed pH (Figure 3.7). The predicted pH only slightly deviates from the validation line with the predicted pH being consistently slightly lower than the observed pH. There is a single outlier and this is believed to be due to human error in recording the solution composition during weighing.

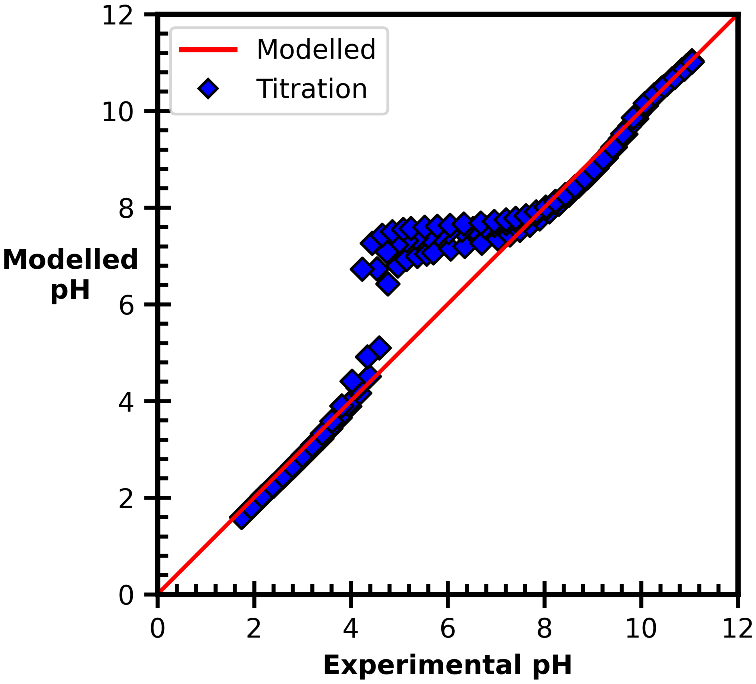

Figure 3.8: The solution composition data from the titration experiment shown in figure 3.5 was input into the ideal model to predict pH. The predicted pH is plotted against the observed pH.

The titration experiment conducted for the determination of pK_a also allows for validation of the model. The solution composition of each recorded pH during the titration was input into the model and the returned pH value compared to the observed pH (Figure 3.8). The model shows excellent predictive power for pH ranges from 8 - 11.5 and below pH 4. In the range pH 4-8 there is a significant deviation from the observed experimental pH. This is to be expected as small changes in hydrogen ion concentration around neutral pH have much greater effect on pH. However, it does not have a significant impact on this work as it is outwith the range of pH values studied. It was not possible to validate the accuracy of the model at pH values outside this range due to the limitations of the instrumentation for measuring pH.

Solubility prediction

A mechanistic model was developed for predicting the solubility. Two models were created: one for ideal solutions and another for non-ideal solutions. In the ideal model, the pH prediction element was decoupled from the solubility prediction element of the model.

The model assumes that the solubility of the conjugate base is effectively infinite, while the solubility of the neutral species remains the same. The solubility value for a given concentration of phenylalanine is the pH at which the concentration of undissociated phenylalanine is equal to the solubility of the neutral species. The model functions by performing a "titration", progressing through a series of sodium hydroxide:hydrochloric acid ratios while maintaining the same phenylalanine concentration. For each solution composition, the model returns the concentration of each species in solution, including [H$^+$] and [AH]. When the concentration of undissociated phenylalanine [AH] crossed the threshold of the neutral species solubility the solution acid-base composition and the pH was recorded (Figure 3.9). For the ideal model, the speciation model utilized equations 3.8, 3.9 and 3.10 but γ was given a value of 1. For the non-ideal model, the value for γ was acquired from equation 3.6. This model was also used to calculate the supersaturation ratio from the soltion speciation for a given composition using the following equation:

$$S = \frac{[AH]}{C^*_{AH}} \tag{3.12}$$

Where C^*_{AH} is the neutral species solubility.

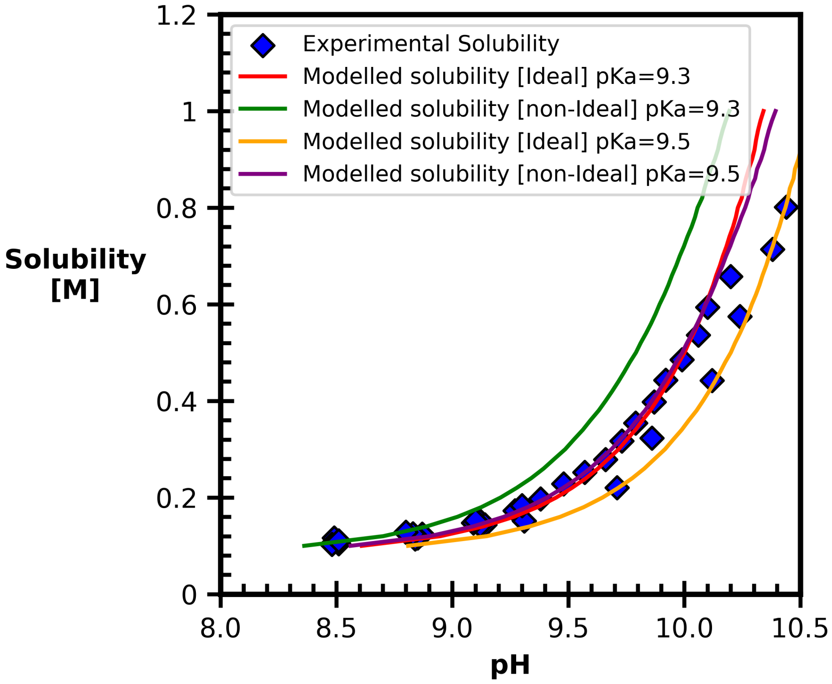

Figure 3.9: Solubility modelled in ideal system and non-ideal systems at 293.15K. The model utilized pK_a values of 9.3 and 9.5 for both ideal and non ideal. The non-ideal model used a calculated activity coefficient based on equation 3.6

Figure 3.9 displays the non-ideal solubility model and the ideal model for selected pK_a values. The models were developed for the purpose of calculating pH (and, secondarily, solubility) for experiments in which the value cannot be observed using a pH probe, for example, microfluidics and in supersaturated solutions. The models rely on real physicochemical properties of the solutions, however, it was decided that it was more important for the model to be useful than strictly mechanistically accurate. Therefore, the pK_a value was adjusted to get the closest fit to the experimental data as possible. Both models used a neutral species solubility of 0.083 M. The neutral species solubility was determined from the Van't Hoff plot of the temperature at 293.15K. The pK_a value was within the range of normal values at this temperature found in the literature. However, it was found to be necessary to adjust the pK_a within the range to fit the solubility line to the observed experimental solubility data. In this case, a pK_a of 9.3 most adequately fit the data for the ideal model and a pK_a of 9.5 best fit for the non-ideal model. The ideal model at pK_a 9.3 was selected as the model for use in further experiments as this pK_a value is more in line with the pK_a values in literature and reported here.

In addition, the supersaturation can be calculated for any solution composition by acquiring the neutral species concentration in a given solution and applying equation 3.12. The neutral species solubility point for the desired temperature was calculated from the Van't Hoff plot presented in Figure 3.2.

The ideal model provided a predicted solubility close to the pH-dependent solubility lines at pK_a 9.3. This was deemed to be a good model but further investigation was done to assess whether the model could be improved by the incorporation of non-ideality through activity coefficients. The simple non-ideal model used was found to make the solubility prediction less accurate to the experimental solubility (figure 3.9). This inaccuracy could be compensated for by increasing the pK_a to shift the solubility line, however, this required pK_a values outwith what has been observed for this molecule under these conditions. Improvements could be made to this non-ideal model. Barba et al created a thermodynamic model for solubility determination of calcium sulphate in salt water using a complex model comprising elements of Debye-Huckel, the Born Model, and NRTL model to describe activity coefficients [57]. While it would be possible to implement a similar level of detail into the model, it was deemed beyond the scope of this work. Therefore, the ideal model was used to inform further experiments conducted in chapters 4 & 5.

The model covers a limited range of pH values. As the input parameters (pKa and solution activity) were adjusted to achieve an adequate fit to the collected pH-dependent solubility data, any application of this model to another system would require the same adjustment to fit experimental data. The ideal model was found to be sufficient for prediction in this system. This may not apply to systems using an alternative solvent and would, therefore, need to be verified. Finally, there appeared to be some variability in the quality of pH prediction at higher pH values and ionic strengths and this may limit the utility of the model in such systems.

3.5 Conclusions

This work presents experimental pH-dependent solubility data for DL-phenylalanine collected using a gravimetric equilibrium concentration method and pK_a determined by potentiometric titration. From this experimental data a speciation and pH-dependent solubility model that can be used to predict pH of a solution and the pH dependent solubility of an active ingredient was developed. The model makes use of dissociation constants and solution composition to predict pH, solubility and supersaturation. Non-ideality was incorporated into the model through the Davies Equation. The model can also be used for supersaturation of metastable solutions. The model was validated with experimentally collected pH values and solution composition data from solubility experiments and potentiometric titrations. The final model produces consistent, sufficiently accurate estimations of pH and supersaturation from compositional data. Further applications of this work could be to explore deeper the application of non-ideality through a more complex system of equations.

Chapter 4

The Study of DL-Phenylalanine Crystal Nucleation Kinetics Using a Small Scale Agitated Crystallizer

4.1 Introduction

Crystal nucleation is the process by which a crystal forms from a supersaturated solution or melt. It is the first step in the crystallization process, and involves the formation of a small nucleus, which then grows into a crystal[11][58].

Understanding the factors that influence crystal nucleation, and the kinetics of the process, is important in a variety of fields, as it can help predict and control the rate at which crystals form. In addition, the nucleation event affects the crystal quality attributes (CQAs) such as polymorphism, crystal shape and particle size distribution. In food science, for example, nucleation kinetics can be important in the production of food products such as chocolate [59]. The rate at which crystals form in these products and their CQAs can affect their texture, flavor, and appearance.

In the pharmaceutical industry, crystal nucleation kinetics can be important in the development of new drugs [15]. Drugs are often administered in the form of crystals, and the rate of nucleation can affect crystal particle size distribution and crystal shape which can affect downstream process and are therefore necessary to control in an industrial process. By understanding the factors that influence crystal nucleation, researchers can design drugs that crystallize in a desirable manner.

The fitting of a large number of induction time measurements to a cumulative probability distributions can give a value for nucleation rate at constant volume [25]. This method of nucleation rate estimation utilizes the stochasticity of nucleation expressed in the Poisson probability distribution of multiple, independent induction times observed at constant supersaturation and volume.

4.2 Aim and Objectives

In this work, we will study nucleation behaviour in supersaturated solutions of the model system (which expresses pH-dependent solubility) in a high pH context. We will establish the metastable zone width of the model compound, DL-Phenylalanine, at a range of different pH values and supersaturation ratios through the observation of nucleation induction times under isothermal conditions. It was decided to study agitated systems using a widely adopted approach utilizing small agitated vials in the Crystal16 multiple reactor system. The collected induction time distributions for each experimental condition will be fitted to a cumulative probability distribution to determine the crystal nucleation rate for each set of conditions. The collected nucleation rates will then be fitted to the experimental conditions to investigate potential relationships between the solution composition data (supersaturation and pH) and the nucleation rate.

4.3 Materials and Methods

4.3.1 Materials

Solutes

DL-phenylalanine (DL-phe; Sigma-Aldrich,$\geq$ 99%),was used as purchased. Sodium Hydroxide (anhydrous, Sigma-Aldrich, $\geq$98%) was used as purchased. Hydrochloric acid was purchased as 37% HCl (ACS, Sigma-Aldrich, reagent).

Solvents

The solvents and media used were aqueous Sodium Hydroxide (NaOH) solution, aqueous Hydrochloric Acid (HCl) and Milli-Q water. The Milli-Q water was taken from a Merck Millipore purification system and had a resistivity of 18.2 MΩ·cm at 25°C (Milli-Q water is referred to as water later on in the text unless otherwise indicated). Aqueous solutions of NaOH were prepared by dissolution of a known accurate quantity of pure NaOH pellets in approximately 70 mL of water in a volumetric flask. Water was then added to the flask up to the volume line, indicating 100 mL of solution to produce a solution of predetermined concentration. The flask was then inverted multiple times to ensure robust mixing. Aqueous solutions of HCl were prepared by mixing a known accurate mass of 37% HCl solution in approximately 70 mL of water in a volumetric flask. Water was then added to the flask up to the volume line, indicating 100 mL of solution to produce a solution of predetermined concentration. The flask was then inverted multiple times to ensure robust mixing.

4.3.2 Methods

Solubility and Supersaturation determination

Initial solubility data reported in chapter 3 was used to select a pH and supersaturation ratio for initial experiments and solution composition was adjusted to achieve nucleation within the time window selected. Measurement of pH during an experiment was impractical as the introduction of a probe into the supersaturated solution could induce crystallization and required the removal of the vial from the temperature controlled environment. Therefore, pH was measured at 50 °C when the solution was undersaturated. However, pH changes with temperature, therefore, this measure was imprecise. Therefore, a solution speciation and solubility model was developed (chapter 3.4.4). Solubility and supersaturation used in this chapter were according to this model.

Induction time measurement

The induction time collection methodology was adapted from work conducted by Jiang et al.[25]. Induction times were measured at 20 °C in the Crystal16 multiple reactor setup (Technobis Crystallisation Systems). The model compound was DL-Phenylalanine.A stock solvent was prepared by mixing specific amounts of a 1.0 M NaOH solution and a 1.0 M HCl solution to reach a target pH. 20 g of this stock solvent was added to a known quantity of DL-Phenylalanine. This was heated and stirred with a magnetic stirrer bar at 350 rpm on a hot plate until complete dissolution of the compound. Using a pre-heated pipette tip, 1 mL of solution was pipetted into 16 1.5 mL vials containing a 0.7 mm magnetic stirrer bar. The vials were transferred to the Crystal16. The samples were agitated at 700rpm stirring rate. The samples were heated to 70 °C, which was greater than the saturation temperature, and held for 30 minutes to ensure complete dissolution. The clear solution was then cooled at a rate of 2 °C per minute to 20 °C. For recording the induction time, time zero was taken as the moment the temperature reached 20 °C. The samples were held under isothermal conditions for four hours. The induction time for a particular vial was recorded as the difference between time zero and the time at which there was a decrease in the transmittance of light through the vial. After the induction time measurement period a new temperature cycle was started and the samples were reheated at a rate of 2 °C min^{-1} to 70 °C. This cycle of cool-hold-heat-hold was repeated 5 times to obtain 80 (16 x 5) readings for each solution composition.

4.4 Results

4.4.1 Metastable Zone Width Assessment

The study aimed to investigate the nucleation rate of DL-Phenylalanine by analyzing the probability distribution of induction times at different pH levels and supersaturation ratios in a Crystal16 multiple reactor setup. To define a clearly delineated area of interest for studying nucleation kinetics, pH values ranging from 9 to 10 were specifically chosen to establish the region along the solubility curve where the metastable zone can be determined. The pH was controlled through varying concentrations and ratios of NaOH and HCl solutions. Initial experiments were conducted at 20°C based on a preliminary understanding of pH dependent solubility, with the hope of obtaining reasonable results. A good result, later called sufficient nucleation, was if at least 10 nucleation observations out of 80 vials at each experimental condition nucleated in a four hour time window. However, initial experiments yielded either no nucleation or excessive nucleation (where at least one of the vials nucleated prior to reaching the isothermal point). Through trial and error, conditions that resulted in sufficient nucleation were discovered. However, it was difficult to replicate these intial results due to small changes in the solution concentrations of DL-phenylalanine, NaOH and HCl having large effects on the pH and consequently, the supersaturation.

To improve the consistency of solution concentrations, the experimental protocol was adjusted by using large stock solutions of mixed NaOH and HCl solution for several induction time experiments. This reduced some of the inconsistency and it was therefore possible to gather data points in a small range around the initial conditions. However, it was still difficult to expand the range of pH and supersaturation to cover a wider experimental space. To overcome this problem, a MATLAB model was developed (Chapter 3) to predict the pH and supersaturation for a given solution composition. This model was used to select solution compositions for data points in a broader range of pHs, and data was collected across the pH range from 9-9.8. The data

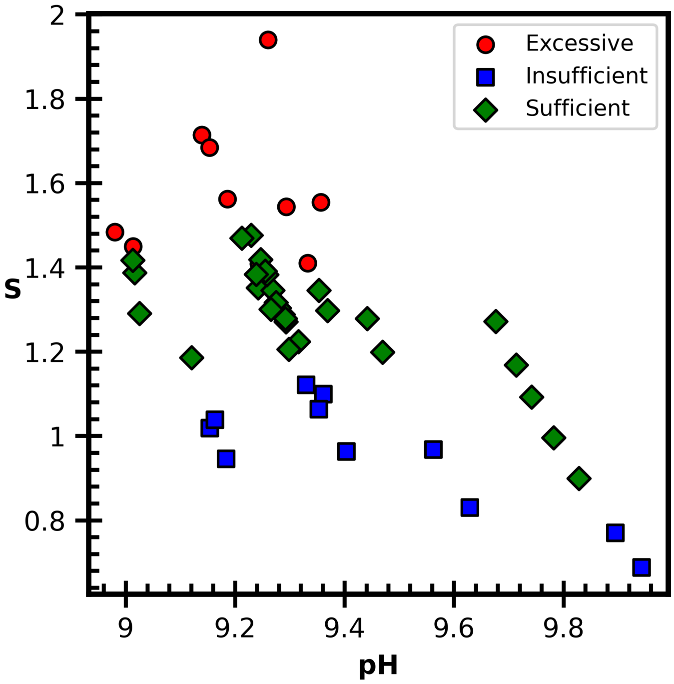

Figure 4.1: All induction time experiment pH and supersaturation ratios according to the Matlab model developed in chapter 3. Nucleation result is highlighted as blue for insufficient, green for sufficient and red for excessive nucleation

was categorized according to the nucleation behavior observed. If fewer than 10 vials nucleated within the four hour experimental window then the nucleation rate was deemed insufficient to gather statistically relevant data [26]. Fewer than 10 of the vials would give insufficient data to make a sufficiently accurate estimation of nucleation rate. A minimum of 10 observations of nucleation was deemed sufficient and if nucleation occurred prior to reaching the isothermal point it was categorized as excessive. The rationale for this threshold was that nucleation that occured before reaching the isothermal point could not be fitted alongside later nucleations as the supersaturation ratio for those vials would be different. The supersaturation was adjusted in order to map out the metastable zone. The supersaturation was then increased until the result was excessive nucleation and then decreased until the result was insufficient nucleation. 30 experimental runs were categorized sufficient, 11 were insufficient and 10 were excessive.

According to the gathered data (Figure 4.1), there is a clear relationship between supersaturation and nucleation rate. The general trend shows that the majority of experiments deemed excessive have a higher supersaturation than those deemed sufficient. Likewise, the experiments deemed insufficient are mostly at supersaturation ratios below sufficient experiments. However, there appears to be an indication that at higher pH values the nucleation rate is greater as for experiments conducted in the pH range 9.6-9.8, where the extent of the metastable zone is lower than that at lower pH values. For pH values below 9.6 a transition region can be observed between 1.4 and 1.5 where the nucleation rate varies between sufficient and excessive. A supersaturation of 1.5, under these conditions, imposes a strict upper limit to the metastable zone. In the region of $S = 1.2$ there seems to be a similar transitional region where nucleation appears sufficient. Finally, at supersaturation ratios below 1.15 this method is unable to collect nucleation rate data due to the low number of nucleation events in the experimental time window. This could be resolved by increasing the induction time observation window beyond the four hours chosen. However, while this would give nucleation rates at these conditions, the nucleation rate would be extremely low. Above pH 9.6 there appears to be an increase in nucleation rate, with some experiments where nucleation occurred were for S values below 1 according to the model developed in chapter 3. This suggests that there is a limitation in the model at predicting supersaturation at either high pH values or high ionic strengths as both these values were elevated in the experiments above pH 9.6 (see Table 8.1).

Nucleation is highly sensitive to even minor variations in environmental conditions, such as the introduction of particles, creating more sites for heterogeneous nucleation, or changes in ionic strength, which can affect solution activity and the driving force for crystallization. Nevertheless, conducting a significant number of experiments under consistent conditions can facilitate the collection of sufficient data to accurately describe the statistical probability distribution underlying nucleation events. This explains the apparent transition regions between insufficient and sufficent nucleation and sufficient and excessive nucleation.

4.4.2 Fitting Induction Times to Probability Distributions to Estimate Nucleation Rate

The induction times for each experiment categorized sufficient were fitted to a Poisson distribution based on the following equation:

$$P(t) = 1 - \exp(-JV(t - t_g)) \tag{4.1}$$

where $P(t)$ is the probability of nucleation occurring at time t, J is the nucleation rate, V is the volume, t was induction time and tg was the time for crystals to grow to a detectable size. $P(t)$

was given by

$$P(t) = \frac{M^{+}(t)}{M} \tag{4.2}$$

where $M^{+}(t)$ is the number of experiments with crystals detected at time t and M is the total number of experiments. The fitted induction times gave values for J and t_g.

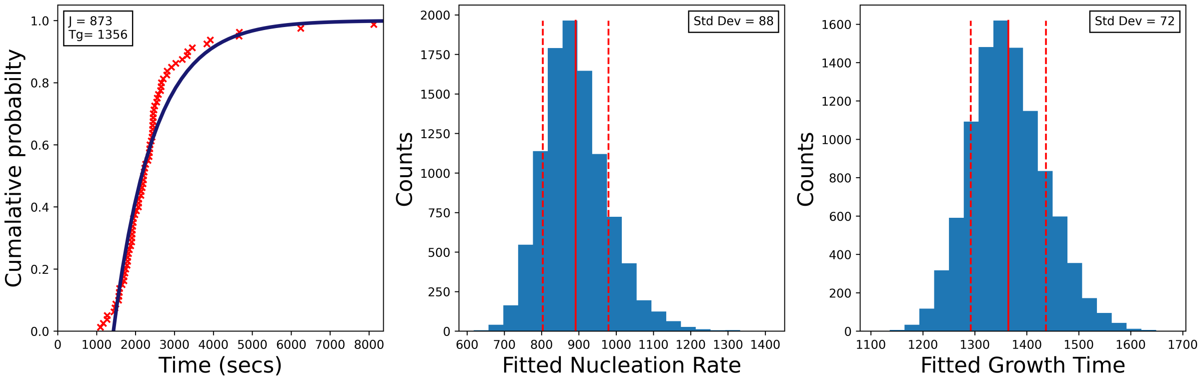

Figure 4.2: An example fit of induction time data to cumulative probability distribution for the determination of nucleation rate and growth time.

In addition, statistical bootstrapping was conducted to estimate the uncertainty of the fitting. This was achieved by selecting a random sample of 80 induction time values from the real experimental data and fitting to the Poisson distribution. This was repeated 10000 times using Python software and the standard deviation of the resultant J and t_g values used as a measure of the error, two standard deviations representing a 95% confidence interval. By using this approach, we were able to estimate the variability in the data and provide a more accurate representation of the range of possible values for the induction times. An example of the poisson fitting and resultant bootstrapping of J and t_g values can be seen in figure 4.2

The nucleation rate data collected shows that nucleation rate increases as supersaturation increases as was expected. It is also apparent that there is a relationship between S and pH and nucleation rate. There are a range of higher pH values at lower supersaturations that achieve similar nucleation rates to high supersaturation values at lower pH values.

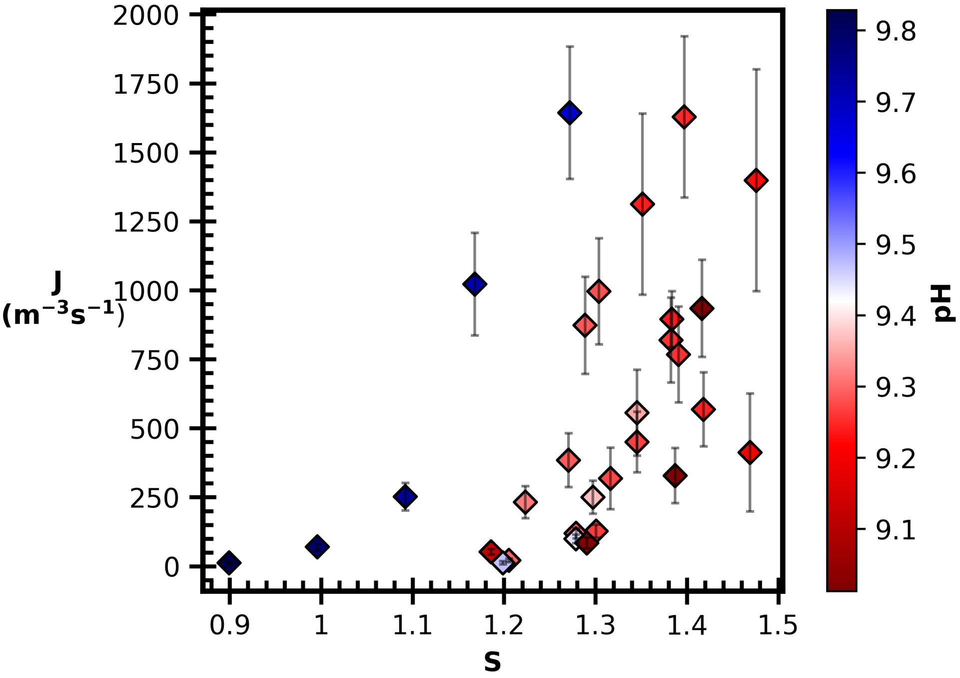

Figure 4.3: Relationship between Supersaturation, Nucleation rate, and pH in a solution. The data points are color-coded based on the pH values represented in a color bar. As the pH increases the colour shifts from blue to red.

4.4.3 Fitting Nucleation Rate Dependence on S and pH

The Kolmogorov-Johnson-Mehl-Avrami (KJMA)(equation 4.3) equation [60][61][62] a commonly used model for predicting nucleation rates in supersaturated solutions[63].

$$J(S) = ASexp\left(-\frac{B}{ln^2S}\right) \tag{4.3}$$

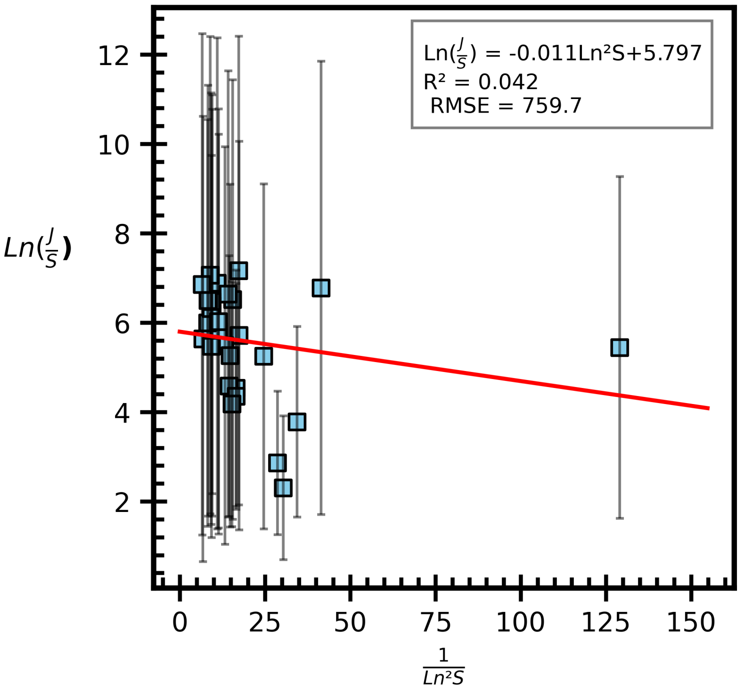

Figure 4.4: Plot of $ln(\frac{J}{S}$ as a function of $\frac{1}{ln^2 S}$ for DL-phenylalanine. Theoretically, identifying the kinetic parameter A and the thermodynamic parameter B of the KJMA equation. Error bars were generated based on two times the standard deviation of nucleation rate values generated from statistical bootstrapping, corresponding to a 95% confidence interval.

To obtain the A and B parameters of the KJMA equation in this system, a linear regression analysis was performed on the acquired nucleation rate data and supersaturation ratios. Specifically, the $Ln^2 S$ was plotted against $Ln(\frac{J}{S})$ and the intercept of the fitted equation was taken as the A value for the KJMA equation, while the B value was obtained from the slope. However, the linear model did not provide a goood fit to the data, as evidenced by the low coefficient of determination (R^2) value of 0.04 for the best fit line. (Figure 4.4). This suggests that other factors may be influencing the nucleation rate besides supersaturation, highlighting the complexity of the nucleation process. However, it is important to note that the error associated with the nucleation measurements is considerable, reflecting the stochastic nature of the nucleation process. This means that there is inherent variability in the data, which should be taken into account when interpreting the results.

The data of J vs S trends upward in a power law fashion (Figure 4.3) however, therefore, it was decided to attempt two fits. First, the data was fitted to a power law regression in a further attempt to establish a quantitative relationship. $S - 1$ was used to ensure that when $S = 1$; $J = 0$. The natural logarithms of $S - 1$ and J were fit to a linear regression (Figure 4.5). This produced somewhat better fitting ($R^2 = 0.225$, indicating that the nucleation rate does indeed increase with increasing supersaturation.

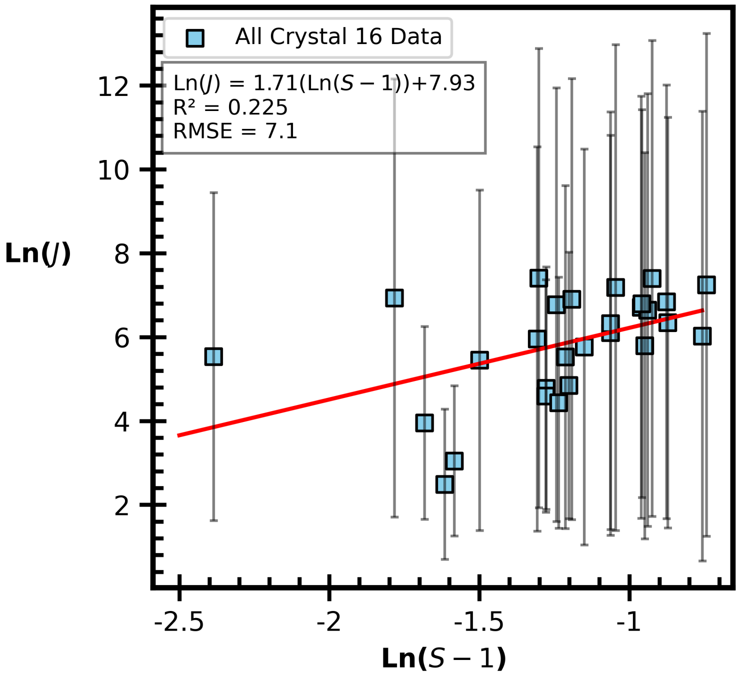

Figure 4.5: The natural logarithm of both nucleation rate and S-1 plotted. A least squares regression was used to fit a linear regression.

As highlighted previously, the supersaturation model used may be limited in its ability to predict S at high pH. Due to the non-linearity of the relationship between J and S any error in the apparent value of S has the potential to greatly hinder attempts to fit J vs S. To attempt to limit the influence of any such error, data from a narrower range of pH values was fitted. Fitting nucleation rate data in this way returns a much better fit. Data was fitted from pH values 9.2-9.5, which included the bulk of the nucleation rate data (Figure 4.6) to give an R^2

value of 0.612.

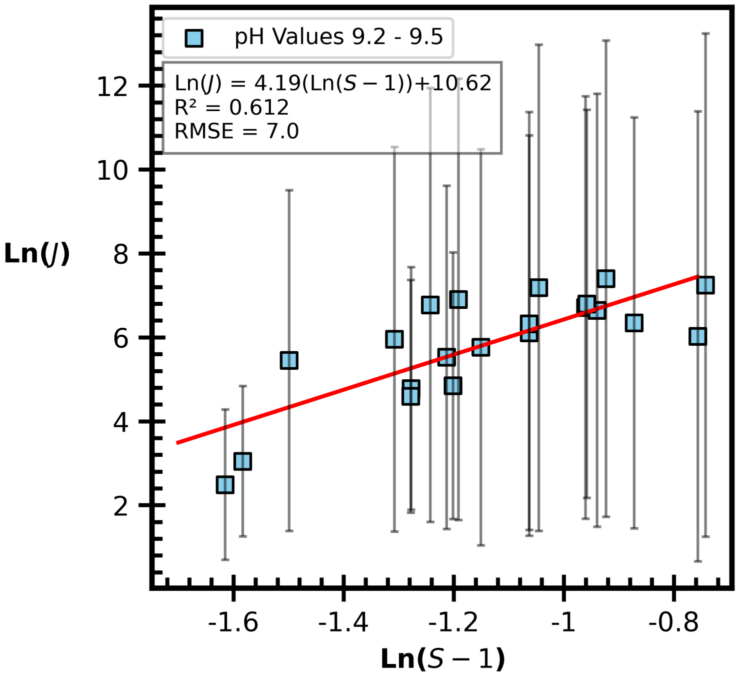

Figure 4.6: The natural logarithm of both nucleation rate and S-1 plotted for pH values in the range 9.2-9.5. A least squares regression was used to fit a linear regression.

The inclusion of pH as a third term in the analysis was explored as a further avenue of investigation. Various models and equations were applied to the data incorporating pH. The pH was also incorporated into the pre-exponential term of the KJMA equation (Table 4.1). The addition of pH to these models did not improve fit quality.

Equation	A	B	C	R^2
$J = A \times (S-1)^B$	310	1.5	-	0.188
$\mathrm{Ln}(J) = A(\mathrm{Ln}(S-1) + B$	1.12	7.36	-	0.225
$\mathrm{Ln}(J) = A \times pH \times \mathrm{Ln}(S-1) + B$	0.16	7.68	-	0.195
$J = A \times pH \times S \exp(\frac{-B}{\mathrm{Ln}^2 S})$	98.54	0.051	-	0.182
$J = (A \times pH) \times S^C \exp(\frac{-B}{\mathrm{Ln}^2 S})$	12.69	-0.002	5.65	0.203

Table 4.1: Table of all fitted equations with their respective coefficients and R^2.

Variable	Coefficient	Std Error	P-value
Constant A	2677	1010	0.793
$S-1$	3919	970	0.001
pH	-891	1305	0.502
Ii	8198	3950	0.049

Table 4.2: Table of coefficients for multi-linear regression analysis, fitting $S-1$, pH and Ii as independent variables and J as the dependent variable

Finally, a multi-linear regression (MLR) was conducted using original least squares regression. The dependent variables were $S-1$, pH, and solution ionic strength (Ii) in the algebraic form:

$$J = A + B \times (S-1) + C \times pH + D \times Ii + error \tag{4.4}$$

The results (Table 4.2) show that the only variable with a statistically significant impact on the nucleation rate, when fitted in this way, is S-1 as indicated by the only P-value below 0.05. In addition, the fit was not very good, with an R^2 value of 0.496, meaning the predictive power of the model would be poor, but the correlation coefficient, R, of 0.704 indicates that there is a clear relationship between these variables, most notably: S-1.

The multi-linear regression was also applied in the same manner to Ln(J) and Ln($S-1$) (Table 4.3).

$$\text{Ln}J = A + B \times \text{Ln}(S-1) + C \times pH + D \times Ii + error \tag{4.5}$$

The R^2 value for MLR of LnJ and Ln$S-1$ was 0.564, the best fit model discovered. For both models, the P-value for ionic strength was statistically significant, indicating that this variable is affecting nucleation rate. This may be, however, confounded by the weakness of the solubility

Variable	Coefficient	Std Error	P-value
Constant A	60.68	23.3	0.2
Ln$S-1$	3.01	0.631	0.0008
pH	-4.05	3.08	0.201
Ii	27.28	9.49	0.008

Table 4.3: Table of coefficients for multi-linear regression analysis, fitting Ln$S-1$, pH and Ii as independent variables and LnJ as the dependent variable.

model in predicting supersaturation ratio at higher ionic strengths. A deeper analysis into the effect of ionic strength, through the application of a more detailed solution activity model may reveal a more quantitatively accurate relationship between these quantities.

4.5 Conclusions

This study aimed to explore the relationship between nucleation rate, supersaturation and pH in DL-phenylalanine crystallization. Nucleation rate was obtained from the fitting of induction times to a cumulative probability distribution at each condition. Nucleation rate data is successfully obtained at high pH, where solubility is increased with respect to the neutral species. There is a clear relationship between supersaturation and nucleation rate within a narrow range of pH values although this data is rather noisy. There may be a relationship between nucleation rate and pH, however, it is difficult to state this with a degree of certainty due to a relatively narrow range of pH values covered and the apparent limitations of the model used for capturing supersaturation at high pH values. It is difficult to establish any predictive relationship between nucleation rate and supersaturation. While the pH seems to alter the nucleation kinetics of the system as evidenced by the lower supersaturation values required for sufficient nucleation at higher pH (Figure 4.1). This may be due to the effect of the ions added to control the pH affecting the solution activity. Applying the collected data to previously established models, such as the KJMA equation, does not produce a statistically good fit.

In this work we also applied the data to other empirical models to see if there was any way of generating a new predictive tool for this kind of data. While it was possible to determine a correlation between nucleation rate and supersaturation ratio in narrow ranges of pH value, for the full data set all models studied failed to produce satisfactory results. The overall inability to find a model to fit this data is believed to be in part due the significant window of error in nucleation rate values. Due to the stochastic nature of nucleation, repeated experiments under identical conditions can produce highly variable results. The collection of a large number of induction times is a method used to try and iron out the natural error in nucleation studies and allow the empirical fitting of the data to models, such as the classical nucleation derived KJMA equation and others.

Future study in this area could be conducted in a few ways. The first step would be to increase the amount of data collected, as the 24 nucleation rates obtained in this work were insufficient to fit any empirical models accurately. Moreover, the pH range studied in this work is quite narrow, spanning only one pH unit. Exploring a broader range of values could lead to a greater understanding of the effect of pH on nucleation kinetics. Increasing the quantity of data collected would be quite labour intensive, however, this could feasibly be streamlined with the use of robotics and automated dosing machines. With more data available come more opportunities for analysis; a large data cloud would open up the possibility of applying machine learning to the data set, which may provide greater insight into nucleation kinetics in pH-shift crystallizing systems.

Chapter 5

The Development of a Novel Microfluidic Device for the Study of pH-Shift Crystallization

5.1 Introduction

Crystallization process control relies on a deep understanding of numerous fundamental parameters such as temperature, supersaturation, solvent composition and pH among others, each affecting crystallization kinetics and crystal product quality attributes. These factors interact with one another in complex ways, making precise control challenging. A deep understanding of such operational parameters and their affects on crystallization is therefore necessary for optimum crystallization control. Microfluidic technologies have emerged in recent years as a novel method for exploring crystallization fundamentals.

Microfluidics offer the ability to tightly control crystallization conditions [64][8]. The small volumes involved in microfluidics can be tightly temperature controlled without the need to be worried about convection currents [20]. Volumes can be adjusted with a high degree of precision. Microfluidics are limited to laminar fluid flow, meaning high quality crystals can be formed without being subjected to excessive fluid shear. Large surface to volume ratios, individual crystal confinement and microgravity also present opportunities for interesting investigations into crystallization and product quality attributes attained through refined supersaturation control. In addition, microfluidics allows for the generation of hundreds of simultaneous, independent crystallizing reaction vessels. The high-throughput nature of such devices allows for the collection of large quantities of data that would require a significantly greater number of experiments to match under conventional circumstances. This is of particular value in studying stochastic processes such as nucleation kinetics.

Microfluidics involves the use of networks of channels or structures to manipulate fluid in the microlitre to picolitre range. In general terms, microfluidics can be used to describe a technical apparatus where one of the features of the microfluidic structure has an internal diameter of less than 1 mm. Some of the advantages of microfluidics include: Laminar flow, which can be mathematically modelled; easy automation through the use of microvalves and micropumps; quick, cheap fabrication of devices which can allow for rapid prototyping; reduced reagent cost due to smaller quantities used; compactness and portability [65]. Therefore, Microfluidics can be useful in a wide range of fields, such as biotechnology, cosmetics and pharmaceuticals.

5.2 Aim and Objectives

The key aim of this work is to develop a microfluidic device for the collection of nucleation rate data. The key requirements of such a device are that it must firstly be able to generate supersaturated droplets through mixing of a high pH solution containing a high concentration of the analyte of interest, phenylalanine, and a low pH solution. This will generate supersaturation in a manner described in figure 2.5. The second key specification is that droplets generated are stored in a stable location that can be observed using optical microscopy for a sufficient period of time to observe nucleation.

5.3 Materials and Methods

5.3.1 Materials

DL-phenylalanine (DL-phe; Sigma-Aldrich,$\geq$ 99%) was used as purchased. Sodium Hydroxide (anhydrous, Sigma-Aldrich, $\geq$98%) was used as purchased. Hydrochloric acid solution 37% HCl (ACS, Sigma-Aldrich, reagent) was used as purchased. Fluorinet FC-40 oil (Sigma-Aldrich) was used as purchased. #008 Fluorosurfactant (Ran Biotechnologies, Beverly, MA, USA) was used as purchased. Polydimethylsiloxane (PDMS, Sylgard 184, Dow, MI, United States) was used as purchased. Curing Agent (Sylgard 184 Curing agent, Dow, MI, United States) was used as purchased. Methanol (VWR, Lutterworth, UK) was used as purchased. Isopropanol (VWR, Lutterworth, UK) was used as purchased. Acetone (VWR, Lutterworth, UK) was used as purchased. 1H, 1H, 2H, 2H-perfluorooctyl-trichlorosilane (Silanizing agent, Sigma Aldrich, UK) was used as purchased. SU8 3035 photoresist (MicroChem, Newton, MA, United States) was used as purchased.

Solvents The solvents and media used were aqueous Sodium Hydroxide (NaOH) solution, aqueous Hydrochloric Acid (HCl) and water. Aqueous solutions of NaOH were prepared by dissolution of a known accurate quantity of pure NaOH pellets in approximately 70 mL of water in a volumetric flask. Water was then added to the flask up to the volume line, indicating 100 mL of solution to produce a solution of predetermined concentration. The flask was then inverted multiple times to ensure robust mixing. Aqueous solutions of HCl were prepared by mixing a known accurate mass of 37% HCl solution in approximately 70 mL of water in a volumetric flask. Water was then added to the flask up to the volume line, indicating 100 mL of solution to produce a solution of predetermined concentration. The flask was then inverted multiple times to ensure robust mixing.

5.4 Device Fabrication

Devices were fabricated using standard photolithography and soft-lithography techniques [66–68].

The microfluidic devices developed for this work were composed of a single layer of the elastic polymer bonded to a glass slide. A master wafer was designed and fabricated through photolithography with the desired pattern a bas-relief of SU8 3035 photoresist printed onto a silicon wafer. The PDMS layer was created by flowing uncured elastomer onto the silanised master wafer and cured, leaving the inverse of the pattern imprinted into the PDMS which when bonded to the glass slide forms the desired channels.

The desired master wafer pattern was designed using CorelDRAW Graphics Suite (Corel Corporation, Ottawa, Canada). The design was printed by JD Photo Data (Hitchen, UK) as either glass or acetate photomasks. The design of the photomask dictated the 2 dimensional features of the device while the depth of the features was controlled by the thickness of the layer of photoresist used.

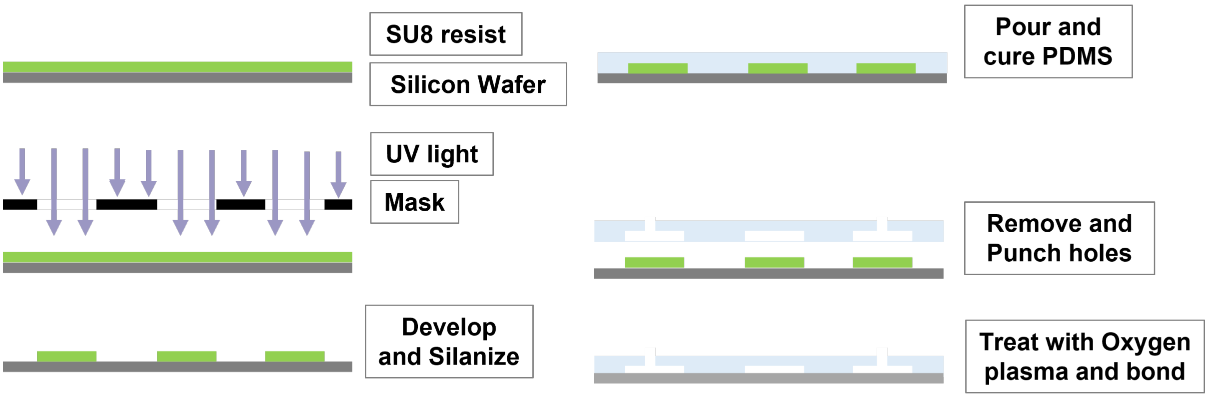

Figure 5.1: Schematic of the process of microfluidic device fabrication.

Silicon wafers were cleaned of debris by sequential sonication in acetone, methanol and iso-propanol (IPA). Residual solvent was removed from the wafer by blasting with nitrogen gas and then heating to 180 °C on a hot plate. After cooling to room temperature photoresist was spin coated onto the wafer, giving an even coating of desired thickness. The wafer was soft baked to a maximum of 95 °C on a hotplate. The photomask was placed on top of the photoresist prior to exposure to collimated UV light. The surfaces exposed by the mask to UV light are caused to crosslink, leading to hard, insoluble features. The wafer was then baked once more. After cooling, the wafer was immersed in MicroPosit EC solvent which dissolved any photoresist that had not been subjected to UV exposure leaving behind the hard, crosslinked patterns on the wafer.

After development, the wafer was once more rinsed with IPA before a final period of baking. At this point the depth of the features on the wafer were measured with a stylus profilometer(Alpha-

Step IQ, KLA Tencor, Milpitas, California, United States). To prevent PDMS adhesion to the silicon master, the surface was silanised by vapour deposition of 1H,1H,2H,2H-perfluorooctyltrichlorosilane for one hour. A glass petri dish was wrapped in tinfoil and the silanised wafer placed therein.

Uncured PDMS, mixed with 10% curing agent, was poured onto the master wafer to fill the tin foil mould. A dessicator was used to degas the PDMS, removing any air bubbles and the master was then baked in the oven at 70-80 °C for 2 hours to cure the PDMS. The moulded PDMS devices were extracted from the mould using a scalpel. G21 biopsy needles were used to punch holes for inlet and outlet ports to connect tubing to syringe pumps. Devices and glass slides were cleaned with adhesive tape to remove any debris. Both PDMS and slide were treated within an oxygen plasma chamber (Pico A, Diener Electronic, Germany) for 0.3 minutes at 60% power. Oxygen plasma exposure causes changes in the chemical structure of PDMS. Methyl groups in the repeating -O-Si-(CH3) are replaced with polar silanol (SiOH) groups [66]. This causes PDMS to form irreversible covalent bonds with the glass it comes into contact with. Treated PDMS was placed on to the treated glass slide and compressed to ensure no air was trapped. Bonded devices were treated with undiluted Aquapel (PPG Industries Inc., Pittsburgh, United States) to obtain hydrophobic channel surfaces, promoting wetting of the channel surfaces to oil.

5.4.1 General Syringe Pump operation

Liquids were introduced in to the device using syringes, pumps and tubing. Glass hamilton syringes were used as a reservoir for the fluid prior to injection into the system. PTFE tubing was used to connect the syringe to the inlets on the microfluidic device. The tubing and the syringe were attached using a needle. A tight fit was required to prevent any liquid escaping the system through any gap between the needle and the tubing. The syringe was driven using a

Aladdin Single-Syringe Pump (High Pressure World Precision Instruments, FL, USA).

The flow rate on the syringe pump is controlled by adjusting the rate at which a rotating screw turns, depressing the syringe plunger. This conversion of turn rate to flow rate is calculated by the pump from the internal diameter of the syringe barrel. A result of this mechanism is that a wider internal diameter syringe is not able to pump as slowly as a narrower internal diameter syringe due to the lower limit of the pump's minimum screw speed. In addition, at slow screw rotation the pump is forced to toggle the screw on and off at a rate of approximately 3 Hz, rather than apply continuous screw pressure to the syringe plunger. To counter this, it was desirable to use a syringe with as small an internal diameter as possible. Experiments were conducted using a 250 μl glass Hamilton 1700 series syringe (Hamilton Company, Reno, NV, USA) with an internal diameter of 2.3 mm. A smaller, 50 μl 1700 series syringe with 0.729 mm internal diameter was tested to determine if results were better, however, the extremely thin plunger was found to be very flexible and this led to inconsistency in operation. It was sometimes observed that the flows within the device appeared to oscillate slightly, particularly at the mixing Y section of the droplet forming junction. It is unclear if this was a result of the variation or if it actually had any impact on droplet mixing, therefore, it is assumed that the headline flow rate of the syringe pump was representative of the flow rate at the junction.

Care was taken to minimise any compliance in the fluid injection system to ensure consistent pressures. Compliance leads to a difference between the headline flow rate at the syringe pump and the actual flow rate at the device inlet. The presence of air anywhere in the system leads to significant levels of compliance. Under the pressures used in the system any air compresses and this significantly alters the flow of fluid. As such, all air had to be removed from the system prior to connection to the device. Glass syringes were chosen specifically for the purpose of reducing compliance. Plastic syringes were found to flex. There was limited flexibility in the PTFE tubing.

Once droplets formation was well established and sufficient droplets in the storage location the inlet and outlet tubings to and from the device were simultaneously severed with sharp shears. This was done to ensure the immediate cessation of droplet formation. If only the inlets are severed the fluid in the outlet will either backflow into the device or negative pressure will continue to pull droplets from the device into the outlet tubing. Tubing was severed within 30 mm of the connection with the device. If the severed tubing leaves differing lengths or heights of tubing the subsequent pressure differences can cause droplets to move which causes problems for droplet observation and tracking. Image acquisition began within 30 seconds of severing the tubing on the device.

5.4.2 Microscopy

A Zeiss Axiovert 5 microscope (Zeiss, Cambridge, UK) was used to image the microfluidic devices. Images were acquired using a Labview controlled Dalsa Genie CMOS HM1024 camera (Phase 1 Technology Corp, NY, USA). Images were either taken as single snaphots or, more commonly, as a time lapse with images taken at regular intervals. Single images were analysed using ImageJ. For large sequences a program was written using MATLAB to determine the time of nucleation within each droplet. This software worked by tracking each droplet through each image in the sequence and recording the average pixel intensity within the droplet. The droplet pixel intensity for each image was compared to a moving average and if these values sharply deviated, this was taken as the moment of nucleation and was verified by visual appraisal.

5.4.3 Crystallization Process Control

There are numerous methods for generating the supersaturation required to cause crystal nucleation. Temperature control, used in systems where the solubility at high temperatures is greater than that at low temperatures, can be used to supersaturate by taking a solution at high temperature to a low temperature where the solution is supersaturated. This requires a model compound that has a very high degree of temperature dependence to generate high levels of supersaturation. As nucleation induction time is linearly dependent on volume. The volumes of microfluidic droplets are orders of magnitude smaller than even the low volumes used in the previous chapter. It was therefore hypothesized that in order to compensate for the decreased volumes supersaturation would need to be greatly increased. The temperature dependent solubility of the model compound in water would at most allow for a supersaturation ratio of 2.5. This was thought unlikely to be sufficient headroom in the experimental space to conduct experiments.

Evaporative crystallization has also been used in microfluidic devices for the crystallization of proteins, exposing the solution to air through an evaporation chamber[69].

Vapour diffusion works through a similar method, utilizing the permeability of PDMS to water. One such method has been previously presented that allows for precise control of crystallization conditions in the Crystallization of monoclonal antibodies[70]. This technique relies on the selective permeability of PDMS to water to control the final concentration of droplets. A reservoir of specific water activity is separated from the droplets containing water, solute and precipitants by a PDMS layer. The difference in water activity draws the solvent from the droplets, increasing the concentration. While this method was considered viable it was not prioritised due to increased complexity in fabrication. However, the effect of water pervaporation on solution concentration and supersaturation can have a major effect on crystallization in PDMS based microfluidic deices.

Anti-solvent addition is a common technique for generating supersaturation. In this process, the addition of an antisolvent, in which the solute is highly insoluble, reduces the overall solution equilibrium solubility at a greater rate than dilution brings down the solution composition leaving the solution in a supersaturated state. This system allows generation of sufficient supersaturation and requires relatively simple geometry to achieve. pH-shift crystallization is a form of reactive crystallization that can be achieved in a very similar manner through simple mixing on the device. A high pH solution of sodium hydroxide and model compound was mixed in the devices with a low pH solution of hydrochloric acid. Due to the high supersaturation ratios required for crystallization in the microfluidic device it wasn't possible to measure the pH of the solution outside of the device as any crystallization would alter the pH.

Therefore, it was required to calculate the solution pH *in silico*. The supersaturation modelling software developed in Chapter 3 was used to predict the solution pH and supersaturation for the experiments conducted in this chapter. The program uses the concentrations of NaOH, HCl and model compound and, utilizing the pKa of the model compound and the solubility of the neutral species returns the solution concentration, the pH and the supersaturation. The input concentrations were adjusted until a desirable pH and supersaturation profile was reached. These concentrations were then manufactured in the laboratory and used for experiments in the microfluidic device. The concentrations were initially calculated at equal flow rates, however, by adjusting the flow rates in favour of either element of the crystallizing mixture could be used to alter the pH and supersaturation and the program also had this capability.

5.5 Device 1 - A Single Chamber Device

5.5.1 Device Specification

As stated above, the goal of the project was to design and utilise a microfluidic device for the purpose of analysing crystal nucleation and quantifying crystal nucleation rates from the probability distributions of induction times. The design of the device had several key specifications in order to meet this objective. 1: The device was required to create a supersaturated solution in the metastable zone in droplets ∼1nl in volume. 2: the droplets would be transported to a location where they would be stably stored for a sufficient period of time for nucleation to occur. 3: the nucleating droplets had to be observable for the duration of the experiment using a microscope.

5.5.2 Design of the Device

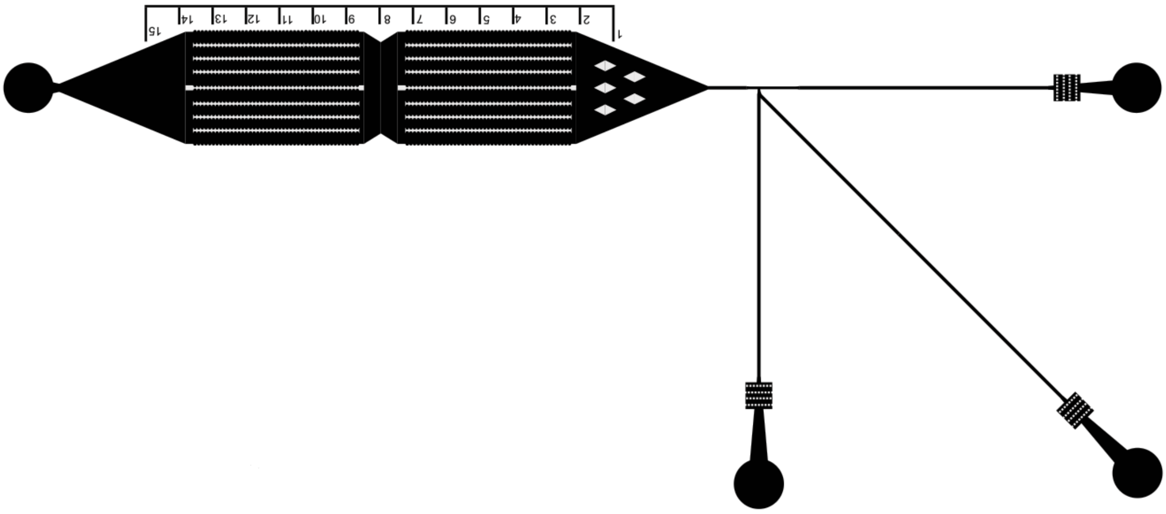

Figure 5.2: A Microfluidic design 1

The design of this device [71] was fabricated on a silicon wafer using SU8 3035 photoresist in a single layer 40 μm in thickness. The device was composed of two main sections: A junction for mixing and forming droplets and a chamber for droplets.

Junction

The aqueous and continuous phases were introduced to the device through tubing connected to 1 mm holes cut in the PDMS with a biopsy punch. Each inlet led to a filter for preventing large particulates from entering the mixing and droplet forming junctions of the device potentially causing blockages in the device. This filter comprised of a matrix of PDMS columns with spaces of 28 μm between columns to allow fluid to flow through, but catch and stop large particles such as fibres passing through. The droplet forming junction started with a Y-type junction for mixing together different aqueous solutions to form a supersaturated solution for crystallization. It was essential that the crystallizing solution was mixed in situ and immediately encapsulated into droplets. The ratio of solution and precipitant is critical to crystallization process control. This is managed by the flow rates of syringe drivers used and can be confirmed visually by assessing the interface between the two flows seen at the droplet forming junction (Figure 5.3). Following this, the solution was encapsulated as water in oil droplets at a T junction. At this junction, the immiscible continuous and aqueous phases form an interface. The aqueous phase pushes into the continuous phase, blocking that stream. Pressure builds up in the continuous phase channel causing the aqueous protrusion to distort down stream of the main channel. The upstream interface of the aqueous is pressed towards the downstream edge of the junction until the continuous phase completely severs the new droplet from the aqueous inlet.

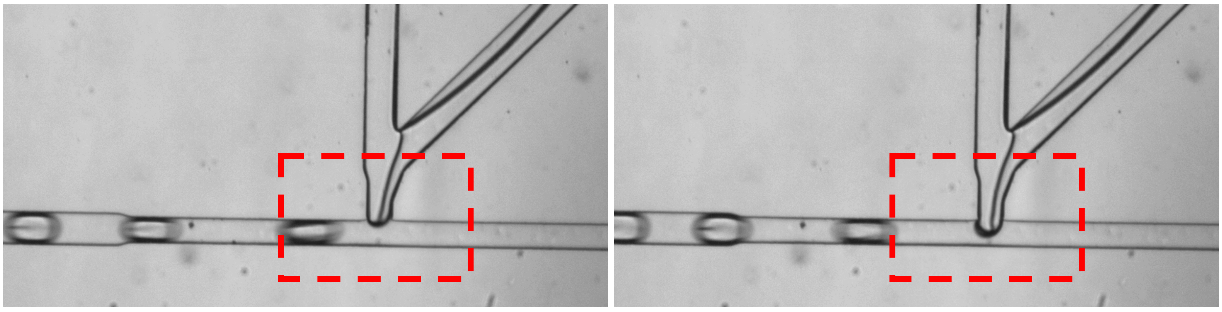

(a) The interface between continuous and aqueous phase

(b) The intrusion of the aqueous phase into the main channel

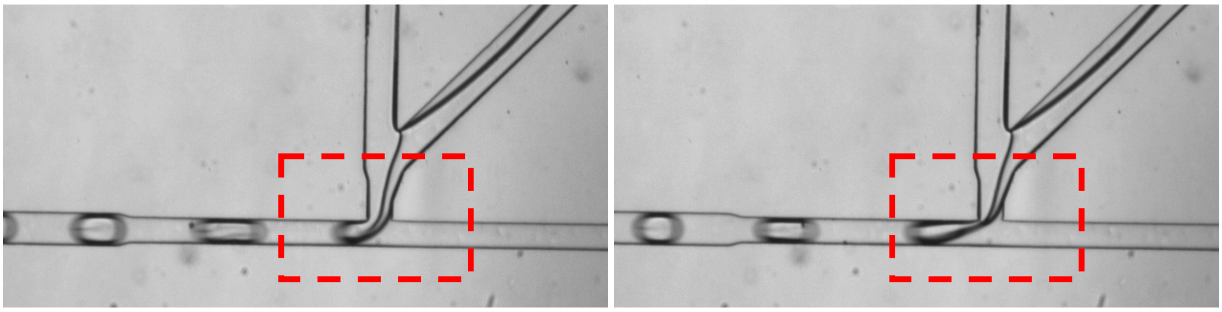

(c) The aqueous phase is distorted by the increased pressure enacted by the continuous phase

(d) As the trailing interface reaches the upstream edge of the inlet the new droplet is severed

Figure 5.3: Still images of the formation of droplets at the T junction. The interface of the aqueous flows can be seen bisecting the aqueous phase at the junction and this phenomenon is also observed in the droplet plugs themselves as they progress down the channel.

Storage Chamber

The storage chamber was walled with scalloped edges to trap droplets in position allowing for long term analysis. The chamber was supported with long pillars traversing the length of the chamber which were also scalloped. The maximum width of the chambers were 3.45 mm. A numbered scale was drawn at the side of the chamber to aid droplet tracking.

5.5.3 Operation of the Device

Initial experiments were conducted with solely water as aqueous phase to test flow rates for optimum droplet size and consistency. The continuous phase was FC-40 fluorinated oil with 2% fluorosurfactant. Continuous flow rate used was 0.14 ml/hr, aqueous flow rate used was 0.12

ml/hr. The syringes were driven at a continuous rate for five minutes to allow equilibration of the pressure in the system. After equilibration the storage chamber was filled with droplets and the tubing severed to begin observation.

5.5.4 Successes and Weaknesses of Device

The droplets formed at the junction were of consistent volume and composition which were the key requirements of the droplet forming junction.

At high flow rate the interface between the two aqueous inlet flows can be observed (Figure 5.3). The interface bisects the volume between the Y-junction and the T-junction, indicating that the droplet contains equal volume of solution from each inlet. This same interface can also be observed in the droplets themselves that flow down the channel (Figure 5.3). This seems to confirm that droplets were composed of equal volumes of both aqueous solutions, which is to be expected with equal flow rates. This, however, is something of an informed assumption. Confirmation of the exact internal solution composition of droplets would require use of some kind of fluorescent molecule in one of the solutions and measurement of the fluorescence intensity in the final droplets. However, this would lead to interference in the crystallization process and could alter nucleation rates. The droplet forming junction was deemed to be a successful geometry and suitable for use in this work with the concession that absolute accuracy of mixing can only be assumed and not validated.

The storage chamber design was found to be ineffective for the purposes of this work. Firstly, once the droplets were formed and the flows of the aqueous and continuous phases were ceased, coalescence occurred very quickly, often in as little as 10 minutes. This meant that droplets would no longer be of consistent size and volume and larger volumes would lead to higher rates of nucleation. Secondly, droplets were not able to be stored in a consistent location. Droplets would collect in the middle of the device due to the hydrophobic coating on the walls of the device. The scalloped walls then had no effect on the droplets and so they were able to move freely over time and so monitoring for nucleation was made significantly more difficult. Therefore, a different device was required.

5.6 Device 2 - A Hydrodynamic Trap Device

Device 1 identified that the droplet forming junction was suitable for further use, however, more development was required to produce a suitable storage matrix for monitoring droplets over three to four hours. It was also at this point that the addition of an accessory pathway for a reservoir of osmotically balanced fluid to hydrate the PDMS. PDMS is permeable to water and therefore, an aqueous droplet present in the device will lose a volume of water to the PDMS which will further concentrate a supersaturated droplet, increasing the nucleation rate.

5.6.1 Design of the Device

Based on designs by Bokellal et al. and Vanapalli et al. [72][73] this device followed the pattern set by the previous device by consisting of a droplet forming junction and a storage matrix for droplet crystallization and observation. This device was fabricated on a silicon wafer using SU8 3035 photoresist in a single layer 60 μm in thickness.

The storage chamber consists of a serpentine of hydrodynamic traps and bypass channels which allow droplets to flow around filled traps. As with the previous device, aqueous solutions are mixed by a Y-junction immediately precedent to a T junction where the aqueous and continuous flows meet and form a water in oil droplet. Between the droplet forming junction and the trap serpentine an intermediate outlet channel was situated. The purpose of this outlet was to allow equilibration of the droplet forming junction without the products flowing into the traps. When aqueous inlets are initiated it takes a series of adjustments to remove excess air from the channels, to bring both flow rates up to the required levels and to allow the pressures and compliance within the system to equilibrate to the new conditions. Any aqueous droplets produced during this adjustment period would be of uncertain composition and those that flowed into the serpentine would be of trapped and would not be appropriate for crystallization and analysis. Coupled with the speed of droplet production, this would quickly fill the entire serpentine, thus rendering the device useless. The intermediate outlet was designed such that when this channel was open to the atmosphere, the resistance in this channel would be inferior to the resistance of the serpentine. The droplets would therefore preferentially flow into the intermediate outlet, protecting the serpentine. When the adjustment period was complete, the intermediate outlet would be sealed, massively increasing the resistance to far greater levels than the serpentine and allowing droplets to flow into the serpentine for trapping, crystallization and analysis.

In addition to the functioning device, accessory channels were added to control the hydration of the PDMS to prevent evaporation of water from the droplets. Flowing a solution of equal water activity to the droplet water activity through an external channel would hydrate the PDMS and prevent water pervaporating from the droplet and affecting the concentration.

Trap Function

Each trap consisted of a storage chamber 500 μm in diameter connected to a narrow restriction channel and a broader, but longer bypass channel. The trap functions by utilizing the changing resistance across the trap unit caused by introduction of an aqueous droplet. When no droplet

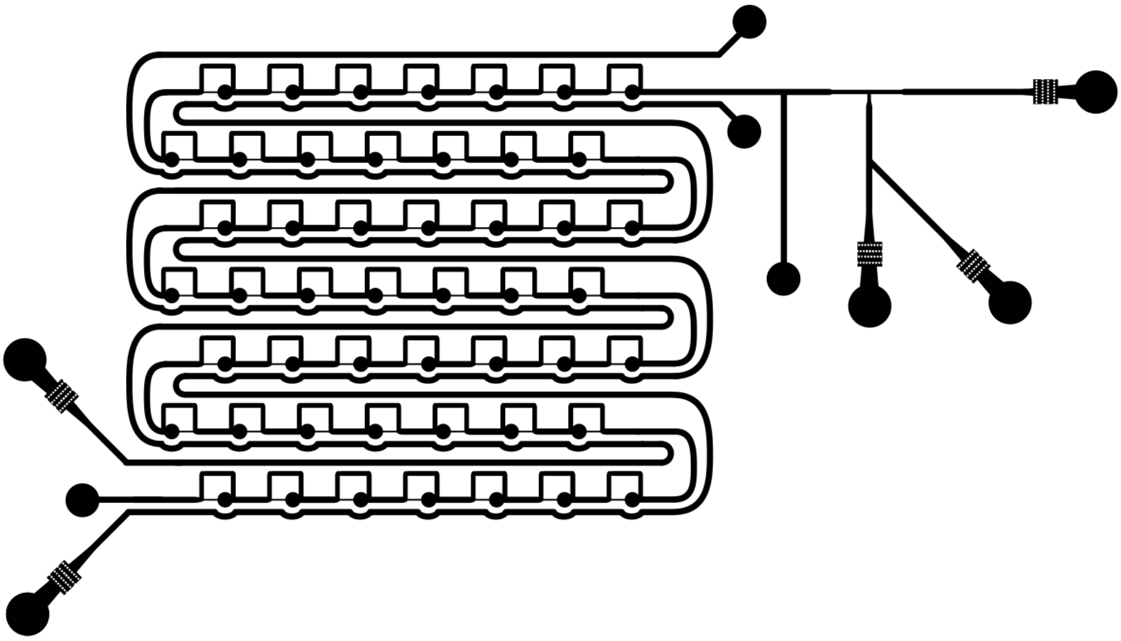

Figure 5.4: A Microfluidic design 2

is present in the trap chamber (Figure 5.6a) the path of least resistance is across the narrow, restriction channel. This draws a droplet into an empty chamber (Figure 5.6b). The presence of a droplet in the trap greatly increases the resistance across the restriction channel which switches the path of least resistance to the bypass channel causing future droplets to pass around the trap (Figure 5.6c). The effect of this is that any empty traps will be filled by droplets and held there securely. For this geometry to function correctly, however, it is necessary that the ratio between the hydraulic resistance of the bypass channel and that of restriction channel must promote trapping. In addition, the restriction channel must be sufficiently resistant to prevent the trapped droplet deforming and passing through the channel. The resistance through each channel in the device was calculated using the following equation

$$R = \frac{12\mu L}{wh^3}\left[1 - \frac{192}{\pi^5}\left(\frac{h}{w}\right)\right]^{-1} \tag{5.1}$$

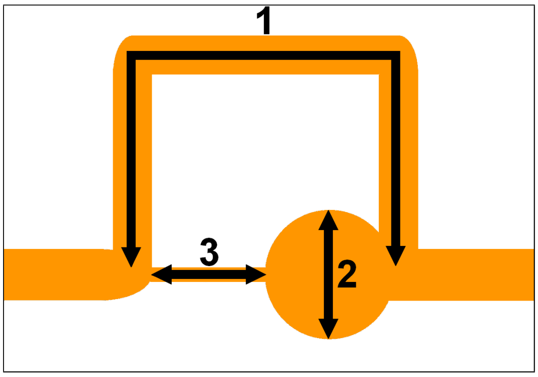

Figure 5.5: Segment 1 is the bypass channel, circumventing the main trap. Segment 2 shows the storage chamber itself where a droplet will eventually be trapped. Segment 3 is the narrow, restriction channel which pulls the droplet into the chamber but is subsequently blocked by the trapped droplet.

where μ is the dynamic viscosity; L is the length; w is the width and h is the height of the channel. The resistance for each segment was calculated. The resistance ratio between the restriction/chamber segment (Figure 5.5.2 5.53) and the bypass channel (Figure 5.5.1) needs to be less than one for the device to effectively trap a droplet in the chamber.

Chamber	Bypass Channel	Restriction Channel	Restriction Channel and Chamber	Resistance Ratio
D = 500 μm R = $2.46x10^{11}$	L = 2650 μm W = 150 μm R = $5.37x10^{12}$	L = 435 μm W = 55 μm R = $5.71x10^{12}$	R= $5.96x10^{12}$	1.11

Table 5.1: Dimensions of chamber, restriction and bypass channels and calculated resistance values for hydrodynamic trap device.

5.6.2 Operation of the Device

The operation of the device was conducted in much the same way as device 1. However, due to the larger droplet chambers, a different ratio of flow rates were tested with water and continuous

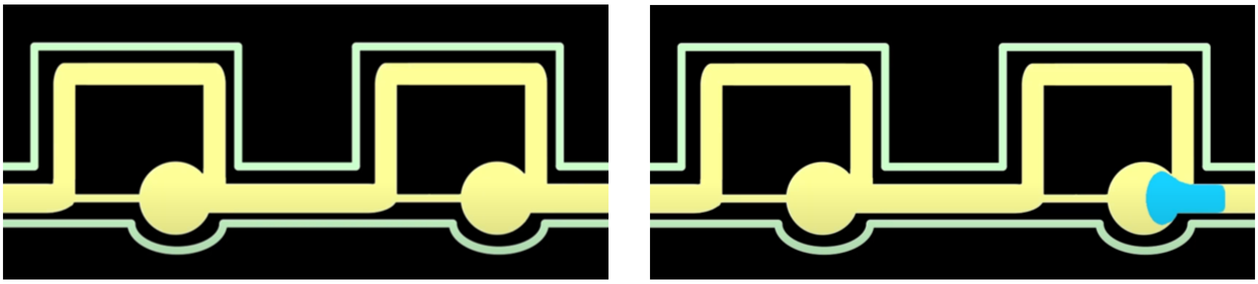

(a) The empty chamber allows fluid to flow across the restriction chamber.

(b) A droplet, when presented to an empty trap, is drawn into the chamber, thus blocking the restriction chamber.

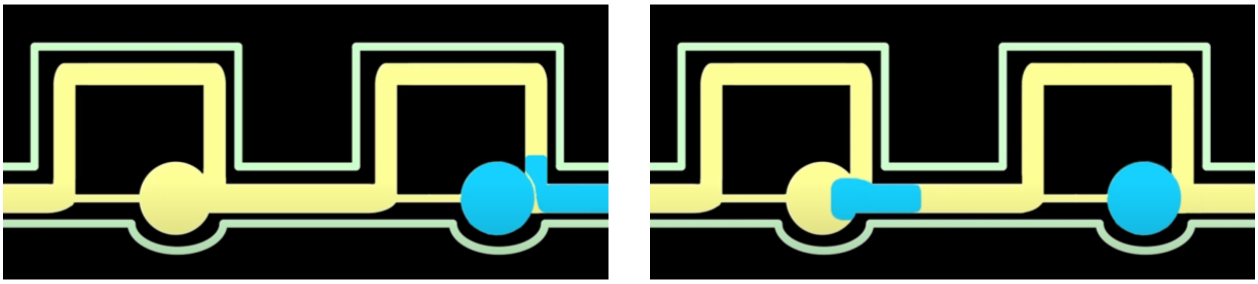

(c) The trap is now blocked and the bypass channel now has lower resistance, causing any new droplet to flow past filled traps

(d) The droplet will fill the first empty trap it comes across

Figure 5.6: Schematic of microfluidic trap function

phase to adjust droplet size to fit. If the droplet was too large, then it would protrude into the bypass channel, altering the fine balance of resistances and encouraging displacement from the chamber. Smaller droplets had the potential to be trapped, however, multiple droplets could then get drawn into the chamber, affecting coalescence.

In addition, initial experiments were conducted to assess the best utilisation of the intermediate outlet. The purpose of this outlet was to allow equilibration of the droplet forming junction without the products flowing into the traps. When aqueous inlets are initiated it takes a series of adjustments to remove excess air from the channels, to bring both flow rates up to the required levels and to allow the pressures and compliance within the system to equilibrate to the new conditions. Any aqueous droplets produced during this adjustment period that flowed into the serpentine would be trapped and would not be appropriate for crystallization and analysis.

Coupled with the speed of droplet production, this would quickly fill the entire serpentine, thus rendering the device useless. The intermediate outlet was designed such that when this channel was open to the atmosphere, the resistance in this channel would be inferior to the resistance of the serpentine. The droplets would therefore preferentially flow into the intermediate outlet, protecting the serpentine. When the adjustment period was complete, the intermediate outlet would be sealed, massively increasing the resistance to far greater levels than the serpentine and allowing droplets to flow into the serpentine for trapping, crystallization and analysis.

However, applying this theory in practice proved a fatal flaw for this device in conducting further experiments. The challenge that presented was the closing of the intermediate outlet without disrupting the equilibrium. Initial attempts involved the connecting to the outlet of a short section of tubing and inserting a solid plug into the end to increase the resistance. However, the insertion of the plug created a back pressure which caused disruption. Clamps were applied to the tubing to create a seal, however, it was impossible to form a perfect seal consistently and even when a seal was temporarily formed the equilibrium would be altered. One option that could have been explored would have been the use of some sort of gate valve, however, it was not possible to acquire one for this work.

5.7 Device 3 - A "Dropspot" Storage Device

5.7.1 Design of the Device

Following the difficulties encountered with device 2 it was decided to pivot back to what had worked somewhat before, but with a key variation. The "Dropspot" device is based on the design by Schmitz et al. [74]. Incorporating the very successful Y-T junction for mixing and droplet formation, this device utilizes a storage matrix with similarly scalloped walls as to the single chamber device initially tested. The key difference, however, is that this device makes use of a series of divided channels with scalloped walls to create chambers for trapping a line of single droplets in each channel but maintaining a degree of separation between droplets; the goal being to prevent the coalescence observed in the first device. The device contained 2128 150 μm diameter chambers within the storage array which was hoped to be suitable for longer term storage. The devices were fabricated using a single SU8 3035 layer to create well defined, 58 μm thick features. The constrictions between each chamber had to be less than 50% of the width of the channel diameter to prevent trapped droplets moving between chambers. Therefore the constrictions were 70 μm. The interfacial tension acts to conform the droplet to the geometrical shape that minimizes the surface area for a given volume. In order to dislocate the droplet from the chamber, energy is required to deform the droplet. This means that while the syringe pumps are flowing, the droplets can be deformed and pushed through the chambers. When flow is stopped, the droplets should be trapped in position for monitoring. In addition, the droplets were surrounded by a layer of continuous phase, preventing droplets contacting and coalescing. The device contained a large, open antechamber prior to the storage matrix for droplets to transition en route to the matrix channels. The bypass channel was included to apply extra continuous phase pressure to the system to encourage droplets from this region and into the matrix. The volume of droplets captured were approximated using the equation for the volume of an ellipsoid:

$$V = \frac{4}{3}\pi abc \tag{5.2}$$

where the a and c are given by the radius of the chamber and b was given half the height of the chamber. Using the above equation the approximate volume of a droplet was calculated as 683 pl.

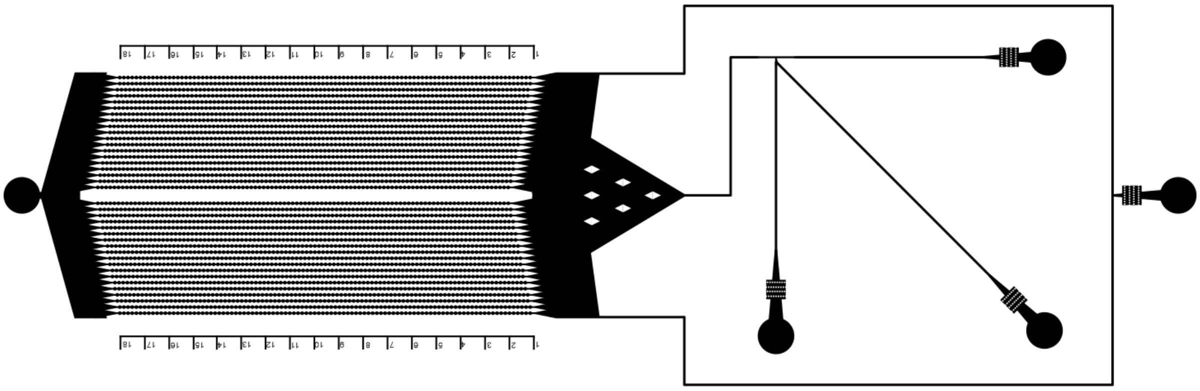

Figure 5.7: A Microfluidic design 3

5.7.2 Operation of the Device

The device was connected to the syringe pumps with tubing (Masterflex® Microbore Transfer Tubing, PTFE, Avantor) through the inlets. Initially the device was filled solely with continuous phase to wet the walls of the tubing. The aqueous syringes were driven at a continuous rate for five minutes to allow equilibration of the pressure in the system. After equilibration the storage chamber was filled with droplets and the tubing severed to begin observation. Initially, the flow parameters had to be determined by experimentation to produce optimally sized droplets that could be reliably trapped within the device. A continuous phase flow rate of 0.14ml/hr and a 0.12ml/hr aqueous flow rate was found to produce optimum droplets for capture. When conducting crystallization experiments it was necessary to use separate syringe pumps for each aqueous inlet with the flows set to total 0.12ml/hr e.g. 0.06 ml/hr and 0.06 ml/hr. Initiating and altering flow was observed to take a period of time to reach a new equilibrium where flow settled. During this settling period some droplets would be formed that were composed of a significant amount more of one aqueous solution than the other. If a droplet would form composed with significantly more of the acidic solution than the basic solution then it had a high probability of crystallizing in the droplet forming junction. Due to the geometry of the device, the traveling time from the junction to the storage matrix would allow a crystal to form, potentially blocking the device or acting as nucleation point for other droplets to crystallize, thus rendering the device useless for further observation and analysis. This was resolved by starting flows at a lower rate with a higher rate of the basic solution than acidic. The flows were then slowly adjusted stepwise to their final rates, maintaining a higher basic flow rate until the last adjustment. This was found to limit the occurrence of early nucleating droplets.

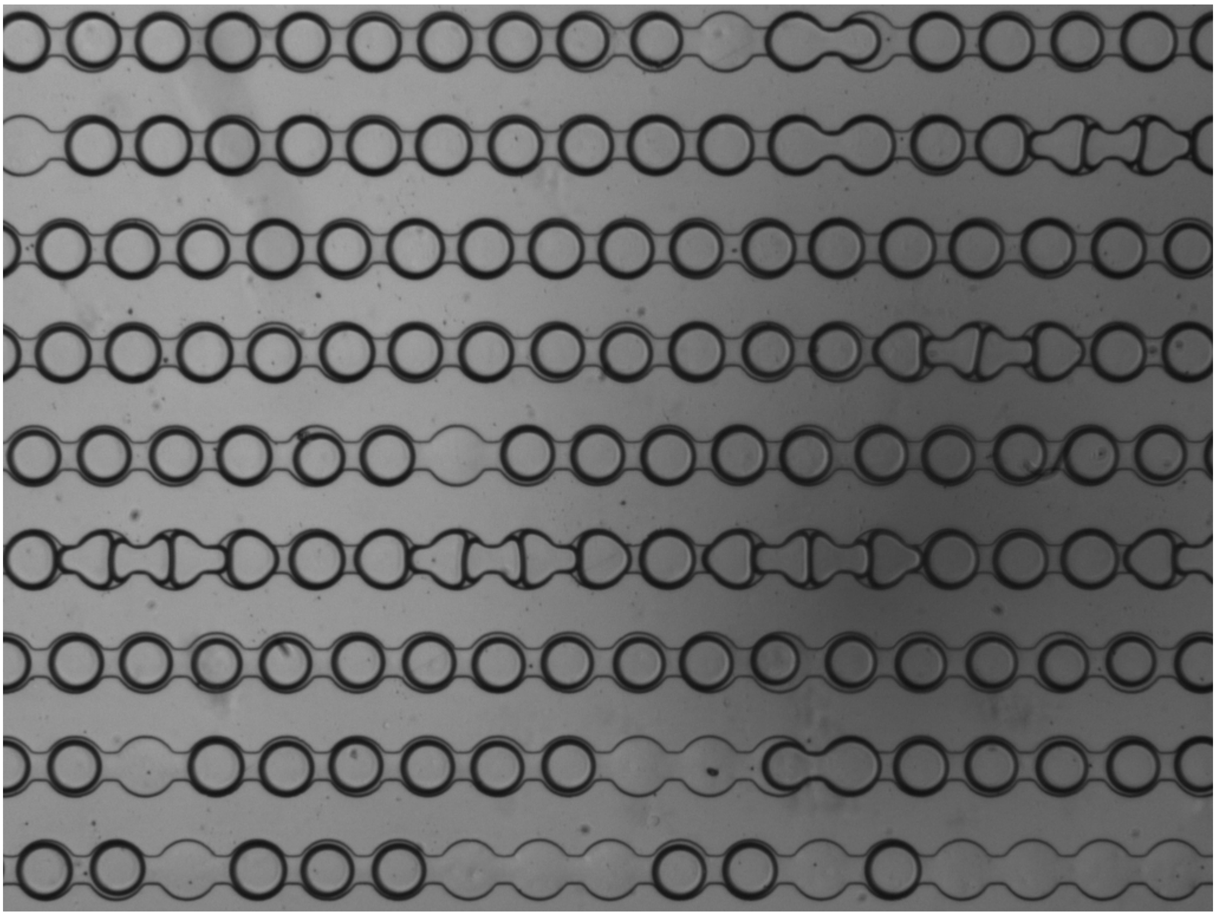

Figure 5.8: Filled "dropspot" device after severing tubing. The observation window of the microscope allowed the tracking of up to 153 droplets. Average filling efficiency was 87% meaning about 130 droplets on average would be filled

5.7.3 Successes and Weaknesses of Device

Droplet storage was observed to be generally effective. after initial disconnecting of the device droplets would settle into traps after a few seconds and, unless the device were sharply moved, would remain in the traps for the duration of the experiment. The average filling efficiency of the device was 87%. Given that the field of view of the microscope allowed for the observation of 153 chambers, this meant that about 130 droplets could be tracked over the course of the experiment.

Two issues were discovered with the device over the course of experiments, both in relation to the large antechamber prior to the storage matrix.

The first was that droplets in the antechamber were allowed to come into contact with each other which allowed them to coalesce. Coalescence in this area occured with a maximum of 5% of droplets that reached the storage matrix. This, while unimportant in non-crystallizing solutions, created a problem when the solution was close to nucleating. Nucleation occurs as a function of the volume of a solution. A droplet with double the volume has double the likelihood of nucleation occuring per second. Therefore, as supersaturation increased there was a higher likelihood of a coalescence leading to a nucleation event. Once a crystal formed in this antechamber, it was likely to get trapped, as the crystal would grow to the height of the channel. This would in turn allow crystals to protrude into other droplets moving around them, encouraging either further coalescence leading to massive droplets and further crystal growth or initiating secondary nucleation in other droplets. This could easily result in a cascade of crystallization, with the entire antechamber filled with crystals in a matter of seconds (Figure 5.9). Once nucleation on this scale occured, the device was rendered useless as there was no way to clean the device.

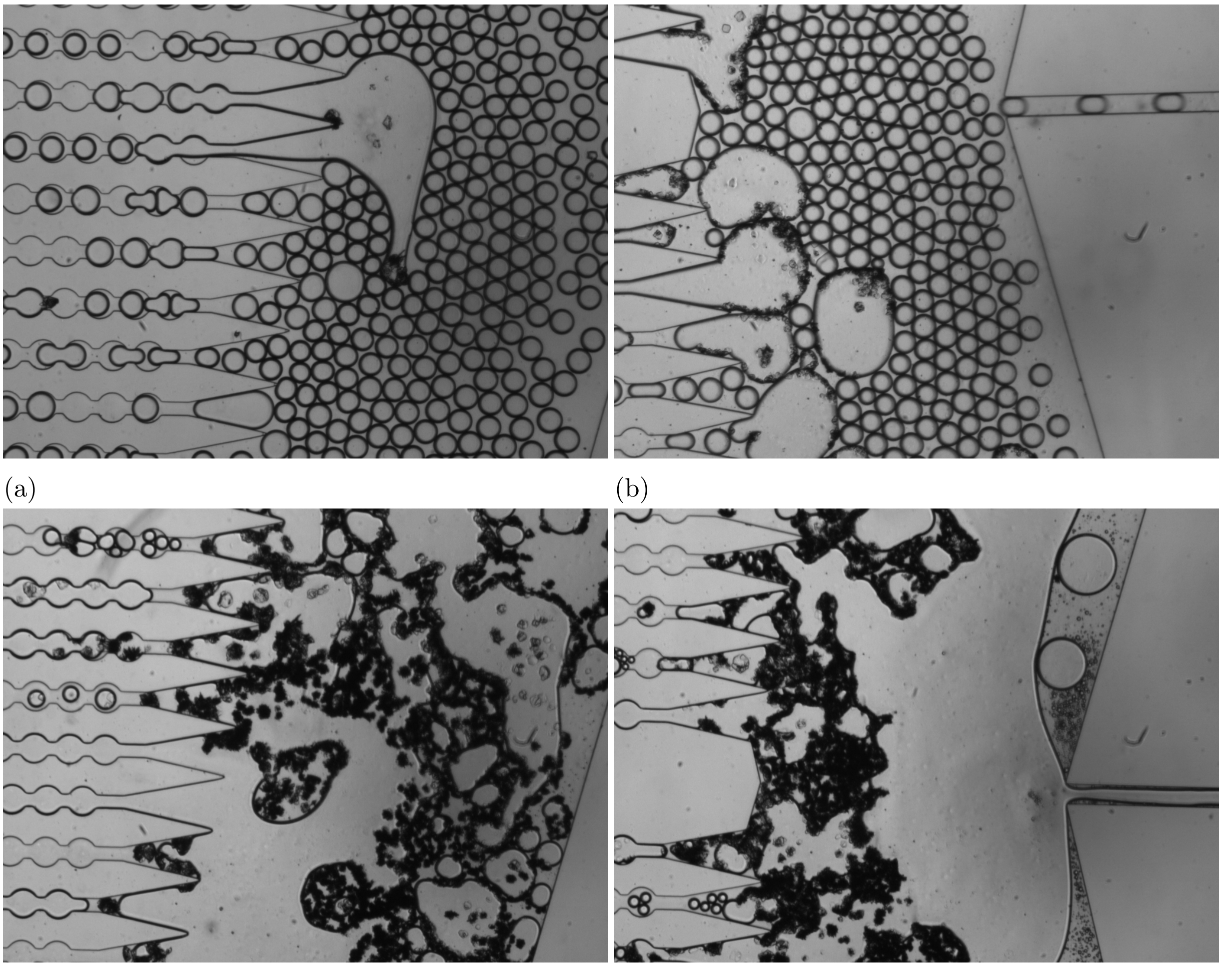

(a) (b) (c) (d)

Figure 5.9: (a) An initial coalescence event spreads as crystals protrude into nearby droplets inviting further coalescence. (b) Crystals that are formed either hold the super droplet in position blocking the channels or flow down into the channels of the storage matrix blocking the constrictions. (c) Rapid secondary nucleation stemmed from a few individual coalescence events. (d) A cascade event would eventually block the entire device, rendering it useless.

The second issue was an uneven rate of droplet transport across the different storage matrix channels. Channels closer to the centre generally flowed slower than those at the outside of the matrix. The general spread of transport rates is thought to be a result of excess continuous phase in the system. The flow rate for the continuous phase was required to exceed the flow rate of the aqueous in order to produce droplets of optimal size. However, each channel of the storage matrix had room for a significant number of droplets but far less space for oil (Figure

5.10). The continuous phase, which is still being pumped in and needs to go somewhere. The result was that the central channels, which were filled with droplets first, would become high resistance channels and the flow would be directed to the outside. The excess continuous phase was unable to pass through the high resistance central channels and so flowed at a very high rate to peripheral channels carrying some droplets through with them at a much faster flow rate. In general, this led to a gradient of transport rates across the channels from center to periphery. In addition to this, however, their was an apparent degree of variability in pressures across the channels. Some channels ceased to flow, perhaps because they were well filled with droplets, creating higher resistance and thus they were being effectively bypassed by the fast-flowing, low resistance peripheral channels. Various droplets of different sizes could have further exacerbated this problem. Cumulatively, these phenomena led to a complex, inconsistent system, such that some channels would flow adequately, others too slowly and some channels would completely block up. This was problematic for this device due to the necessary adjustment period required to initiate flow. If one channel was flowing too slowly or not at all then there was no guarantee that the droplets in that channel were representative of the droplets being generated at the junction. Alternatively, even if the droplets in a stationary channel were of the right composition, the droplets contained in that channel would have been formed earlier than droplets in faster flowing channels. It is essential for induction time measurements to provide an accurate indication of nucleation rate that the time at which crystallizing conditions is reached is known. Therefore if different droplets have different, unknown T_0 values then calculation of induction time is not possible.

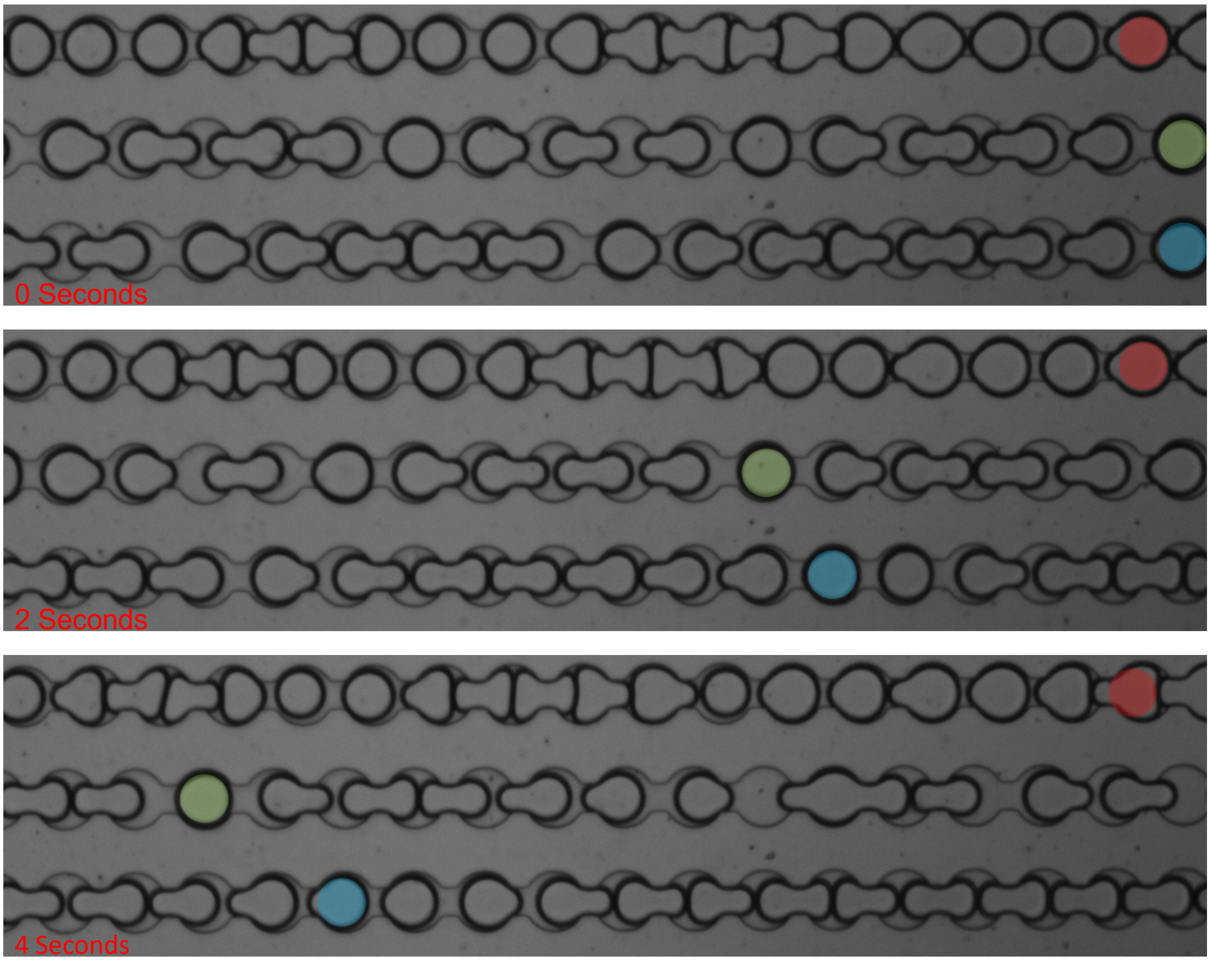

Figure 5.10: Droplet transport across the device is uneven with some channels moving significantly slower than others. The red highlighted droplet channel is flowing markedly slower than the others. The green channel is flowing at a rate of 2.6 droplets/second. The red channel is flowing at 0.1 droplets/second. The blue channel flowed initially at 2.5 droplets/second. However, during the 1 minute these channels were recorded the blue channel stopped flowing completely for the last 40 seconds of the footage meaning the actual flow rate over the observed period was 0.7 droplets/second.

In spite of the flaws identified with the dropspot device, it was still possible to conduct some basic crystallization experiments to identify the upper limit of metastability in this device under these conditions. These results are outlined in the following chapter (Section 6.4.1).

5.8 Device 4 - A Serpentine Storage Device

5.8.1 Design of the Device

The fourth device, was an adaptation of the "dropspot" device, the key feature being to remove the storage matrix and antechamber and replace it with a single serpentine containing chambers of the same dimensions as the "dropspot" device. This had the benefits of the droplet forming junction, found to be adequate and the trapping effects of the dropspot. A single channel ensured that there was no issue of variable flow rates and without the problematic antechamber allowing droplets to coalesce en masse, there was a reduced risk of early nucleation. The device was designed with two possible outlets, the theory being that the resistance of the channels could be varied by selecting which outlet to punch during fabrication. The device was significantly smaller than the dropspot device and it was possible to easily make 15 devices on a single wafer, therefore, both a 150 μm and a 230 μm version of the device was designed. The hope was that if the device were successful, nucleation rates could be compared at two distinct volumes under same conditions. Another minor alteration made to the device was to ensure that the inlet channels leading to the droplet forming juction were of identical length. Hydraulic resistance being a function of channel length (Equation 5.1), and resistance having an effect on flow rate (Equation 2.22), this was done to further guarantee that the acid and basic aqueous flow rates were correct.

5.8.2 Operation of the Device

The device was secured under the microscope using a universal microscope slide holder. Experiments were conducted as before, where the device was connected with tubing to syringe pumps. The device was filled with continuous phase before aqueous flows were started. Aqueous flows

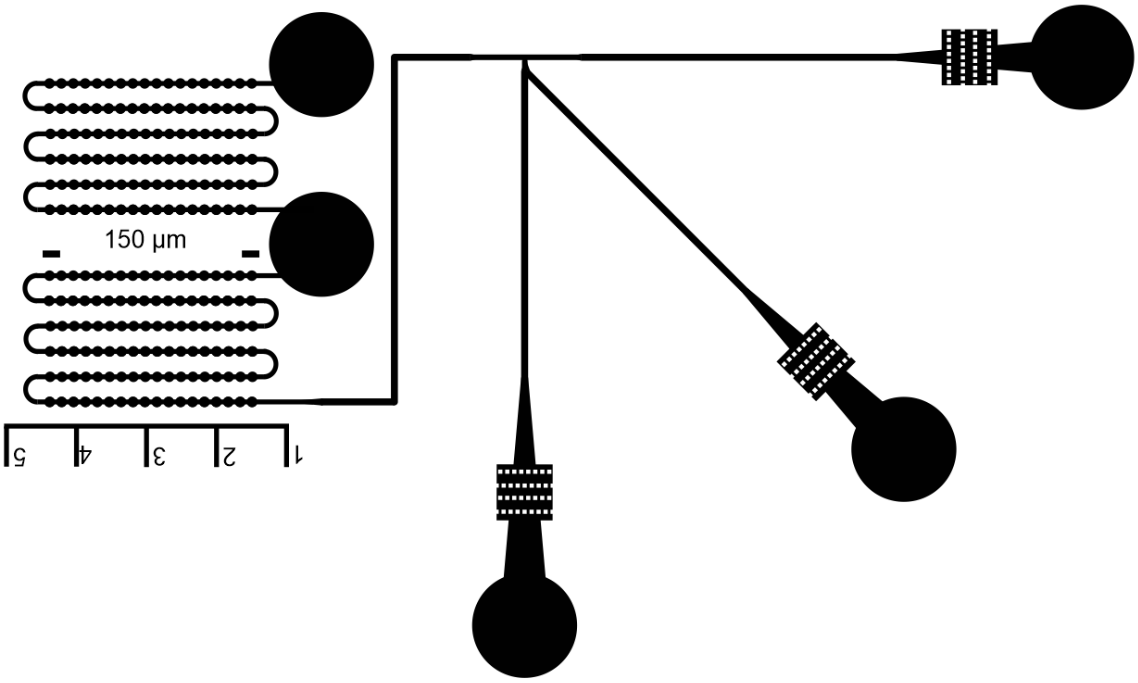

Figure 5.11: A Microfluidic design 4

were initiated at 50% of final flow rate and gradually increased to desired values with priority given to the basic solution so as to prevent premature nucleation. When droplets were successfully stored in the serpetine, the tubes were simultaneously severed and the pumps switched off. Immediately, recording of microscope images began with the field of view covering the serpentine.

5.8.3 Successes and Weaknesses of Device

The device was still able to consistently generate droplets of the right size with apparently correct ratio of basic and acidic solutions. The device was significantly less prone to nucleation cascade events due to the limited contact between droplets. One weakness of the device was that the fluid flow ratio of continuous to aqueous required to produce the correct droplet size led to a big gap between droplets when stored in the device As a result, the droplet trapping efficiency was between 40 - 45 %, significantly lower than desired. This limits the statistical accuracy of the probability distribution fitting. The minimum number of droplets for optimum fitting would be 80 per condition. This would require that experiments either be repeated to get statistically significant number of induction time experiments for analysis or use an alternative analysis method such as maximum likelihood estimation [26].

An alternative design was hypothesized for extracting the excess oil after droplet formation. Such a design would include vents between the droplet forming junction and the storage serpentine connected to an outlet. The vent geometry would be such that droplets would be unable to pass through but oil would and the length of tubing connected to the outlet could be used to control the resistance and therefore, the flow through that outlet, tailoring the amount of continuous phase extracted through the vent so that droplets would be closer together, getting a higher fill rate of the storage serpentine but not so close that coalescence would become a problem.

An intermediate solution was devised to extract some oil and give a marginal improvement to droplet storage. The devices were punched fully at the second outlet prior to bonding. After bonding, a biopsy punch was used to excise a section of PDMS above the first potential outlet, leaving a thin layer of PDMS. This thin layer was then pierced several times with a fine gauge needle and tubing was connected to the new partial outlet. Due to the small gauge needle and the elasticity of the PDMS, the perforations created were large enough to allow a fraction of oil to escape the channel but small enough that droplets were unable to escape. This was found to marginally improve the trapping efficiency to 45-50%. However, it introduced problems with droplets occasionally attaching to the perforations and not flowing through the channel, therefore, the idea was abandoned.

The key manner in which this device superseded previous designs was its ability to store droplets in a manner that allowed for the monitoring of crystal nucleation. However, the reduced geometric area of this device led to an increased surface to volume ratio between the device and the surrounding air, resulting in an increased rate of water pervaporation to the atmosphere. This could be improved by incorporating a stabilising solution of equivalent osmolality either around the device or within a hydrating chamber or channel such as was included in device 2. This volume effect has a key impact on the collection of data which is discussed below.

5.9 Discussion

The data extracted from the collected images relies on a number of assumptions.

5.9.1 Mixing

The water in oil droplets are collected from a mixture of two solutions flowing at pre-determined flow rates. The composition of the final solution is dependent on those flow rates, for example, equal flow rates indicates a final solution made up of 50% fractions of the input solutions. However, the syringe drivers operate by turning a screw which depresses the plunger. At the extremely low flow rates used the screw operates intermittently, turning a minimal amount then stopping. This occurs at a rate of approximately 5Hz. This intermittency creates the potential for different flow rates in each solution if one pump is activated while the other is stopped. A droplet formed under such conditions might not have an exactly 50:50 ratio of solutions and this would have potentially major effects on the nucleation process occuring downstream. The quality of mixing could be analysed using fluorescent solutions to determine the composition of final droplets, however, this was not not feasible due to limitations in time and budget. Consequently, it was assumed that the mixing was consistent. As mentioned previously, this

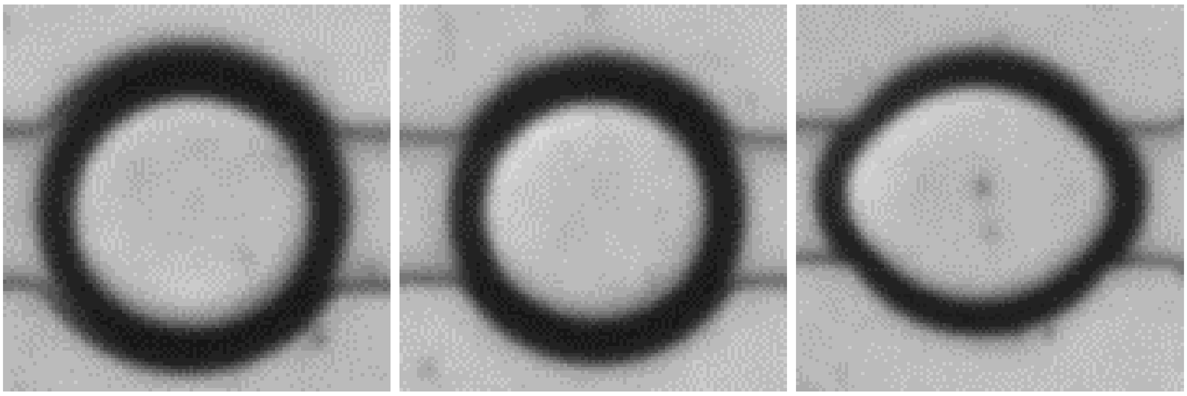

(a) Possible Ellipsoid (b) Either Ellipsoid or Plug (c) Definite Plug

assumption is somewhat supported by the bisection of the area of the static mixing Y-junction.

5.9.2 Droplet Geometry

Microscope images collected capture a two dimensional representation of a three dimensional object. Knowing the volume is determined by knowing the 3D shape. However, it is challenging to definitively determine what the 3D shape is and as such, an assumption has to be made. For example, a droplet that is smaller in 2D area than the trap it resides in is likely to be best described by an ellipsoid (Figure 5.12a) and its volume can be defined by

$$V = \frac{4}{3} \times \pi \times abc \tag{5.3}$$

where a and b are the radius of the droplet and c is half the height of the channel. However, a droplet where the perimeter of the 2D area is completely in contact with the walls of the chamber (Figure 5.12b) could have the volume of an ellipsoid or it could be something closer to a cylinder where the droplet is a partially deformed ellipsoid. Finally, a droplet that is extended beyond the bounds of its trapping chamber (Figure 5.12c) is certainly a plug where the volume is approximately the 2D area of the shape multiplied by the depth of the channel.

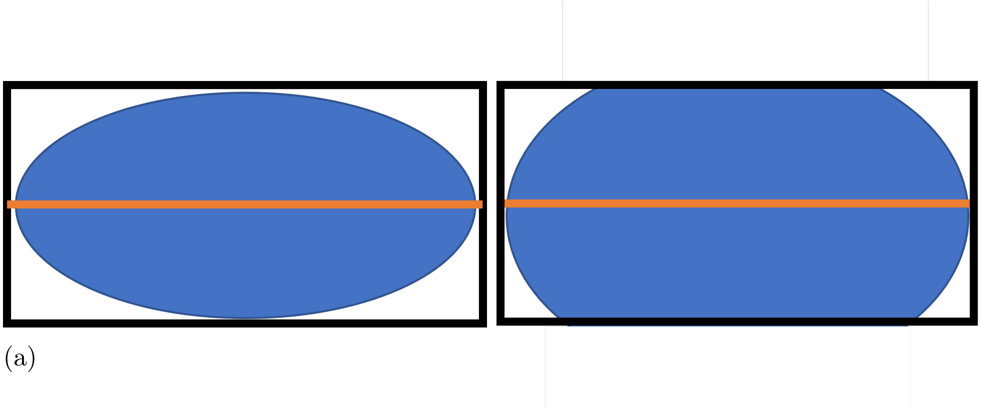

(a)

(b)

Figure 5.13: Cross section of potential ellipsoid droplets. (b) has greater volume than (a) but identical observed 2D area represented by orange line.

There is further uncertainty in the transition from plug to ellipsoid. As time passes and water pervaporates from the droplet, a droplet will lose volume. A droplet simililar to 5.12b will potentially decrease in 2D area proportionately to the volume, it alternatively might maintain its 2D area while losing volume. For example, The droplet in figure 5.13b is greater volume than 5.13a but the area as viewed from above (represented by the orange line) remains the same. This makes accurate calculation of volume an impossibility. Therefore, it was decided to use the 2D area multiplied by the depth for droplets that appeared to exceed the trap chamber (as an ellipsoid estimate for such a droplet would be obviously incorrect). Droplets that contacted the edges of the trap chamber were volumetrically defined as a range between the ellipsoid volume and the cylindrical volume. Droplets that appeared to be smaller than the trap were calculated using the volume of an ellipsoid, although this is an approximation.

5.9.3 Droplet Volume

Droplet size was used to calculate the volume of the droplets in each experiment recorded as sufficient nucleation according to the assumptions stated above. The volume of each droplet at

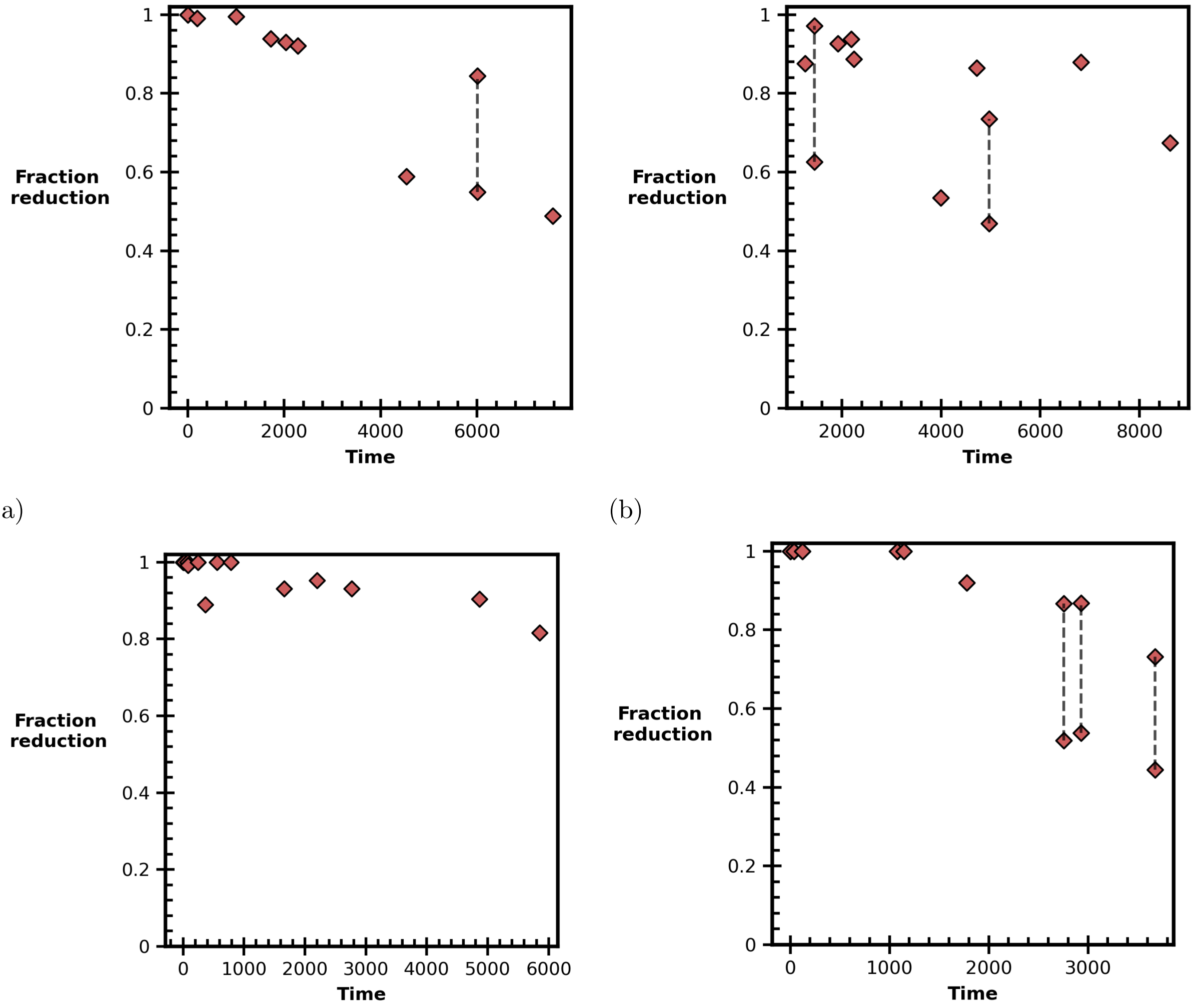

(a) (b)

(c) (d)

Figure 5.14: The recorded droplet volume reduction at the time of induction for each droplet as a fraction of the initial droplet volume. If the droplet volume was ever calculated as a range this is represented by two points at that induction time connected by a dashed line.

both t0 and induction time was determined using Python software which can analyse an image to isolate each droplet from its surrounding image. The software then calculates the 2D area of represented by the droplet and calculates both the plug and ellipsoid volumes. Each droplet image was then visually appraised to determine if it should be classed as an ellipsoid, a plug or a range between the two.

Figure 5.14 displays the fraction of volume reduction for each droplet in each experiment. If a droplet was found to be fully in contact of the walls of the trap at either the start of the experiment or at the induction time the volume fraction reduced is reported as a range. The apparent rate of droplet shrinkage is variable between experiments and droplets with experiment 5.14c showing the least decline in volume. The variability in average droplet size for each experiment is a significant factor. Smaller droplets will, theoretically, have a lower rate of volume loss due to decreased surface area. Smaller droplets will also have less surface in contact with the PDMS walls of the device. Table 5.2 shows the average rate of loss for each experiment over time. While this rate would not be applicable to any long term experiments, it shows that the smallest droplet volume clearly had the lowest amount of volume loss.

In addition, the droplet's location within the device may affect the rate of water pervaporation, with droplets towards the interior possibly being less susceptible than those at the periphery. This was observed more clearly in earlier experiments with previous devices but has not been quantified here.

Experiment	Average Initial volume [pl]	Rate of loss [% /1000s]
1	1358	6.27
2	1103	4.52
3	373	2.68
4	1010	9.99

Table 5.2: Rate of loss from initial droplet size for each experiment

The effect of droplet volume loss on droplet composition is significant. Figure 5.15 shows the extent of maximum possible supersaturation and pH deviation. The volume change affects a change in pH and concentration, thereby leading to a complex set of changes in supersaturation ratio. While this is large range of possible supersaturation values it should be noted that values at the extremities of the range are uncommon, shown by the mean values for pH and supersaturation ratio being close to the initial value.

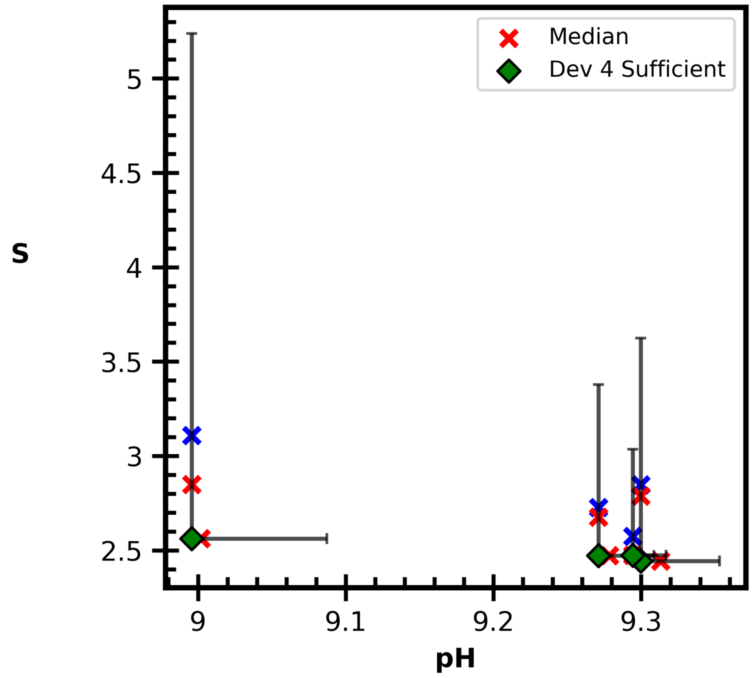

Figure 5.15: Nucleation rates with range of possible values for S and pH due to water loss. Mean and median values are included to show that outliers are common.

The incorporation of PDMS hydrating element to the experimental set up would reduce the rate of droplet shrinkage, allowing for longer experiments and more refined control of the solution composition.

5.10 Conclusions

The aim of this work was to develop a microfluidic device that could be used for the collection of induction times under isothermal conditions for the calculation of crystal nucleation rates.

The device presented in this work utilizes the pH-dependence of the solubility of the model compound to generate supersaturation through the mixing of a high pH solution with a strong acid. The droplets formed on the device can be observed for nucleation events for up to 10000 seconds. The limitations of the device were the variability in droplet volume, the volume depletion by pervaporation of solvent through PDMS, the lack of temperature control and the inability to collect more than 50 droplets in the observation window.

Chapter 6

The Study of pH-Shift Crystal Nucleation Kinetics Using Novel Microfluidic Devices

6.1 Introduction

Nucleation is a key step in the crystallization process which controls many crystal product quality attributes such as particle size distribution and polymorphism[1, 10, 22]. Nucleation is the creation of a new, crystalline solid phase from a mother liquor of solution. Reliable and quick mechanisms for analysing nucleation and measuring nucleation rate are of great importance for the validation of scientific theories and the development of crystallization processes.

pH-shift crystallization is a less studied area of crystallization, in particular, with regard to nucleation studies. pH-shift crystallization relies on the appreciable difference in solubility between the protonated and deprotonated molecule to generate supersaturation. While there is work reporting on metastable zone width in a pH-shift system [7], there is, as yet, no work reporting on nucleation rate determination in such a system.

Microfluidics has been presented as a useful tool in the study of nucleation. The low volumes and laminar flow of microfluidic devices offer tight control of crystallization conditions [8][64]. The microscale dimensions of a microfluidic device allow for enhanced observation and tracking of individual nucleation events using high quality microscopic images providing a high-resolution platform for nucleation studies. Microfluidics allow for the generation of supersaturation in pH shift crystallization through well-controlled mixing under isothermal conditions.

6.2 Aims and Objectives

This work aims to collect nucleation rate data from the novel microfluidic device presented in chapter 5 and compare this with the microvial nucleation rate data collected in chapter 4. First, the metastable zone must be determined for this device for immediate comparison to previous work. Then, induction time data must be collected using the novel device, utilizing pH-shift crystallization under isothermal conditions to generate supersaturation. The collected induction time data must be then appropriately analysed to determine the nucleation rate. Finally, a comparison will be made between the nucleation rate data collected in the microvial set up in chapter 4 and the novel microfluidic device.

6.3 Materials and Methods

6.3.1 Materials

DL-phenylalanine (DL-phe; Sigma-Aldrich,$\geq$ 99%) was used as purchased. Sodium Hydroxide (anhydrous, Sigma-Aldrich, $\geq$98%) was used as purchased. Hydrochloric acid solution 37% HCl (ACS, Sigma-Aldrich, reagent) was used as purchased. Fluorinet FC-40 oil (Sigma-Aldrich) was used as purchased. #008 Fluorosurfactant (Ran Biotechnologies, Beverly, MA, USA) was used as purchased. Polydimethylsiloxane (PDMS, Sylgard 184, Dow, MI, United States) was used as purchased. Curing Agent (Sylgard 184 Curing agent, Dow, MI, United States) was used as purchased. Methanol (VWR, Lutterworth, UK) was used as purchased. Isopropanol (VWR, Lutterworth, UK) was used as purchased. Acetone (VWR, Lutterworth, UK) was used as purchased. 1H, 1H, 2H, 2H-perfluorooctyl-trichlorosilane (Silanizing agent, Sigma Aldrich, UK) was used as purchased. SU8 3035 photoresist (MicroChem, Newton, MA, United States) was used as purchased.

Solvents

Preparation of Aqueous Sodium Hydroxide (NaOH) Solutions Aqueous solutions of NaOH were meticulously prepared by dissolving a precise quantity of pure NaOH pellets in approximately 70 mL of distilled water within a volumetric flask. Subsequently, distilled water was cautiously added to the flask until the solution reached the volume line, ensuring a final volume of 100 mL, thereby producing a solution with a predetermined concentration. To achieve thorough mixing, the volumetric flask was inverted multiple times.

Preparation of Aqueous Hydrochloric Acid (HCl) Solutions Aqueous solutions of HCl were prepared by carefully mixing a precise mass of 37% HCl solution in approximately 70 mL of distilled water within a volumetric flask. Additional distilled water was gradually added to the flask until the solution reached the prescribed volume, indicating 100 mL of solution and resulting in a solution with a predetermined concentration. The volumetric flask was inverted multiple times to achieve effective mixing of the HCl solution.

6.3.2 Solution Composition and Supersaturation

Supersaturation ratio was the key target for selecting solution composition. Solutions were mixed in a 1:1 ratio within the microfluidic device. As a result, the solution composition of the high pH solution and the low pH solution had to be determined prior to experiments to achieve the desired supersaturation ratio. The compositions were calculated using the model described in chapter 3.

In Chapter 4 we reported nucleation rates for DL-phenylalanine in the range 50 - 1750 particles/m^3·second. These experiments were conducted under precise isothermal control at 1 ml and were agitated. Agitation has a significant effect in promoting nucleation. The microfluidic experiments will not be agitated and will be conducted at volumes orders of magnitude lower that the experiments in the previous chapter. Threrefore, the expectation was that nucleation will require significantly higher supersaturations. In fact, due to the volume effect in particular, the nucleation rate required to produce nucleation in the timescales required will be in the millions of particles/m^3·second.

6.3.3 Crystallization Experimental Protocol

Solutions of DL-Phenylalanine in Sodium Hydroxide and Hydrochloric acid of known concentration were made up. Continuous phase was made up using FC-40 oil and 2% fluorosurfactant. Glass 250μl syringes were connected to Masterflex Microbore Transfer Tubing (PTFE, VWR

MFLX06417-21) using single use, hypodermic needles. Solutions and oil were drawn up into syringes with care taken to exclude any air. The syringes were attached to individual syringe drivers (Aladdin Single-Syringe Pump, High Pressure, World Precision Instruments, FL, USA). The tubing was then connected to the inlet ports on the device. Exhaust tubing was attached to the device. The device was placed in a Zeiss Axiovert 5 microscope (Zeiss, Cambridge, UK) and observation was conducted through a Labview controlled Dalsa Genie CMOS HM1024 camera (Phase 1 Technology Corp, NY, USA). The syringe drivers were started at half of their desired final flow rate, beginning with the oil syringe to wet the walls of the device with oil. The flow rates were gradually increased to the desired level with priority given to the basic flow to prevent early nucleation. When the right flow rates were reached the flows were given five minutes to equilibrate. After this, the tubing was severed with a pair of sharp shears.

6.3.4 Observation

A micro-batch crystallization approach was taken in order to allow the acute observation of multiple crystallizing reactors simultaneously. The probability distribution based approach for quantifying nucleation rate requires that at least 80 induction time measurements be collected for a statistically significant nucleation rate to be obtained. Therefore, a key design specification was that the device would allow the formation of microfluidic droplets to be stored in a stable, observable location. The statistical approach used requires that crystallization experiments have the same relative supersaturation and volume. Therefore, it was deemed optimal that the microfluidic device meet this need.

6.4 Results

The primary objective of the work was to collect nucleation rate data within the microfluidic device to analyse and compare with the data collected in the Crystal16. The device utilized a static mixing Y-junction to introduce high pH, high concentration solution to low pH precipitant. The resulting solution was of a supersaturation pre-determined with the use of the MATLAB model outlined in chapter 3. The solution was emulsified into water in oil droplets using a T-junction and captured in a storage serpentine, where they were observed for 10,000 seconds using an inverted microscope. Images were collected every second. The image data was analysed and produced induction time data, growth data, and droplet size data.

6.4.1 Device 3 Metastable Zone

Despite the discovered flaws with the device, it was still possible to gather some valuable crystallization data. The initial objective was to identify a region of supersaturation ratios where nucleation would occur within a 10000 second window. This time window was selected as it was sufficient to measure nucleation but not so long that water pervaporation would affect crystallization to a significant degree. Over the time period the droplets would lose, on average, 8 μm in diameter, meaning a 10% decrease in volume over the time period. This was not insignificant and had to be incorporated into nucleation rate calculations. Experiments were conducted within the pH range 9.0 - 9.4. Microfluidic droplets were expected to be much less prone to primary nucleation than the 1 ml vials used in Chapter 4 due to overall rate of nucleation (JV) being a function of the solution volume. Therefore experiments began at $S = 1.2$ and subsequently, S values were rapidly increased.

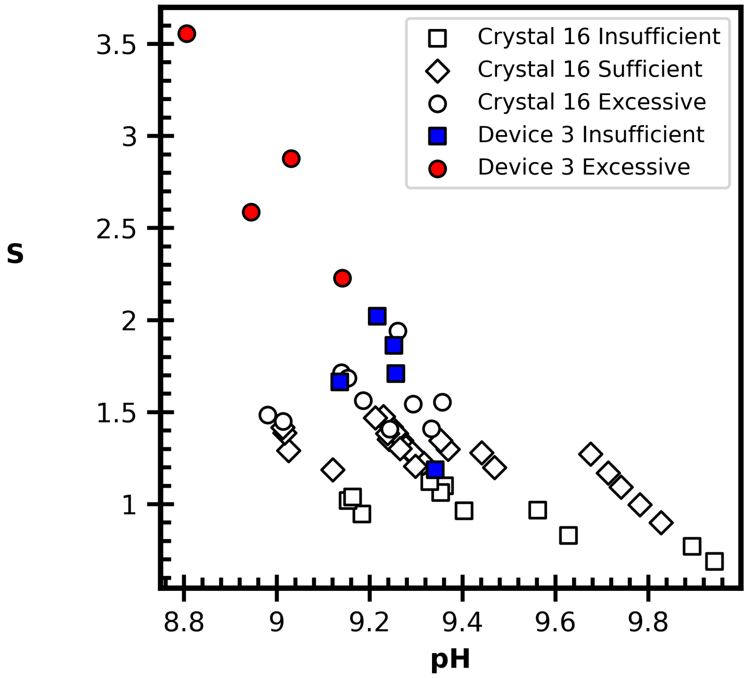

Figure 6.1: Experiments conducted at 600 pl in the "dropspot" device shown by squares compared to Crystal16 1 ml experiments.

Nucleation was neglibible in the experimental time frame at supersaturations below S = 2 with the lowest supersaturation tested at 1.2. Some experiments did not nucleate at all and of those that did, none produced more than 2 nucleation observations out of approximately 130 droplets (Table 6.1). This provided insufficient observations to determine nucleation rate by fitting. Supersaturation was increased to attempt to find a range where nucleation was optimal. The threshold of sufficient nucleation was conditions in which at least 10 nucleations were observed, as with chapter 4. The goal was that droplets would be stored in the matrix and then would nucleate over the observation period. However, there appeared to be a supersaturation threshold below which nucleation would not happen and above which a nucleation cascade (described in Figure 5.9) would occur in the matrix antechamber and would block up the device before droplets could be stored. This cascade phenomenon was observed in experiments with identical conditions to those reported as insufficient. It was found that at supersaturations close to 2.1 the nucleation cascade would sometimes occur. This was initially believed to be a flaw with experimental protocol, however, further observation suggests that these events were primarily a result of coalescence in the matrix antechamber. Therefore, the results reported here as insufficient are conditions under which it was sometimes possible to store droplets successfully in the storage matrix but also did not nucleate in the matrix over the 10000 second observation window. For supersaturations greater than 2.2, a cascade would always occur in the matrix antechamber over 3 repeats of these conditions (Table 6.2. Such events were defined as excessive nucleation. However, as there were no conditions under which nucleation was found to be sufficient it was necessary to develop a new device that resolved the problems created by the matrix antechamber in order to find a region where optimal nucleation could be observed. In addition, it was necessary to resolve the problem of uneven droplet transport.

pH	Concentration [M]	Supersaturation	Percentage Nucleated
9.34	0.31	1.18	0
9.13	0.37	1.66	0
9.26	0.37	1.71	0
9.21	0.4	1.86	1.5
9.22	0.42	2.02	1.5

Table 6.1: Solution parameters for microfluidic nucleation rate experiments using Device 3 where nucleation was insufficient to calculate nucleation rate data.

It is worth noting at this point that even under these flawed microfluidic conditions droplets were found to be much more stable under microfluidic conditions than in the Crystal16 with less than 2% of droplets nucleating in 4 hours at S = 2.02, while in the Crystal16 at much lower supersaturations, nucleation was occurring before reaching the isothermal point. The metastable limit, therefore, in this device under these conditions is approximately a supersaturation ratio of 2.0 - 2.2.

pH	Concentration [M]	Supersaturation
9.14	0.42	2.22
8.94	0.42	2.58
9.03	0.47	2.88
8.81	0.47	3.56

Table 6.2: Solution parameters for microfluidic nucleation rate experiments using Device 3 where nucleation was excessive and there was no opportunity to observe droplets in device.

6.4.2 Device 4 Metastable Zone

Data was collected using the fourth device with the objective of analysing the metastable zone in this system under the conditions of a microfluidic device with droplet volumes around 0.5-1 nl. As in chapter 4 nucleation was categorized as insufficient, sufficient and excessive, however, the boundary conditions for each had to be adjusted due to the nature of nucleation in the microfluidic device. Experiments resulted in a few different possible outcomes. The first outcome, which occurred at lower supersaturations, was less than 10 nucleation events occurring in the observation window, classed as insufficient. To ensure the validity and reliability of the analysis, it was deemed appropriate to set a lower limit of 10 data points for fitting the nucleation rate. Excessive nucleation was noted where nucleation occurred instantaneously in all droplets. For an experiment to be classed as sufficient there had to be sufficient non-nucleated droplets at the start of the observation window to observe at least 10 nucleations and at least 10 droplets had to nucleate during the observation window. This phenomenon was uniquely observed in this device as earlier devices either failed to nucleate or nucleate excessively in the cascade phenomenon described above.

While in chapter 4 a single vial which nucleated prior to the observation window was regarded as excessive, this was due to the nature of isothermal crystallization achieved by cooling. A vial that nucleated in this way would have nucleated prior to observation would have nucleated at a temperature different to the defined isothermal conditions and therefore, at a different solubility and supersaturation. In the microfluidic device this was not the case. The desired supersaturation was achieved at the moment of mixing (working with the assumption that mixing is essentially an instantaneous process at the induction timescale considered here). The limitation to observation was the time that it took to transfer a droplet from the mixing junction to the storage matrix where observation occurred. In addition, the action of stopping droplet generation by cutting off flow to the device had the effect of moving the device out of the field of view of the microscope. Reacquiring the storage matrix with the microscope also added time between achieving supersaturation and the beginning of recording nucleations. Therefore, a droplet that is classified below as instantaneous nucleation occured under the desired conditions, but during the approximately ten second window under which observation of nucleation was not possible.

Experiments conducted in device 3 reached a maximum supersaturation of 2.02 without significant nucleation observations. Between 2.02 and 2.22 there was a sharp transition into excessive nucleation. This was believed to be a fault in the device design as no conditions were found where nucleation could be classed as sufficient. In device 4 there was an increase in the metastable zone limit from 2.02 to 2.44. In fact, conditions between a supersaturation ratio of 2.22 (which always resulted in a nucleation cascade in device 3) and 2.44 were found to be insufficient at producing nucleating droplets, confirming that early nucleation was being precipitated by some flaw in the design of device 3. Between 2.4 and 2.6, sufficient nucleations were observed to attempt fit-

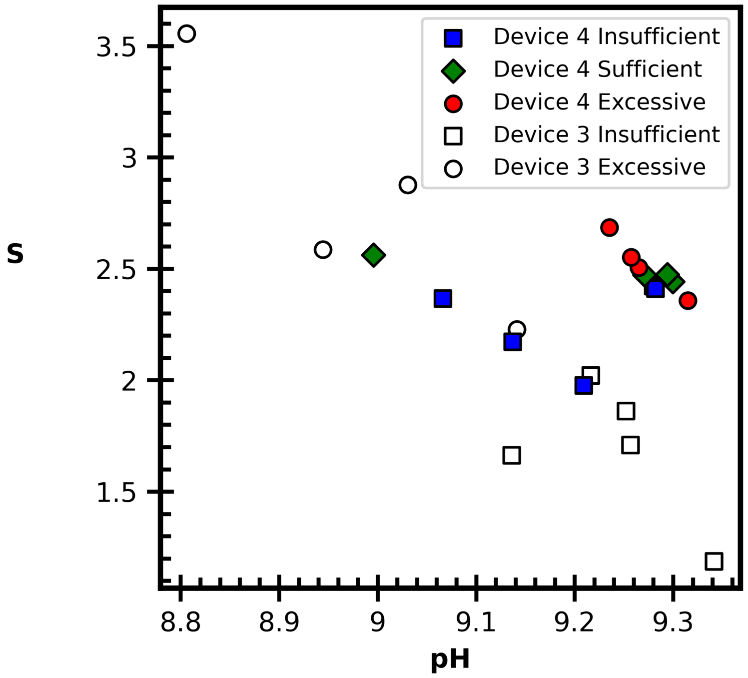

Figure 6.2: Compositional data of all experiments conducted in microfluidic devices. Experiments conducted in the dropspot device (Dev 3) marked by circles. Experiments conducted in the current device (Dev 4) marked as diamonds.

ting. Above 2.56 supersaturation occured instantaneously in all droplets. For each experiment, droplets were categorized as instantaneously nucleating, slowly nucleating and non-nucleating within the experimental time frame.

Supersaturation	Instant	Slow	No Nucleation
2.561	0%	21%	79%
2.442	42%	23%	35%
2.474	48%	28%	24%
2.472	40%	25%	35%

Table 6.3: Percentage of droplets categorized as instantaneously nucleating, slowly nucleating and non-nucleating for each experiment.

As supersaturation increased fewer droplets were recorded as non-nucleating and more droplets were registered as instantaneously nucleating. The fraction of droplets nucleating within the time window gradually increased, however, above 2.56, all experiments showed 100% instantly nucleating (Figure 6.2), indicating a hard upper limit to the metastable zone width in this system.

Within this device it was not possible to collect nucleation data below a supersaturation of 2.4. This could be changed with some adjustments to the device. The use of a solution of equal osmotic pressure to the droplets to hydrate the PDMS would reduce the loss of droplet volume and allow for a longer time window within which it might be possible to observe nucleation at lower supersaturation and collect nucleation rate data.

6.4.3 Nucleation Rate and Fitting

As discussed in chapter 4, it is possible to determine nucleation rate by fitting a series of induction time experiments collected under isothermal conditions to a Poisson distribution. This method assumes that the underlying kinetics remain the same throughout the experiment in all droplets. The microfluidic experiments conducted in this work could be fitted in a similar manner, with each droplet effectively an individual reactor. However, the large number of non-nucleating droplets and the number of droplets that nucleate instantly suggests that nucleation doesn't follow the same behaviour in this system. This may be due to the non-agitated nature of this system. Similar behaviour has been observed in non-agitated systems of glycine, paracetamol and potassium nitrate[75–77].

$$P(t) = 1 - \exp(-Jv(t - t_g)) \tag{6.1}$$

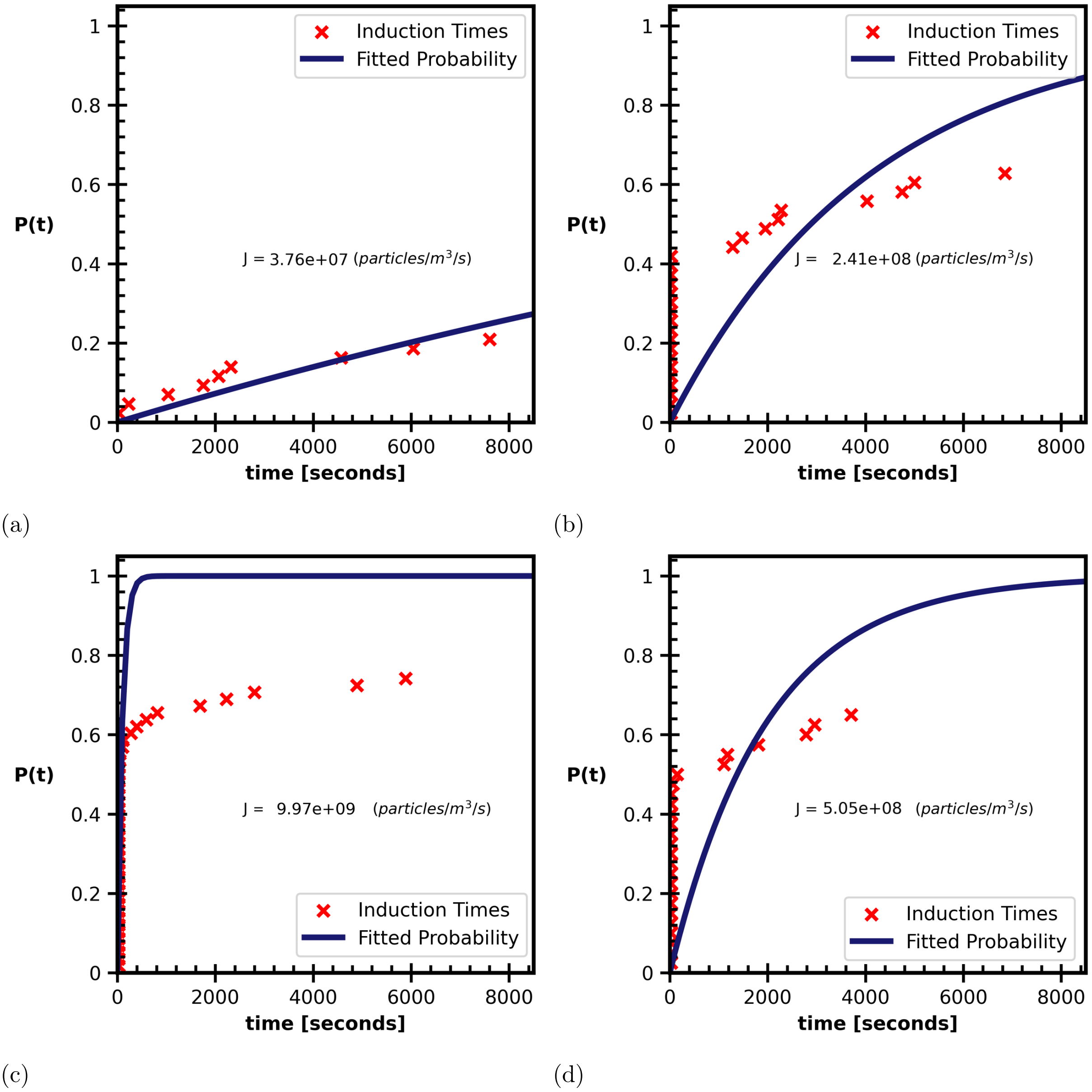

(a) (b) (c) (d)

Figure 6.3: Fitted Poisson distribution for all microfluidic induction time experiments.

The induction times were fitted to the standard Poisson distribution (Equation 6.1) (see Figure 6.3. However, as crystal nucleation is observed almost immediately t_g was set to 0. This provided a poor fit for all experiments with instant nucleations. With the exception of the experiment shown in figure 6.3a the fit is poor as these experiments are dominated by the instant nucleations which seem to be controlled by different kinetics to the slowly nucleating droplets.

In order to obtain a better fit for slowly nucleating regime it was attempted to exclusively fit those nucleations, excluding those experiments that nucleated instantaneously(Figure 6.4). This

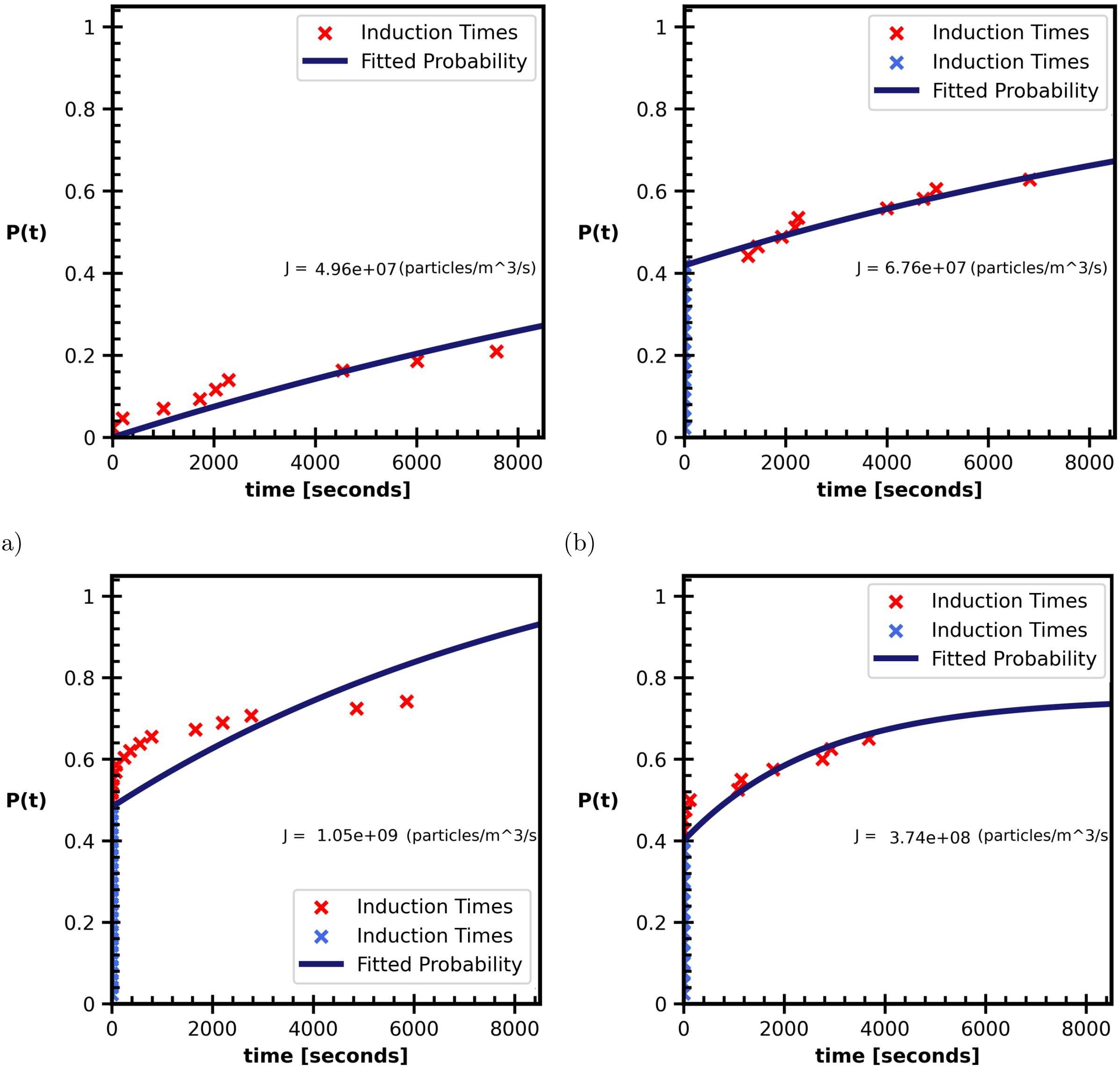

(a) (b) (c) (d)

Figure 6.4: Fitted Poisson distribution with instant nucleations labelled blue and not included in the fitting.

fit used the following equation:

$$P(t) = P(i) + (1 - \exp -Jvt) \tag{6.2}$$

where $P(i)$ is the probability of nucleation being instant. This effectively assumes that the nucleation rate for droplets which nucleated prior to the start of observation was infinite. This fits the slow nucleation data better than the previous fit. For Figures 6.4c & 6.4d the assumed further nucleations are plotted out beyond the the last nucleation, although there are no data available and it is not guaranteed that it would extrapolate in this manner.

The apparent separation between the extremely fast nucleation that occurs prior to observation and the slower nucleation that occurs over the following 10000 seconds suggests a bimodal nucleation regime, similar to that observed by Javid et al[78]. Therefore, the data was fitted as the sum of two weighted, exponential distributions, as shown in equation 6.3:

$$P(t) = A(1 - \exp(-J_1 vt)) + (1 - A)(1 - \exp(-J_2 vt)) \tag{6.3}$$

where A is the fraction of droplets nucleating extremely quickly, J_1 is the nucleation rate of droplets classified as instantaneously nucleating and J_2 is the nucleation rate of droplets classified as slow.

Fitting the double exponential to 6.5 shows good agreement with the data. This type of fitting results in a very high nucleation rate in the first regime (J_1) and a lower value for the second regime (J_2). The quality of fitting with two exponential terms suggests that nucleations in these systems are governed by two different mechanisms. This conforms with what others have reported in non-agitated systems [75, 78–81] However, the cause of these two mechanisms remains unexplained.

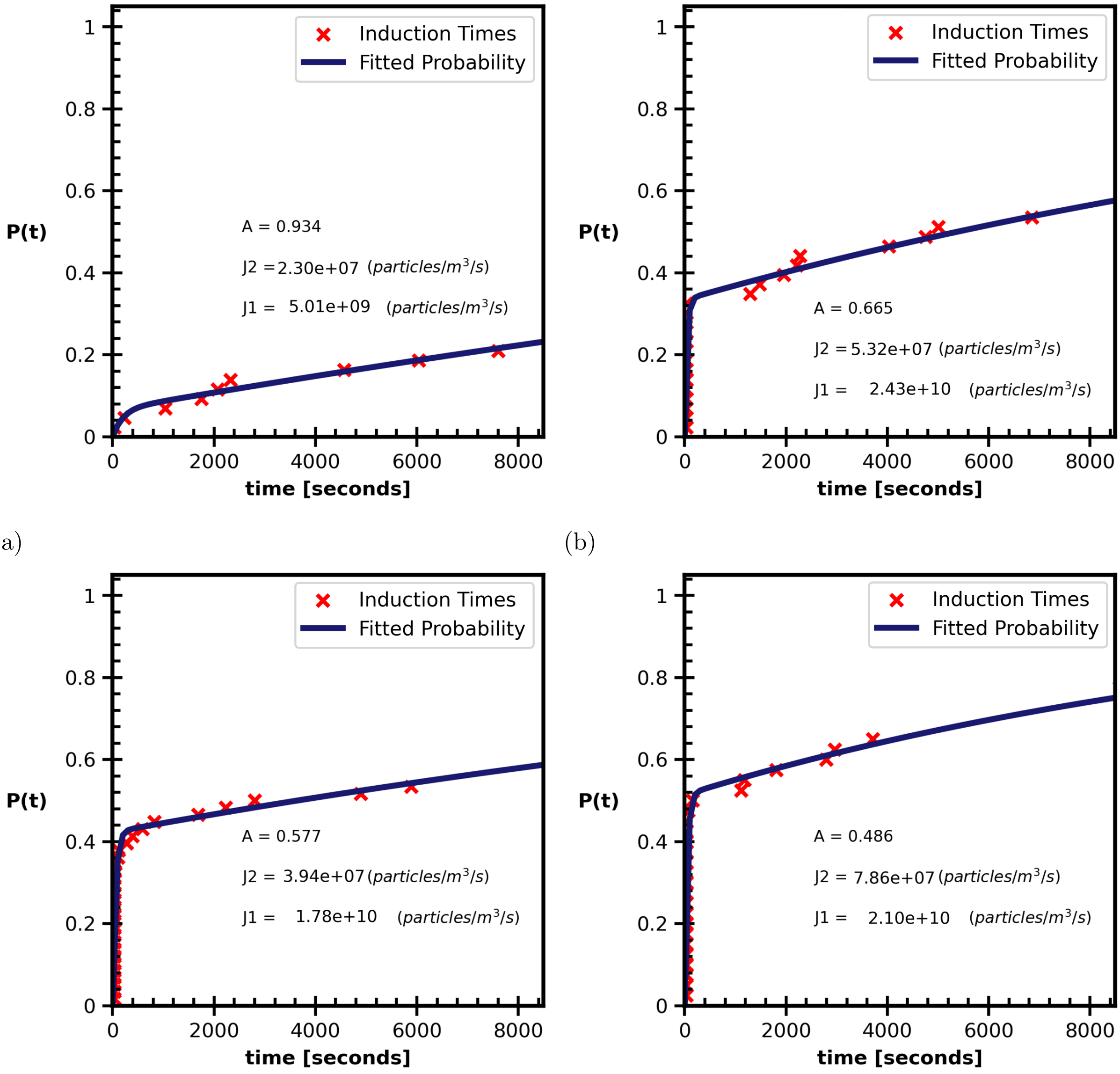

(a) (b)

(c) (d)

Figure 6.5: Bimodal fitting performed on nucleation induction time data from microfluidic experiments.

One potential explanation for the phenomenon of near instantaneous (very fast) nucleations is that during the brief transition period from the droplet forming junction to the storage matrix, the droplets experience a small but significant degree of fluid shear due to the laminar flow of the droplet through the channel. Fluid shear is known to increase crystal nucleation rates[82]. This may cause a fraction of the droplets to undergo nucleation within the very short travel time of less than one second. However, once the droplets reach the storage matrix, they become stationary, and any droplets that have not yet undergone nucleation enter a new kinetic regime. This could suggest that the fluid shear during the droplet transition period may play a crucial role in inducing the nearly instant nucleation phenomenon. However, the appearance of two nucleation regimes has been observed in other works under static conditions that don't involve microfluidic devices and, therefore, an alternative explanation might be more appropriate.

An alternative explanation could be micromixing at the interface of the fluids at the Y-junction or the diffusion of miscible liquids between each other as they travel down the tube (Figure 5.3). This could lead to pockets of extreme supersaturation where a small aliquot of NaOH solution has mixed with the HCl solution bulk causing a localized pH shift to well below the solubility, precipitating nucleation[83].

Nucleation rates are a stochastic phenomenon and as such the same experiment can often produce markedly different results. Numerous factors have been attributed as having an effect on nucleation rate. White and Frost posited that an accelerated nucleation rate of potassium nitrate in water in oil droplets was catalysed by impurities in a fraction of the droplets[76]. This was mitigated by using recrystallized potassium nitrate to exclude impurities which produced a slower nucleation rate. Similarly, microfluidic experiments conducted by Seltzer[75] using potassium nitrate were similarly observed to have a fast nucleating component and a slow nucleating component. They suggest that the fast nucleation phenomenon is dictated by heterogenous nucleation caused by the presence of impurities in those droplets. When all droplets containing impurities have nucleated, nucleation becomes dominated by another, unknown mechanism which they suggest is due to impurities specifically at the liquid-liquid interface of oil and solution. However, McKechnie [84] showed that increasing the volume of oil in contact with a solution did not affect nucleation rate. Alternatively, it has been shown that an oil-solution interfaces enhances nucleations through molecular dynamics simulations [85] that glycine accumulates in higher concentrations at an oil-water interface with tridecane leading to a higher supersaturation ratio at surfaces. Ildefonso [86] argued that the selection of oil used to suspend microfluidic droplets also has an influence on collected nucleation rates due to changes in interfacial energies and kinetic pre-exponential factors.

Interfacial surface effects between oil and solution affects nucleation rate. This has great relevance to this work as the variability in droplet sizes and therefore surface area in contact with oil could be affect changes in nucleation rate. As droplet volume increases but supersaturation remains the same, nucleation rate should also stay the same, independent of the volume. However, the surface area in contact with the oil will change and this would affect the nucleation rate. Future work could analyse nucleation rate data collected at different droplet volumes. This would require further iterations of the microfluidic device to improve process control, including temperature control, better droplet size control and storage.

In addition, classical nucleation theory, from which the equations and fitting models used above are derived, may not be a suitable model for analysis. Dela Cruz et al. [77] showed that the act of confinement hindered nucleation and that, under such conditions, there exists a different nucleation pathway. This work was conducted at 100μl, significantly less confined than this work. They argue that the CNT cannot adequately explain crystal nucleation in confined, small volumes.

6.5 Discussion of Crystal16 and Microfluidic Acquired Nucleation Rate Data

Nucleation rate data collected in the Crystal16 was compared to that from the microfluidic device. Data from the microfluidic device were collected under significantly smaller volumes and as a result a much greater nucleation rate, and therefore higher supersaturation, is needed to achieve nucleation in the same time frame for analysis. $J \times v$ values for both measurement types have comparable orders of magnitude as the reciprocal of $J \times v$ is the characteristic time, i.e. the timescale in which nucleation events occur. For all nucleation rate experiments conducted across literature the time window for observing nucleation is consistently in the range of minutes to hours, i.e. within two orders of magnitude. Therefore, for nucleation rate data to be collected, conditions must be set in order that nucleation occurs within the observation window. Therefore, if volume were altered, nucleation rate data collected would have a Jv that falls within 2 orders of magnitude of the current data regardless of supersaturation data.

Figure 6.6 presents the two datasets on a natural logarithmic scale as the nucleation rate in the microfluidic device, being orders of magnitude lower in volume, is orders of magnitude greater than the Crystal16. The slow nucleation regime rate data, J_2, from microfluidic device 4 (pH 9 - 9.3) was fitted alongside the data collected from agitated vials in the Crystal16 at pH values 9.2 - 9.5 using the equation: $\mathrm{Ln}J = A \times \mathrm{Ln}(S-1) + B$. This fitting produced similar parameters to those acquired from fitting the Crystal16 data alone (Table 6.4) further reinforcing that the relationship between J and S does hold true.

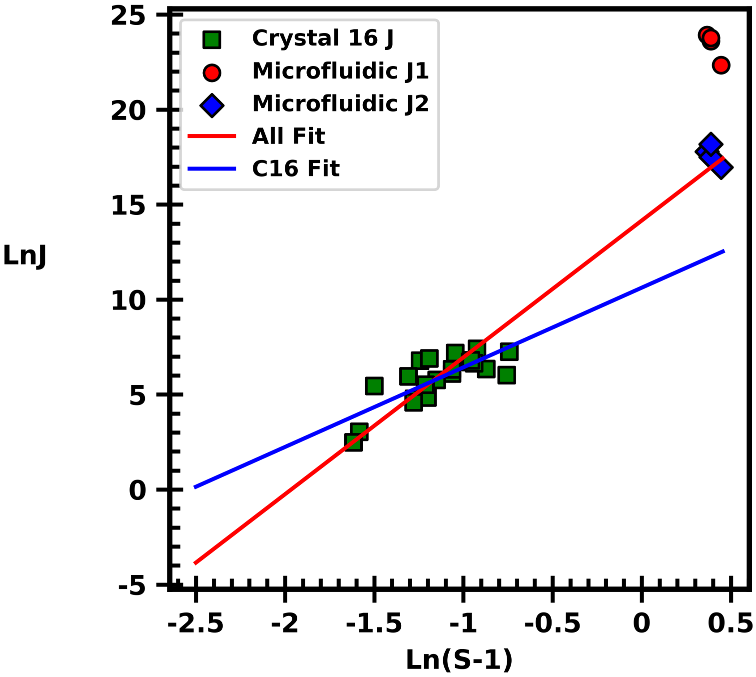

Figure 6.6: Microfluidic data using device 4 and Crystal16 data compared using LnJ and LN$S-1$. "All Fit" line was fitted using the the microfluidic $J2$ value and the nucleation rates collected from agitated vials in the Crystal16. The "C16 Fit" line was fitted using solely nucleation rates collected from agitated vials in the Crystal16.

Figure 6.6 offers several opportunities for future investigations. A volumetric analysis of nucleation rate could be conducted to fill in the space between the Crystal16 data and the microfluidic data. As volume is decreased, a greater supersaturation ratio is required to produce nucleation in the time frame required, filling in the space in the graph. Comparing induction times in non-agitated solutions of DL-phenylalanine in the Crystal16 to both the agitated Crystal16 data and the non-agitated microfluidic data could provide further insight into the mechanisms at play in the different nucleation phases shown in this work.

Method	A	B	R^2
Crystal16 pH 9.2 - 9.5	4.19	10.62	0.612
Crystal 16 pH 9.2 - 9.5 & Microfluidic	7.2	14.15	0.945

Table 6.4: Table of coefficients for fitting exclusively Crystal16 nucleation rate data and combined slowly nucleating microfluidic regime and Crystal16 nucleation rate data.

Other potential work could be the comparison of surface area to volume ratios using different microfluidic volumes. As the characteristic time remains approximately the same it would be an interesting avenue of exploration to assess any present relationship between nucleation rate and surface area of the droplet in contact with the oil. Alternatively, analysis of the affect of an oil interface could also be analysed by using a similar setup to McKechnie et al. [79] where non-agitated vials of solution were nucleated in contact with tridecane oil. Vials of different diameter and depth could be used to maintain the same volume while altering the surface area in contact with the solution.

6.6 Conclusions

The aim of this work was to utilize a novel microfluidic device to collect nucleation rate data in a pH-shift crystallization system. This work presents that data and compares the collected data with that of an established isothermal agitated vial technique.

Droplets were found to nucleate in two different regimes: instant or very fast nucleation and slower nucleation, while some droplets did not nucleate within the experimental time frame. This data was fitted to a double exponential fit, similar to other non-agitated nucleation rate measurements in the literature. The first exponential accounted for nucleation in the fast regime and the second the slower regime. Fitting assumes that in a longer experiment the remaining droplets would nucleate according to the slower regimes nucleation kinetics. Nucleation rate data was collected for significantly higher supersaturation ratios than earlier experiments. The nucleation data collected gave values for nucleation rate within 2 orders of magnitude greater at significantly higher supersaturations compared to larger scale experiments conducted in the Crystal16 due to the requirement that nucleation occurred within the observation window frame of experiments. Future work could look at the effect of volume and agitation on nucleation in these different experimental setups.

Chapter 7

Conclusions

Crystal nucleation is a vital step in the crystallization process and plays an important role in determining the crystal quality attributes required by industrial processes in numerous fields. New tools for understanding how nucleation proceeds are a necessary step in the development of better crystallization unit operations. Greater understanding will allow for better design, optimization and control of future crystallization processes.

pH-dependent solubility was selected as the mechanism for generating solution supersaturation. This complex system is very difficult to predict as changes in concentration effect pH changes. Previously described models required initial solution pH values as an input for supersaturation prediction. In Chapter 3 we present a model for determining the solubility and supersaturation of solutions of DL-phenylalanine at different pH values from solution compositional data and dissociation constants. The model utilizes material balances and solute dissociation constant to predict pH, solubility and supersaturation of a given solution. The model was compared to experimentally acquired and literature data for pH-dependent solubility and was found to give solution speciation and supersaturation properties to a sufficient degree of accuracy to guide further crystallization experiments. The non-ideality of the solutions was incorporated into the model using the Davies Equation. However, while this particular activity model was accurate for pH, solubility and supersaturation prediction were less accurate. Further refinement of this model could be conducted through the application of a more detailed activity coefficient model that was beyond the scope of this current work. In addition, this model could be expanded to include the effect of crystal mass growth on pH and supersaturation. The model presented here, however, is adequate for exploring the pH-shift crystallization design space required here.

Chapter 4 was a study of crystal nucleation rate through the acquisition and fitting of induction times in a pH-dependent solubility system using agitated vials under isothermal conditions. It was possible to estimate nucleation rates in the pH range 9-9.8. The metastable zone limit was established and the lower limit for supersaturation at which nucleation rate data could be collected was reported. It was attempted to fit the nucleation rate data to commonly used nucleation models (such as the KJMA equation), however, these models were found to be inadequate at describing the variability in the data. Other equations were used for fitting the data, in some cases incorporating pH and ionic strength to ascertain any relationship between pH and nucleation rate apart from supersaturation. While some models showed a significant trend of nucleation rate with increasing supersaturation, as expected, this was also confounded by dependence on pH and ionic strength. It was found that the nucleation rate generally increased with both pH and ionic strength at a given supersaturation but the statistical significance of this was limited. Future studies in this system would require a significant increase in data collected within the metastable zone at a broader range of pH values and ionic strengths. Fitting could then be attempted with more data available. Alternatively, a machine learning model could be developed to reveal any further relationships in the data.

The aim of chapter 5 was to develop a microfluidic tool for gathering induction times under isothermal conditions to calculate crystal nucleation rates. The device employed the rapid mixing to produce supersaturation by bringing together a high pH solution containing the solute with a strong acid to lower the pH. The droplets produced could be examined for nucleation events for up to 10000 seconds through microscope imaging. The device's shortcomings were that the droplet volume varied, the solvent pervaporated through PDMS during the observation window, inadequate temperature control, and no more than 50 droplets could be obtained in the observation window.

In chapter 6 nucleation rate data was collected from a novel device using pH-shift crystallization under isothermal conditions and compared with rate data collected using an agitated vial isothermal method at equivalent pH values. Two distinct nucleation regimes were discovered, with some droplets subject to rapid nucleation, other droplets nucleating at a slower rate and some droplets failing to nucleate. The resulting distribution of induction times were fitted to a double exponential curve, similar to other non-agitated nucleation rate measurements in previous literature. The first exponential component explained nucleation in the rapid regime, and the second accounted for the slower regime. The fitting assumed that the remaining droplets would nucleate according to the slower regime's nucleation kinetics in a lengthier experiment. Nucleation rate information was collected at significantly higher supersaturation ratios than in agitated vial experiments, providing values for nucleation rates that were some orders of magnitude greater than in larger-scale experiments carried out in the Crystal16.

The work presented in this thesis could be enhanced by implementing a more detailed solution activity model into the speciation model detailed in chapter 3. This would allow the exploration of a broader range of pH values, potentially increasing clarity with regard to the effect of pH on nucleation. In addition, the microfluidic device could be improved to reduce uncertainty. Improving the rate of droplet trapping and incorporating osmolality and temperature control could reduce the uncertainty in these measurements by reducing the volume lost and increasing the number of nucleations observed. Beyond this, further research could investigate the impact of volume and agitation on nucleation in these various experimental settings.

Bibliography

[1] John William Mullin. *Crystallization.* Butterworth-Heinemann, 4 edition, 2001.

[2] F. Bea, N. Bortnikov, A. Cambeses, S. Chakraborty, J.F. Molina, P. Montero, I. Morales, S. Silantiev, and T. Zinger. Zircon crystallization in low-zr mafic magmas: Possible or impossible? *Chemical Geology*, 602:120898, 7 2022.

[3] James M. Campbell, Fiona C. Meldrum, and Hugo K. Christenson. Observing the formation of ice and organic crystals in active sites. *Proceedings of the National Academy of Sciences*, 114:810–815, 1 2017.

[4] Helen H. Wang, Piero Portincasa, Min Liu, and David Q.-H. Wang. Effects of biliary phospholipids on cholesterol crystallization and growth in gallstone formation. *Advances in Therapy*, 40:743–768, 3 2023.

[5] Ajay Pande, Jayanti Pande, Neer Asherie, Aleksey Lomakin, Olutayo Ogun, Jonathan King, and George B. Benedek. Crystal cataracts: Human genetic cataract caused by protein crystallization. *Proceedings of the National Academy of Sciences*, 98:6116–6120, 5 2001.

[6] Brice Martin Couillaud, Philippe Espeau, Nathalie Mignet, and Yohann Corvis. State of the art of pharmaceutical solid forms: from crystal property issues to nanocrystals formulation. *ChemMedChem*, 14:8–23, 1 2019.

[7] Christian Kocks, Christina Maria Krekel, Marcel Gausmann, and Andreas Jupke. Determination of the metastable zone width and nucleation parameters of succinic acid for electrochemically induced crystallization. *Crystals*, 11:1090, 9 2021.

[8] Nadine Candoni, Romain Grossier, Mehdi Lagaize, and Stéphane Veesler. Advances in the use of microfluidics to study crystallization fundamentals. *Annual Review of Chemical and Biomolecular Engineering*, 10:59–83, 6 2019. PMID: 31018097.

[9] S. Veesler and F. Puel. Crystallization of pharmaceutical crystals. *Handbook of Crystal Growth: Second Edition*, 1:915–949, 1 2015.

[10] Joop H. ter Horst, Christiane Schmidt, and Joachim Ulrich. Fundamentals of industrial crystallization. *Handbook of Crystal Growth: Bulk Crystal Growth: Second Edition*, 2:1317–1349, 1 2015.

[11] D. Kashchiev and G. M. Van Rosmalen. Review: Nucleation in solutions revisited. *Crystal Research and Technology*, 38:555–574, 2003.

[12] Matthew A. McDonald, Hossein Salami, Patrick R. Harris, Colton E. Lagerman, Xiaochuan Yang, Andreas S. Bommarius, Martha A. Grover, and Ronald W. Rousseau. Reactive crystallization: a review. *Reaction Chemistry & Engineering*, 6:364–400, 3 2021.

[13] Xiaochuan Yang, Bipul Sarma, and Allan S. Myerson. Polymorph control of micro/nano-sized mefenamic acid crystals on patterned self-assembled monolayer islands. *Crystal Growth and Design*, 12:5521–5528, 11 2012.

[14] Peter G. Vekilov. The two-step mechanism of nucleation of crystals in solution. *Nanoscale*, 2:2346, 11 2010.

[15] Fiora Artusio and Roberto Pisano. Surface-induced crystallization of pharmaceuticals and biopharmaceuticals: A review. *International Journal of Pharmaceutics*, 547:190–208, 8 2018.

[16] Charline J.J. Gerard, Maria L. Briuglia, Nazer Rajoub, Teresa F. Mastropietro, Wenqian Chen, Jerry Y.Y. Heng, Gianluca Di Profio, and Joop H. ter Horst. Template-assisted crystallization behavior in stirred solutions of the monoclonal antibody anti-cd20: Probability distributions of induction times. *Crystal Growth and Design*, 22:3637–3645, 2022.

[17] Roger J. Davey, Sven L. M. Schroeder, and Joop H. ter Horst. Nucleation of organic crystals-a molecular perspective. *Angewandte Chemie International Edition*, 52:2166–2179, 2 2013.

[18] Dimo Kashchiev. Classical nucleation theory approach to two-step nucleation of crystals. *Journal of Crystal Growth*, 530, 1 2020.

[19] Stefan Auer and Dimo Kashchiev. Two-step crystal nucleation kinetics: Solution of the master equation. *Journal of Crystal Growth*, 580, 2 2022.

[20] Cedric Devos, Tom Van Gerven, and Simon Kuhn. A review of experimental methods for nucleation rate determination in large-volume batch and microfluidic crystallization. *Crystal Growth & Design*, 21:2541–2565, 4 2021.

[21] Wilhelm Ostwald. Studien Über die bildun und umwandlung fester körper. *Zeitschrift für Physikalische Chemie*, 22:289–330, 1897.

[22] Allan S. Myerson, Deniz Erdemir, and Alfred Y. Lee, editors. *Handbook of Industrial Crystallization*. Cambridge University Press, 6 2019.

[23] Noriaki Kubota. A new interpretation of metastable zone widths measured for unseeded solutions. *Journal of Crystal Growth*, 310:629–634, 2 2008.

[24] Jian Liu, Catherine E. Nicholson, and Sharon J. Cooper. Direct measurement of critical nucleus size in confined volumes. *Langmuir*, 23:7286–7292, 6 2007.

[25] Shanfeng Jiang and Joop H. ter Horst. Crystal nucleation rates from probability distributions of induction times. *Crystal Growth & Design*, 11:256–261, 1 2011.

[26] Stephanie Yerdelen, Yihui Yang, Justin L. Quon, Charles D. Papageorgiou, Chris Mitchell, Ian Houson, Jan Sefcik, Joop H. ter Horst, Alastair J Florence, and Cameron J. Brown. Machine learning-derived correlations for scale-up and technology transfer of primary nucleation kinetics. *Crystal Growth & Design*, 23:681–693, 2 2023.

[27] Pijush K. Kundu, Ira M. Cohen, and David R. Dowling. Laminar flow. *Fluid Mechanics*, pages 409–467, 1 2016.

[28] Todd Thorsen, Richard W. Roberts, Frances H. Arnold, and Stephen R. Quake. Dynamic pattern formation in a vesicle-generating microfluidic device. *Phys. Rev. Lett.*, 86:4163–4166, Apr 2001.

[29] Haihu Liu and Yonghao Zhang. Droplet formation in a t-shaped microfluidic junction. *Journal of Applied Physics*, 106:034906, 8 2009.

[30] Jean-Christophe Baret. Surfactants in droplet-based microfluidics. *Lab Chip*, 12:422–433, 2012.

[31] Hsieng-Cheng Tseng, Ching-Yi Lee, Wen-Lu Weng, and I-Min Shiah. Solubilities of amino acids in water at various ph values under 298.15k. *Fluid Phase Equilibria*, 285:90–95, 11 2009.

[32] Robert de Levie. *Aqueous Acid-Base Equilibria and Titrations*, volume 1. Oxford University Press, 1 edition, 1999.

[33] Roger J. Davey and Helen P. Jones. The crystallisation and stability of a polymorphic salt, ethylene diammonium dinitrobenzoate. *New Journal of Chemistry*, 32:1686–1692, 2008.

[34] H. P. Jones, R. J. Davey, and B. G. Cox. Crystallization of a salt of a weak organic acid and base: Solubility relations, supersaturation control and polymorphic behavior. *Journal of Physical Chemistry B*, 109:5273–5278, 3 2005.

[35] Hannu Alatalo, Jarno Kohonen, Haiyan Qu, Henry Hatakka, Satu Pia Reinikainen, Marjatta Louhi-Kultanen, and Juha Kallas. In-line monitoring of reactive crystallization process based on atr-ftir and raman spectroscopy. *Journal of Chemometrics*, 22:644–652, 11 2008.

[36] Hannu M. Alatalo, Henry Hatakka, Marjatta Louhi-Kultanen, Jarno Kohonen, and Satu Pia Reinikainen. Closed-loop control of reactive crystallization. part i: Supersaturation-controlled crystallization of l-glutamic acid. *Chemical Engineering and Technology*, 33:743–750, 5 2010.

[37] Hannu Alatalo, Henry Hatakka, Jarno Kohonen, Satu Pia Reinikainen, and Marjatta Louhi-Kultanen. Process control and monitoring of reactive crystallization of l-glutamic acid. *AIChE Journal*, 56:2063–2076, 8 2010.

[38] Henry Hatakka, Hannu Alatalo, Marjatta Louhi-Kultanen, Ilkka Lassila, and Edward Hæggström. Closed-loop control of reactive crystallization part ii: Polymorphism control of l-glutamic acid by sonocrystallization and seeding. *Chemical Engineering and Technology*, 33:751–756, 5 2010.

[39] A. Borissova, Y. Jammoal, K. H. Javed, X. Lai, T. Mahmud, R. Penchev, K. J. Roberts, and W. Wood. Modeling the precipitation of l-glutamic acid via acidification of monosodium glutamate. *Crystal Growth and Design*, 5:845–854, 5 2005.

[40] Sukanya Srisanga and Joop H. Ter Horst. Racemic compound, conglomerate, or solid solution: Phase diagram screening of chiral compounds. *Crystal Growth and Design*, 10:1808–1812, 4 2010.

[41] J. Vellema, N. G.M. Hunfeld, H. E.A. Van Den Akker, and J. H. Ter Horst. Avoiding crystallization of lorazepam during infusion. *European Journal of Pharmaceutical Sciences*, 44:621–626, 12 2011.

[42] Martin Wijaya Hermanto, Guangwen He, Martin Tjahjono, Pui Shan Chow, Reginald B.H. Tan, and Marc Garland. Calibration of dielectric constant measurements to improve the detection of cloud and clear points in solution crystallization. *Chemical Engineering Research and Design*, 89:2613–2619, 12 2011.

[43] Franziska Stefanie Ihlefeldt, Fredrik Bjarte Pettersen, Aidan von Bonin, Malgorzata Zawadzka, and Carl Henrik Görbitz. The polymorphs of l-phenylalanine. *Angewandte Chemie International Edition*, 53:13600–13604, 12 2014.

[44] John B. Dalton and Carl L.A. Schmidt. The solubilities of certain amino acids in water, the densities of their solutions at twenty-five degrees, and the calculated heats of solution and partial molal volumes. *Journal of Biological Chemistry*, 103:549–578, 12 1933.

[45] Srabani Ghosh, Samiran Mondal, Sanjay Roy, Soumen Saha, Dushila Subba, and Bijoy Krishna Dolui. Evaluation and correlation of solubility and solvation energetics of dl-phenylalanine and dl-serine in water and aqueous ethylene glycol solutions. *Journal of Molecular Liquids*, 249:659–665, 1 2018.

[46] Renzo Carta. Solubilities ofl-cystine,l-tyrosine,l-leucine, and glycine in sodium chloride so-

lutions at various ph values. *The Journal of Chemical Thermodynamics*, 30:379–387, 3 1998.

[47] Renzo Carta. Solubilities ofl-cystine,l-tyrosine,l-leucine, and glycine in sodium chloride solutions at various ph values. *The Journal of Chemical Thermodynamics*, 30:379–387, 3 1998.

[48] Ching-Yi Lee, Jui-Tang Chen, Wen-Tung Chang, and I-Min Shiah. Effect of ph on the solubilities of divalent and trivalent amino acids in water at 298.15k. *Fluid Phase Equilibria*, 343:30–35, 4 2013.

[49] Sadaichi Miyamoto and Carl L.A. Schmidt. The apparent dissociation constants of phenylalanine and of dihydroxyphenylalanine and the apparent free energy and entropy changes of certain amino acids due to ionization. *Journal of Biological Chemistry*, 90:165–178, 1 1931.

[50] Leslie J. Harris. The titration of amino- and carboxyl-groups in amino-acids, polypeptides, etc. parts i-iii.–investigations with aqueous solutions. *Proceedings of the Royal Society of London. Series B, Containing Papers of a Biological Character*, 95(670):440–484, 1923.

[51] Clemente Bretti, Ottavia Giuffrè, Gabriele Lando, and Silvio Sammartano. Modeling solubility and acid–base properties of some amino acids in aqueous nacl and (ch3)4ncl aqueous solutions at different ionic strengths and temperatures. *SpringerPlus*, 5, 12 2016.

[52] S Olsztynska, M Komorow Ska, L Vrielynck, and N Dupuy. Vibrational spectroscopic study of l-phenylalanine: Effect of ph. *APPLIED SPECTROSCOPY*, 55, 2001.

[53] Farhoush Kiani, Abbas Ali Rostami, Sasan Sharifi, Azar Bahadori, and Mohammad Javad Chaichi. Determination of acidic dissociation constants of glycine, valine, phenylalanine,

glycylvaline, and glycylphenylalanine in water using ab initio methods. *Journal of Chemical and Engineering Data*, 55:2732–2740, 8 2010.

[54] Hidetada Nagai, Ko Kuwabara, and Giorgio Carta. Temperature dependence of the dissociation constants of several amino acids. *Journal of Chemical and Engineering Data*, 53:619–627, 3 2008.

[55] John McGinty, Helen Wheatcroft, Chris J. Price, and Jan Sefcik. Modelling solution speciation to predict ph and supersaturation for design of batch and continuous organic salt crystallisation processes. *Fluid Phase Equilibria*, 565:113676, 2 2023.

[56] Cecil Whitfield Davies. *Ion Association*. Butterworths, 1962.

[57] Diego Barba, Vincenzo Brandani, and Gabrielle di Giacomo. A thermodynamic model of caso4 solubility in multicomponent aqueous solutions. *The Chemical Engineering Journal*, 24:191–200, 1 1982.

[58] Dimo Kashchiev. *Nucleation: Basic Theory with Application*. Butterworth-Heinemann, Woburn, MA, 2000.

[59] Malcolm J.W. Povey. Crystal nucleation in food colloids. *Food Hydrocolloids*, 42:118–129, 12 2014.

[60] Melvin Avrami. Kinetics of phase change. i general theory. *The Journal of Chemical Physics*, 7:1103–1112, 12 1939.

[61] Melvin Avrami. Kinetics of phase change. ii transformation-time relations for random distribution of nuclei. *The Journal of Chemical Physics*, 8:212–224, 2 1940.

[62] Melvin Avrami. Granulation, phase change, and microstructure kinetics of phase change. iii. *The Journal of Chemical Physics*, 9:177–184, 2 1941.

[63] Jiao Yang, Benjamin J. McCoy, and Giridhar Madras. Distribution kinetics of polymer crystallization and the avrami equation. *The Journal of Chemical Physics*, 122:064901, 2 2005.

[64] Jacques Leng and Jean-Baptiste Salmon. Microfluidic crystallization. *Lab Chip*, 9:24–34, 2009.

[65] Albert Folch. *Introduction to BioMEMS*. CRC Press, 4 2016.

[66] J. Cooper McDonald, David C. Duffy, Janelle R. Anderson, Daniel T. Chiu, Hongkai Wu, Olivier J. A. Schueller, and George M. Whitesides. Fabrication of microfluidic systems in poly(dimethylsiloxane). *Electrophoresis*, 21:27–40, 1 2000.

[67] J. Cooper McDonald and George M. Whitesides. Poly(dimethylsiloxane) as a material for fabricating microfluidic devices. *Accounts of Chemical Research*, 35:491–499, 7 2002.

[68] Dong Qin, Younan Xia, and George M Whitesides. Soft lithography for micro- and nanoscale patterning. *Nature Protocols*, 5:491–502, 3 2010.

[69] Sameer Talreja, David Y. Kim, Amir Y. Mirarefi, Charles F. Zukoski, and Paul J.A. Kenis. Screening and optimization of protein crystallization conditions through gradual evaporation using a novel crystallization platform. *Journal of Applied Crystallography*, 38:988–995, 12 2005.

[70] Sandy Morais, Gérald Clisson, Teresa Fina Mastropietro, Maria L. Briuglia, Joop H. Ter Horst, Jacques Leng, and Jean Baptiste Salmon. Easy-to-use osmosis-based microfluidic

chip for protein crystallization: Application to a monoclonal antibody. *Crystal Growth and Design*, 21:3469–3476, 6 2021.

[71] Kay S. McMillan, Marie Boyd, and Michele Zagnoni. Transitioning from multi-phase to single-phase microfluidics for long-term culture and treatment of multicellular spheroids. *Lab on a Chip*, 16:3548–3557, 2016.

[72] Hakim Boukellal, Šeila Selimović, Yanwei Jia, Galder Cristobal, and Seth Fraden. Simple, robust storage of drops and fluids in a microfluidic device. *Lab Chip*, 9:331–338, 2009.

[73] Swastika S. Bithi, William S. Wang, Meng Sun, Jerzy Blawzdziewicz, and Siva A. Vanapalli. Coalescing drops in microfluidic parking networks: A multifunctional platform for drop-based microfluidics. *Biomicrofluidics*, 8:034118, 5 2014.

[74] Christian H.J. Schmitz, Amy C. Rowat, Sarah Köster, and David A. Weitz. Dropspots: A picoliter array in a microfluidic device. *Lab on a Chip*, 9:44–49, 2009.

[75] Daniel Selzer, Corinna Frank, and Matthias Kind. On the effect of the continuous phase on primary crystal nucleation of aqueous kno 3 solution droplets. *Journal of Crystal Growth*, 517:39–47, 7 2019.

[76] Malcolm L White and Arthur A Frost. The rate of nucleation of supersaturated potassium nitrate solutions. *Journal of Colloid Science*, 14:247–251, 6 1959.

[77] Isaac Jerome C. Dela Cruz, Jem Valerie Perez, Bryan Gencianeo Alamani, Gerard Capellades, and Allan S. Myerson. Influence of volume on the nucleation of model organic molecular crystals through an induction time approach. *Crystal Growth and Design*, 21:2932–2941, 5 2021.

[78] Nadeem Javid, Thomas Kendall, Iain S. Burns, and Jan Sefcik. Filtration suppresses laser-induced nucleation of glycine in aqueous solutions. *Crystal Growth and Design*, 16:4196–4202, 8 2016.

[79] David Mckechnie and Karen Johnston. *Heterogeneous Nucleation at Hydrophobic Interfaces. PhD thesis.* 2021.

[80] Laurie J. Little, Richard P. Sear, and Joseph L. Keddie. Does the γ polymorph of glycine nucleate faster? a quantitative study of nucleation from aqueous solution. *Crystal Growth and Design*, 15:5345–5354, 11 2015.

[81] Maria J. Vesga, David McKechnie, Paul A. Mulheran, Karen Johnston, and Jan Sefcik. Conundrum of γ glycine nucleation revisited: to stir or not to stir? *CrystEngComm*, 21:2234–2243, 2019.

[82] Jin Liu and Åke C. Rasmuson. Influence of agitation and fluid shear on primary nucleation in solution. *Crystal Growth & Design*, 13:4385–4394, 10 2013.

[83] Amit K. Thakur, Rahul Kumar, V.K. Vipin Kumar, Amit Kumar, Gajendra Kumar Gaurav, and Kaushal Naresh Gupta. A critical review on thermodynamic and hydrodynamic modeling and simulation of liquid antisolvent crystallization of pharmaceutical compounds. *Journal of Molecular Liquids*, 362:119663, 9 2022.

[84] David McKechnie, Samira Anker, Saraf Zahid, Paul A. Mulheran, Jan Sefcik, and Karen Johnston. Interfacial concentration effect facilitates heterogeneous nucleation from solution. *Journal of Physical Chemistry Letters*, 11:2263–2271, 3 2020.

[85] David McKechnie, Paul A. Mulheran, Jan Sefcik, and Karen Johnston. Tuning interfa-

cial concentration enhancement through dispersion interactions to facilitate heterogeneous nucleation. *The Journal of Physical Chemistry C*, 126:16387–16400, 9 2022.

[86] Manuel Ildefonso, Nadine Candoni, and Stéphane Veesler. Heterogeneous nucleation in droplet-based nucleation measurements. *Crystal Growth and Design*, 13:2107–2110, 5 2013.

Chapter 8

Appendices

8.1 All experimental data for induction time experiments deemed sufficient and subsequent fitting.

pH	S	J	tg	σJ	σtg	Ii	Number Nucleated
9.68	1.27	1802	185	228	27	0.59	80
9.25	1.40	1628	1066	150	30	0.59	77
9.23	1.48	1398	201	121	50	0.59	80
9.24	1.35	1312	916	165	59	0.59	80
9.71	1.17	1022	563	94	45	0.59	75
9.28	1.30	1008	507	108	50	0.59	80
9.01	1.42	996	717	96	50	0.59	73
9.24	1.38	934	711	88	59	0.59	71
9.29	1.29	873	1356	88	72	0.59	80
9.26	1.38	819	792	76	61	0.59	61
9.26	1.39	767	820	87	51	0.59	80
9.25	1.42	568	764	67	93	0.59	80
9.35	1.35	556	598	79	82	0.59	80
9.27	1.35	450	2310	56	93	0.59	11
9.21	1.47	412	895	50	98	0.59	62
9.29	1.27	384	1723	49	103	0.59	80
9.02	1.39	328	864	49	123	0.59	80
9.28	1.32	318	466	56	126	0.61	80
9.74	1.09	252	1563	25	201	0.61	80
9.37	1.30	250	752	30	145	0.63	12
9.32	1.22	232	1263	29	161	0.55	50
9.27	1.30	127	2741	12	263	0.55	52
9.29	1.28	119	3642	10	334	0.56	77
9.44	1.28	99	5851	8	400	0.56	37
9.03	1.29	84	907	10	354	0.76	80
9.78	1.00	70	5044	5	439	0.76	14
9.12	1.19	52	2642	5	532	0.76	74
9.30	1.21	20	7103	4	725	0.76	41

Table 8.1: All experimental data for successful induction time experiments. Vials recorded as nucleating here were out of 80 vials total, any remaining vials did not nucleate during the observation window of four hours.

pH	S	Number Nucleated
9.40	0.96	0
9.36	1.10	0
9.35	1.06	0
9.33	1.12	0
9.63	0.83	0
9.56	0.97	0
9.18	0.95	0
9.15	1.02	0
9.16	1.04	0
9.94	0.69	0
9.90	0.77	0

Table 8.2: All experimental data for induction time experiments deemed insufficient for fitting. Vials recorded as nucleating here were out of 80 vials total, any remaining vials did not nucleate during the observation window of four hours.

pH	S	Number Nucleated
9.14	1.71	0
9.24	1.41	0
9.19	1.56	79
9.15	1.68	37
9.29	1.54	71
9.33	1.41	76
9.36	1.55	70
9.26	1.94	0
8.98	1.48	60
9.01	1.45	51

Table 8.3: All experimental data induction time experiments deemed excessive. Vials recorded as nucleating here were out of 80 vials total and represented the vials that nucleated after reaching the isothermal point. No vials nucleated outside of the observation window.

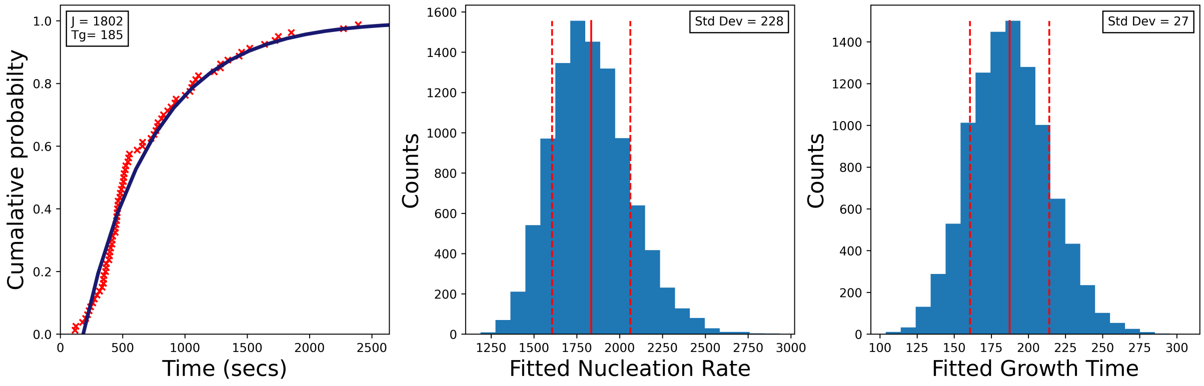
J = 1802
Tg= 185
Cumalative probabilty
Time (secs)
0
500
1000
1500
2000
2500
0.0
0.2
0.4
0.6
0.8
1.0
Std Dev = 228
Counts
Fitted Nucleation Rate
1250
1500
1750
2000
2250
2500
2750
3000
0
200
400
600
800
1000
1200
1400
1600
Std Dev = 27
Counts
Fitted Growth Time
100
125
150
175
200
225
250
275
300
0
200
400
600
800
1000
1200
1400

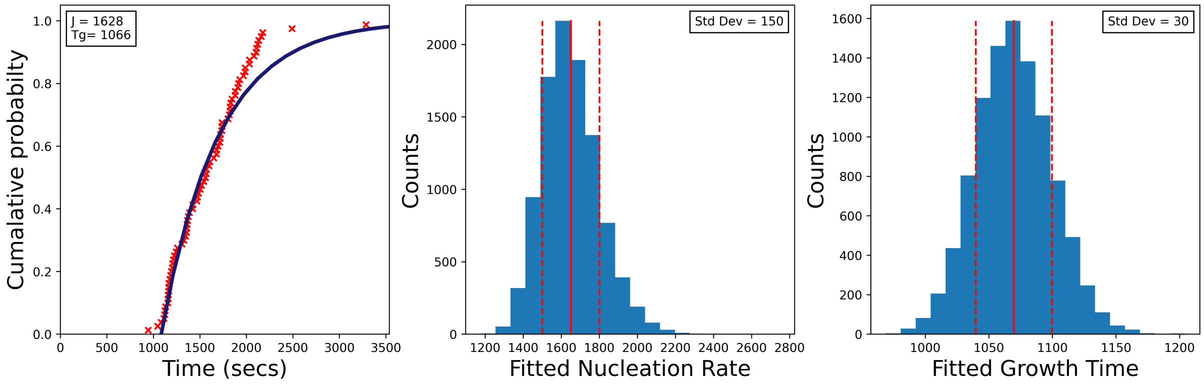
J = 1628
Tg= 1066
Cumalative probabilty
Time (secs)
0
500
1000
1500
2000
2500
3000
3500
0.0
0.2
0.4
0.6
0.8
1.0
Std Dev = 150
Counts
Fitted Nucleation Rate
1200
1400
1600
1800
2000
2200
2400
2600
2800
0
500
1000
1500
2000
Std Dev = 30
Counts
Fitted Growth Time
1000
1050
1100
1150
1200
0
200
400
600
800
1000
1200
1400
1600

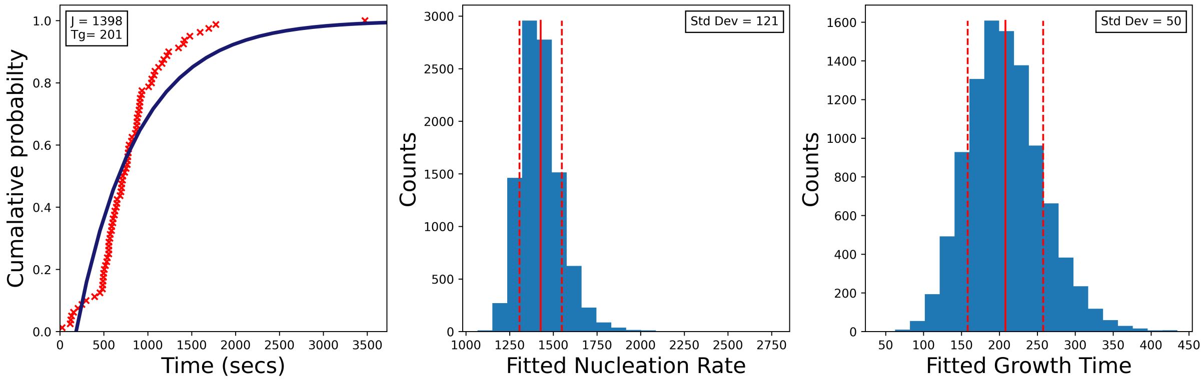
J = 1398
Tg= 201
Cumalative probabilty
Time (secs)
0
500
1000
1500
2000
2500
3000
3500
0.0
0.2
0.4
0.6
0.8
1.0
Std Dev = 121
Counts
Fitted Nucleation Rate
1000
1250
1500
1750
2000
2250
2500
2750
0
500
1000
1500
2000
2500
3000
Std Dev = 50
Counts
Fitted Growth Time
50
100
150
200
250
300
350
400
450
0
200
400
600
800
1000
1200
1400
1600

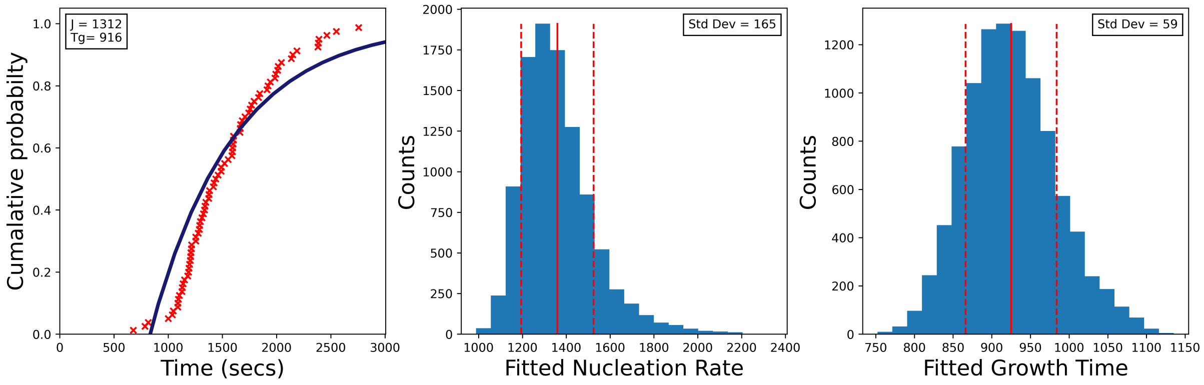
J = 1312
Tg= 916
Cumalative probabilty
Time (secs)
0
500
1000
1500
2000
2500
3000
0.0
0.2
0.4
0.6
0.8
1.0
Std Dev = 165
Counts
Fitted Nucleation Rate
1000
1200
1400
1600
1800
2000
2200
2400
0
250
500
750
1000
1250
1500
1750
2000
Std Dev = 59
Counts
Fitted Growth Time
750
800
850
900
950
1000
1050
1100
1150
0
200
400
600
800
1000
1200

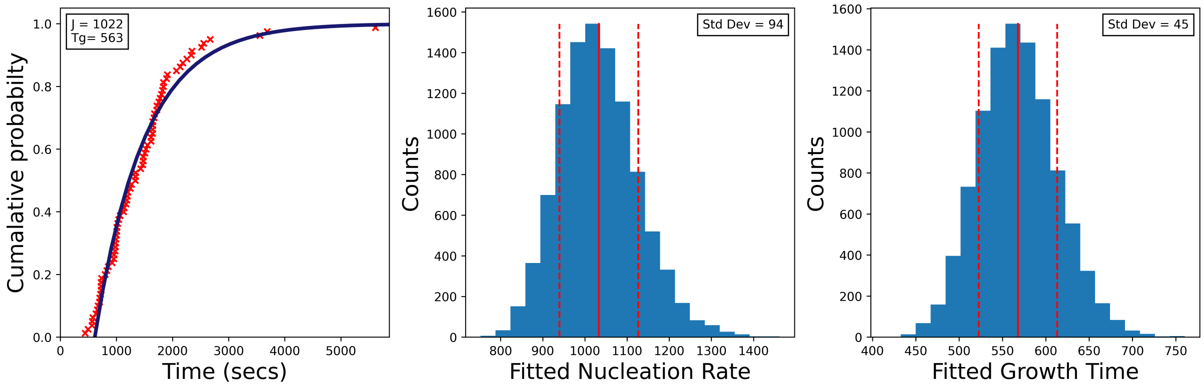
J = 1022
Tg= 563
Cumalative probabilty
Time (secs)
0.0
0.2
0.4
0.6
0.8
1.0
0
1000
2000
3000
4000
5000
Std Dev = 94
Counts
Fitted Nucleation Rate
0
200
400
600
800
1000
1200
1400
1600
800
900
1000
1100
1200
1300
1400
Std Dev = 45
Counts
Fitted Growth Time
400
450
500
550
600
650
700
750

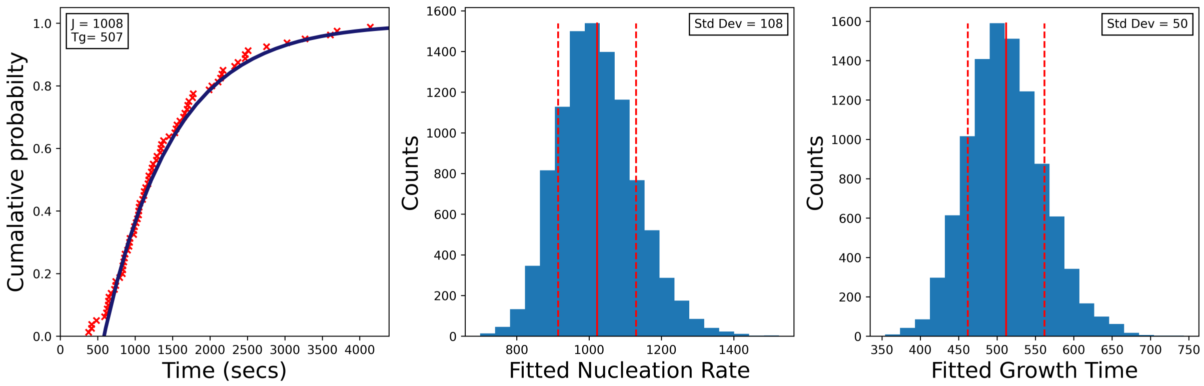
J = 1008
Tg= 507
Cumalative probabilty
Time (secs)
0.0
0.2
0.4
0.6
0.8
1.0
0
500
1000
1500
2000
2500
3000
3500
4000
Std Dev = 108
Counts
Fitted Nucleation Rate
0
200
400
600
800
1000
1200
1400
1600
800
1000
1200
1400
Std Dev = 50
Counts
Fitted Growth Time
350
400
450
500
550
600
650
700
750

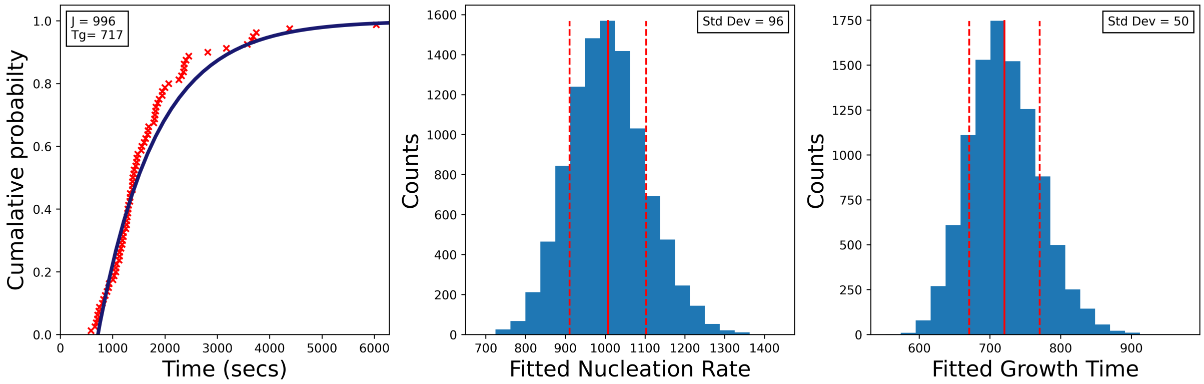
J = 996
Tg= 717
Cumalative probabilty
Time (secs)
0.0
0.2
0.4
0.6
0.8
1.0
0
1000
2000
3000
4000
5000
6000
Std Dev = 96
Counts
Fitted Nucleation Rate
0
200
400
600
800
1000
1200
1400
1600
700
800
900
1000
1100
1200
1300
1400
Std Dev = 50
Counts
Fitted Growth Time
0
250
500
750
1000
1250
1500
1750
600
700
800
900

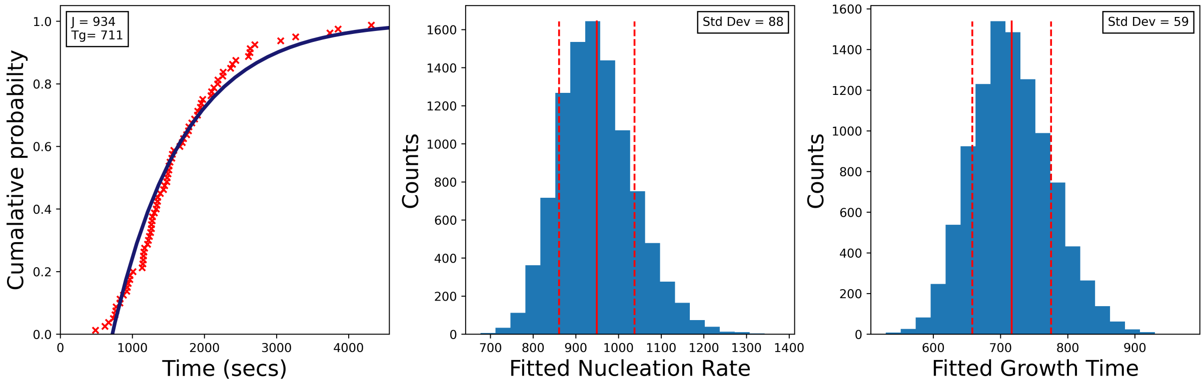
J = 934
Tg= 711
Cumalative probabilty
Time (secs)
0.0
0.2
0.4
0.6
0.8
1.0
0
1000
2000
3000
4000
Std Dev = 88
Counts
Fitted Nucleation Rate
0
200
400
600
800
1000
1200
1400
1600
700
800
900
1000
1100
1200
1300
1400
Std Dev = 59
Counts
Fitted Growth Time
0
200
400
600
800
1000
1200
1400
1600
600
700
800
900

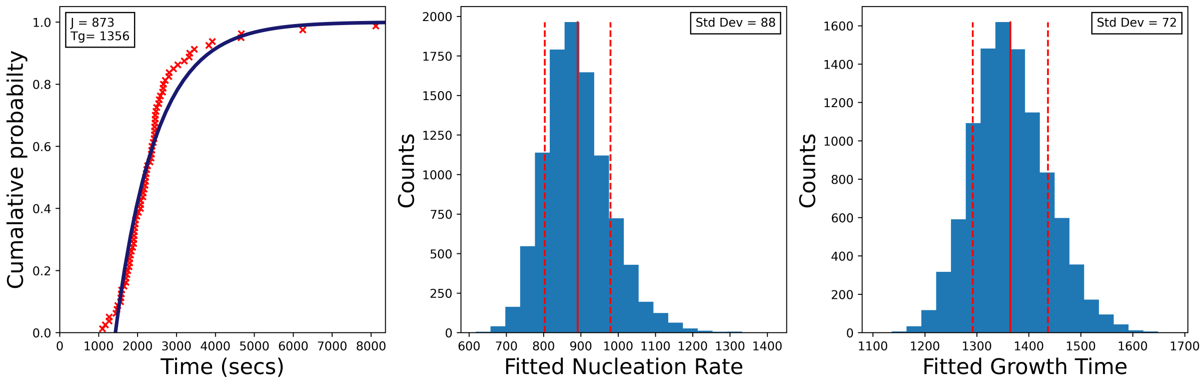
J = 873
Tg= 1356
Cumalative probabilty
Time (secs)
0.0
0.2
0.4
0.6
0.8
1.0
0
1000
2000
3000
4000
5000
6000
7000
8000
Std Dev = 88
Counts
Fitted Nucleation Rate
0
250
500
750
1000
1250
1500
1750
2000
600
700
800
900
1000
1100
1200
1300
1400
Std Dev = 72
Counts
Fitted Growth Time
0
200
400
600
800
1000
1200
1400
1600
1100
1200
1300
1400
1500
1600
1700

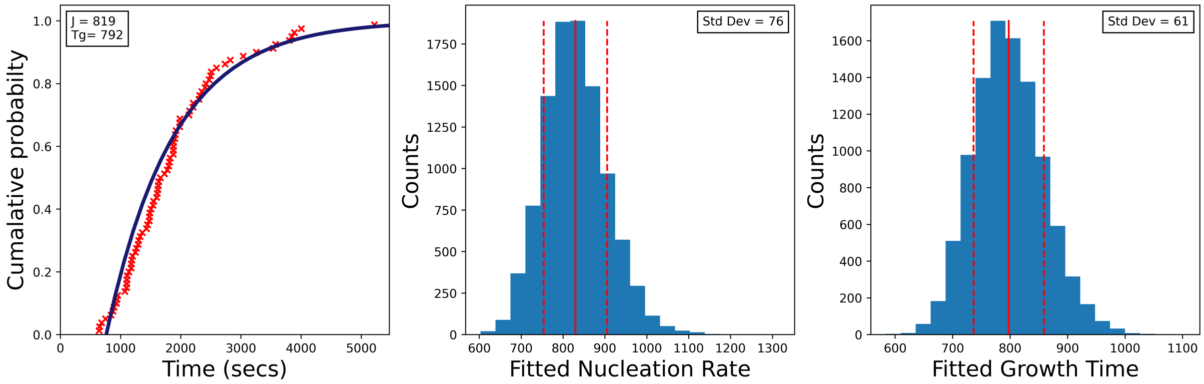
J = 819
Tg= 792
Cumalative probabilty
Time (secs)
0.0
0.2
0.4
0.6
0.8
1.0
0
1000
2000
3000
4000
5000
Std Dev = 76
Counts
Fitted Nucleation Rate
0
250
500
750
1000
1250
1500
1750
600
700
800
900
1000
1100
1200
1300
Std Dev = 61
Counts
Fitted Growth Time
0
200
400
600
800
1000
1200
1400
1600
600
700
800
900
1000
1100

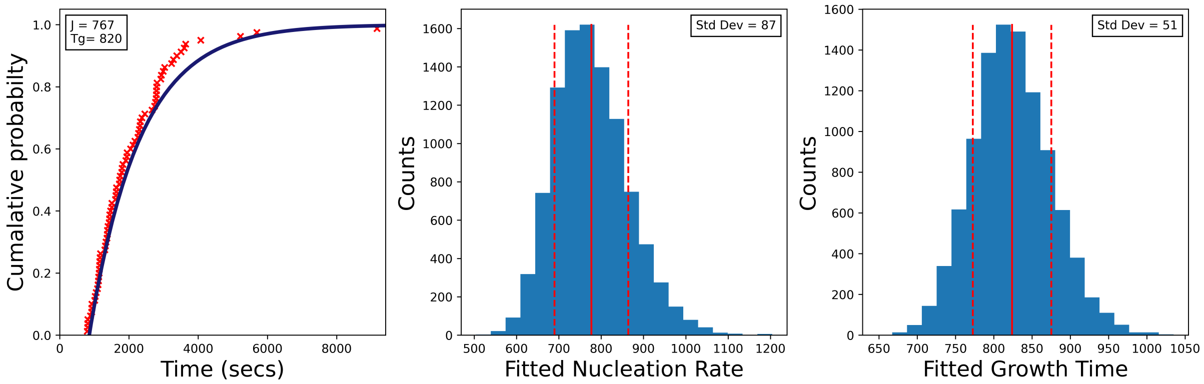
J = 767
Tg= 820
Cumalative probabilty
Time (secs)
0.0
0.2
0.4
0.6
0.8
1.0
0
2000
4000
6000
8000
Std Dev = 87
Counts
Fitted Nucleation Rate
0
200
400
600
800
1000
1200
1400
1600
500
600
700
800
900
1000
1100
1200
Std Dev = 51
Counts
Fitted Growth Time
0
200
400
600
800
1000
1200
1400
1600
650
700
750
800
850
900
950
1000
1050

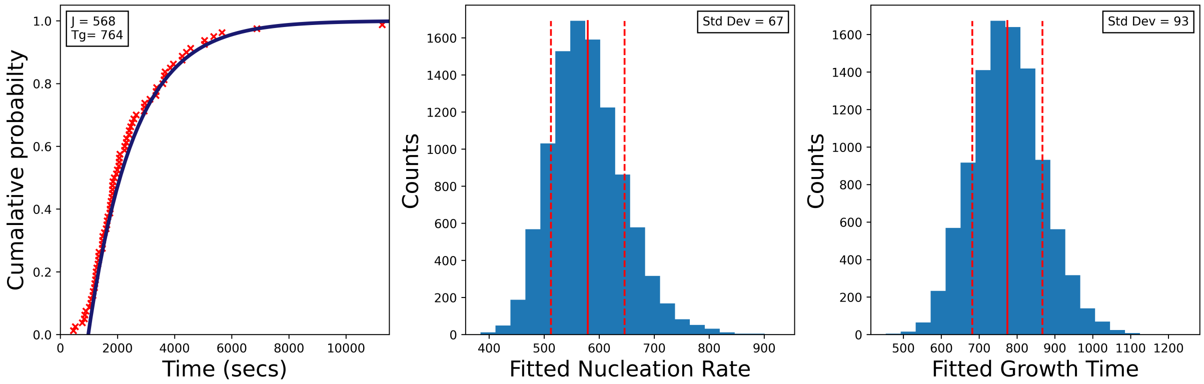
J = 568
Tg= 764
Cumalative probabilty
Time (secs)
0.0
0.2
0.4
0.6
0.8
1.0
0
2000
4000
6000
8000
10000
Std Dev = 67
Counts
Fitted Nucleation Rate
0
200
400
600
800
1000
1200
1400
1600
400
500
600
700
800
900
Std Dev = 93
Counts
Fitted Growth Time
0
200
400
600
800
1000
1200
1400
1600
500
600
700
800
900
1000
1100
1200

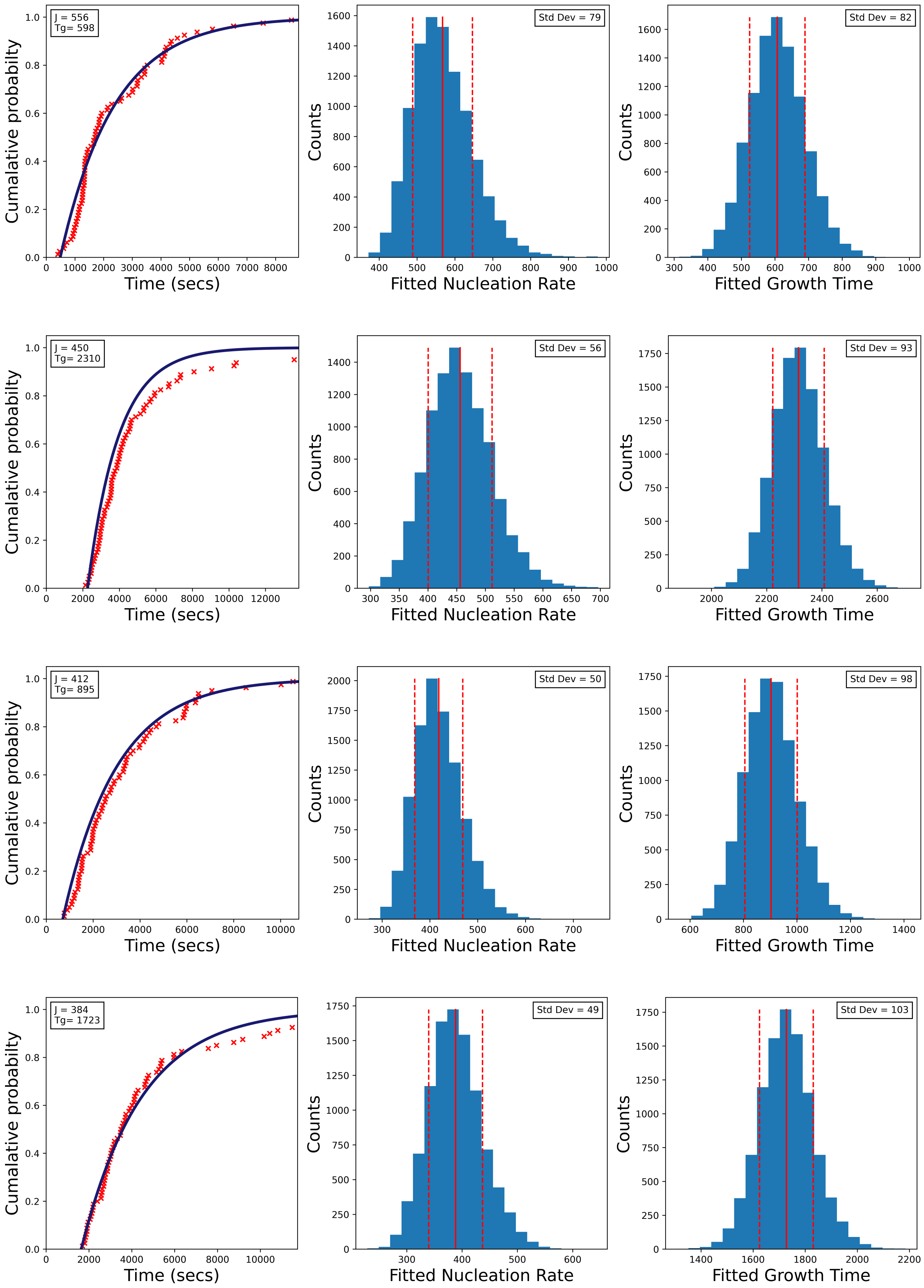
J = 556
Tg= 598
Std Dev = 79
Std Dev = 82
J = 450
Tg= 2310
Std Dev = 56
Std Dev = 93
J = 412
Tg= 895
Std Dev = 50
Std Dev = 98
J = 384
Tg= 1723
Std Dev = 49
Std Dev = 103
Cumalative probabilty
Time (secs)
Counts
Fitted Nucleation Rate
Fitted Growth Time

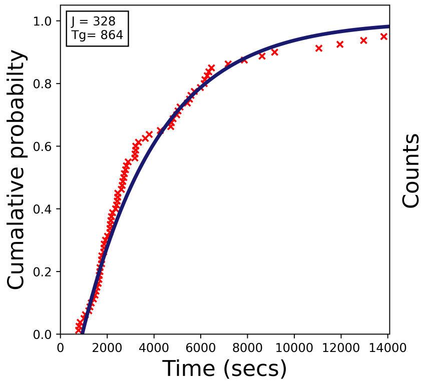
J = 328
Tg= 864
Cumalative probabilty
Time (secs)
0.0
0.2
0.4
0.6
0.8
1.0
0
2000
4000
6000
8000
10000
12000
14000

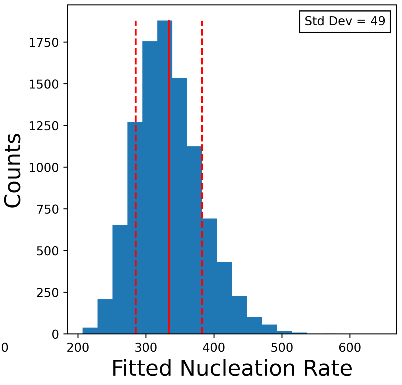
Std Dev = 49
Counts
Fitted Nucleation Rate
0
250
500
750
1000
1250
1500
1750
200
300
400
500
600

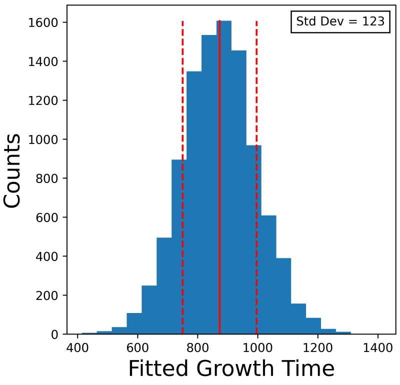
Std Dev = 123
Counts
Fitted Growth Time
0
200
400
600
800
1000
1200
1400
1600
400
600
800
1000
1200
1400

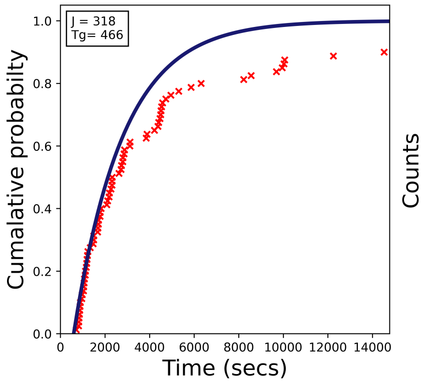
J = 318
Tg= 466
Cumalative probabilty
Time (secs)
0.0
0.2
0.4
0.6
0.8
1.0
0
2000
4000
6000
8000
10000
12000
14000

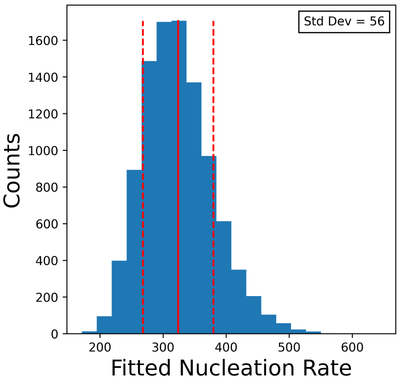
Std Dev = 56
Counts
Fitted Nucleation Rate
0
200
400
600
800
1000
1200
1400
1600
200
300
400
500
600

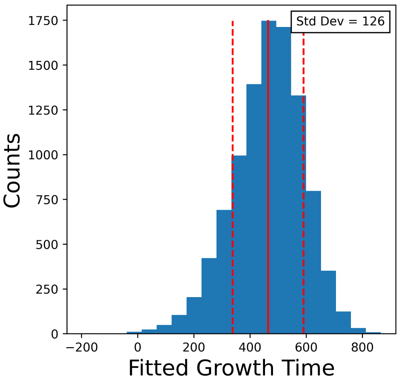
Std Dev = 126
Counts
Fitted Growth Time
0
250
500
750
1000
1250
1500
1750
−200
0
200
400
600
800

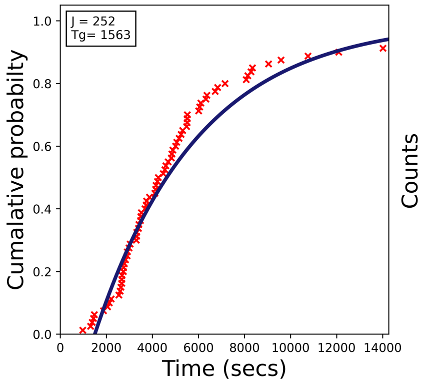
J = 252
Tg= 1563
Cumalative probabilty
Time (secs)
0.0
0.2
0.4
0.6
0.8
1.0
0
2000
4000
6000
8000
10000
12000
14000

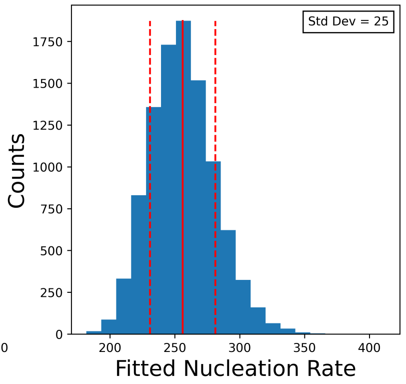
Std Dev = 25
Counts
Fitted Nucleation Rate
0
250
500
750
1000
1250
1500
1750
200
250
300
350
400

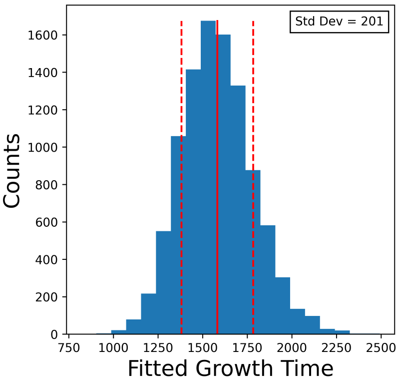
Std Dev = 201
Counts
Fitted Growth Time
0
200
400
600
800
1000
1200
1400
1600
750
1000
1250
1500
1750
2000
2250
2500

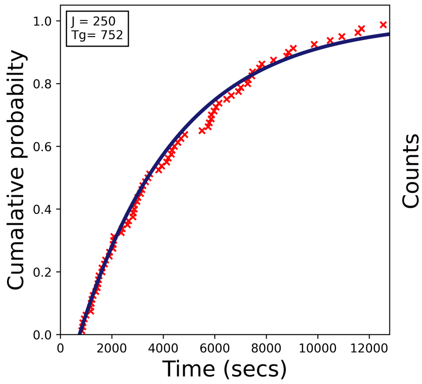
J = 250
Tg= 752
Cumalative probabilty
Time (secs)
0.0
0.2
0.4
0.6
0.8
1.0
0
2000
4000
6000
8000
10000
12000

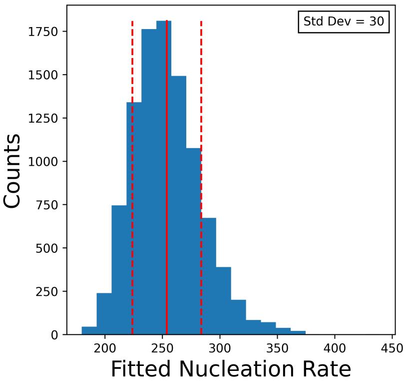
Std Dev = 30
Counts
Fitted Nucleation Rate
0
250
500
750
1000
1250
1500
1750
200
250
300
350
400
450

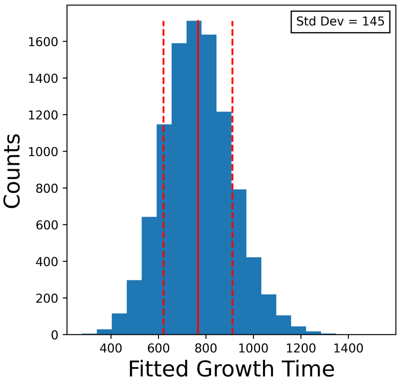
Std Dev = 145
Counts
Fitted Growth Time
0
200
400
600
800
1000
1200
1400
1600
400
600
800
1000
1200
1400

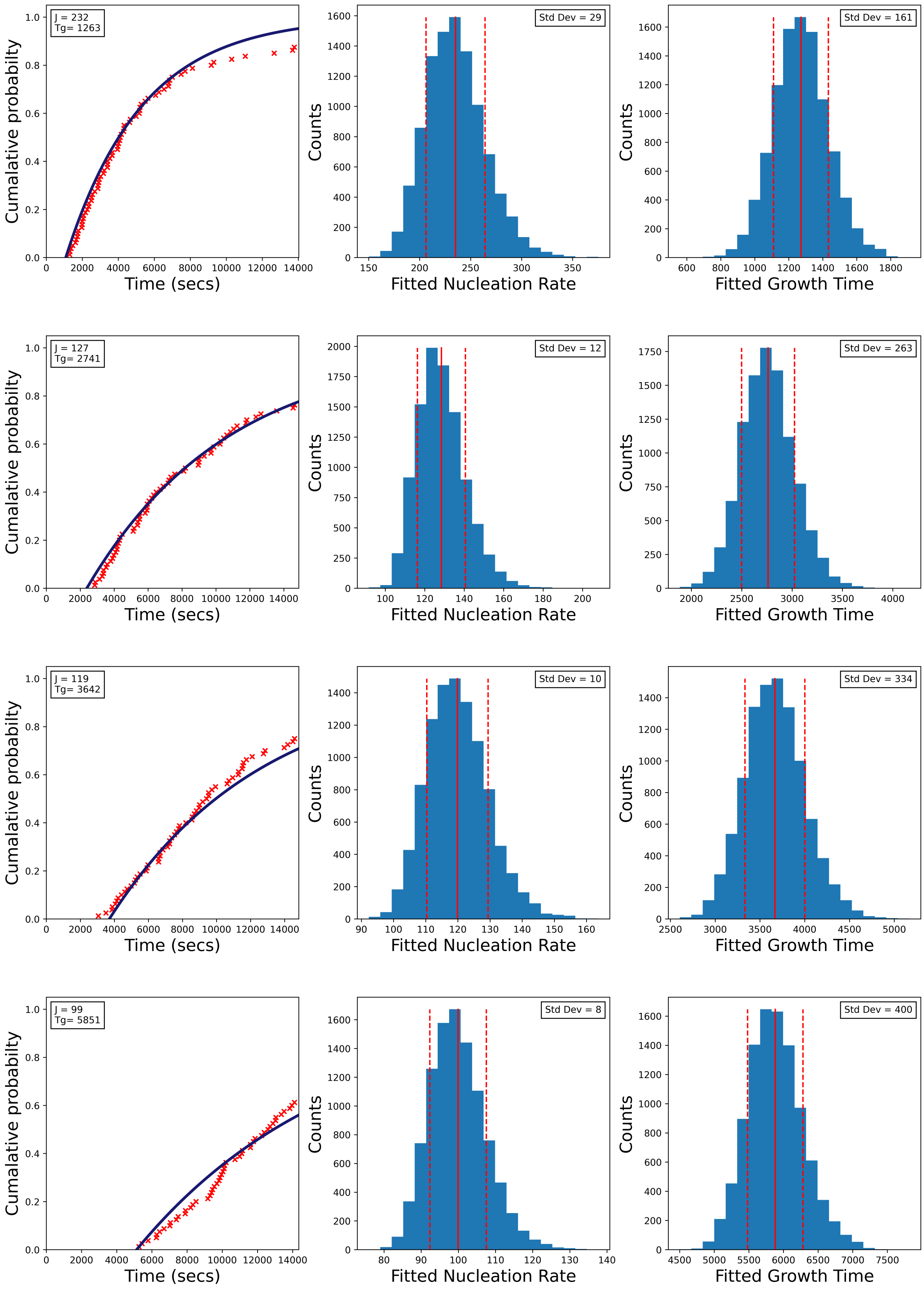
J = 232
Tg= 1263
Std Dev = 29
Std Dev = 161
J = 127
Tg= 2741
Std Dev = 12
Std Dev = 263
J = 119
Tg= 3642
Std Dev = 10
Std Dev = 334
J = 99
Tg= 5851
Std Dev = 8
Std Dev = 400
Cumalative probabilty
Time (secs)
Counts
Fitted Nucleation Rate
Fitted Growth Time
0.0
0.2
0.4
0.6
0.8
1.0
0
2000
4000
6000
8000
10000
12000
14000
150
200
250
300
350
600
800
1000
1200
1400
1600
1800
100
120
140
160
180
200
2500
3000
3500
4000
90
110
130
150
4500
5000
80
5500
6000
6500
7000
7500

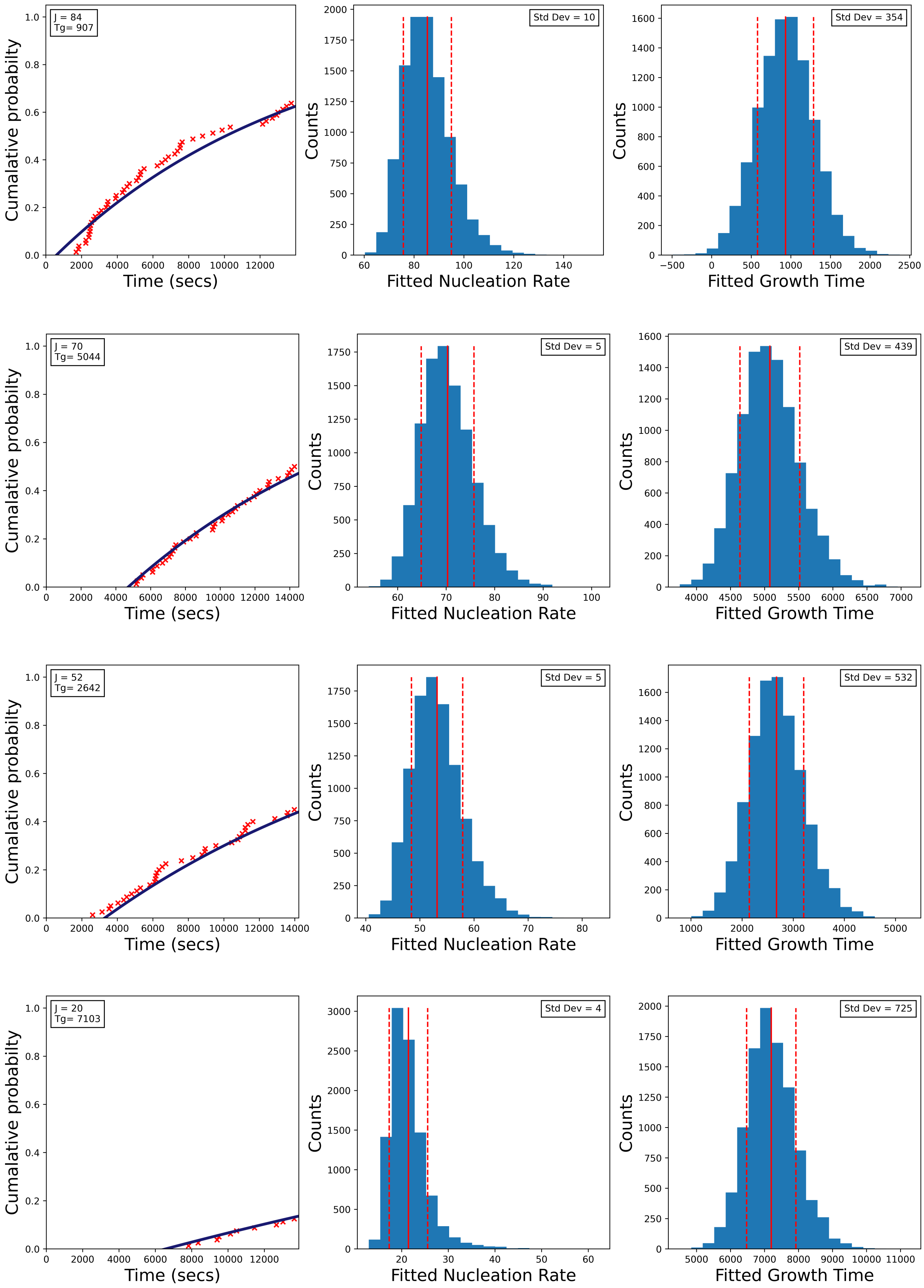
J = 84
Tg= 907
Cumalative probabilty
Time (secs)
Std Dev = 10
Counts
Fitted Nucleation Rate
Std Dev = 354
Counts
Fitted Growth Time
J = 70
Tg= 5044
Cumalative probabilty
Time (secs)
Std Dev = 5
Counts
Fitted Nucleation Rate
Std Dev = 439
Counts
Fitted Growth Time
J = 52
Tg= 2642
Cumalative probabilty
Time (secs)
Std Dev = 5
Counts
Fitted Nucleation Rate
Std Dev = 532
Counts
Fitted Growth Time
J = 20
Tg= 7103
Cumalative probabilty
Time (secs)
Std Dev = 4
Counts
Fitted Nucleation Rate
Std Dev = 725
Counts
Fitted Growth Time

8.2 All attempted fittings of nucleation rate data.

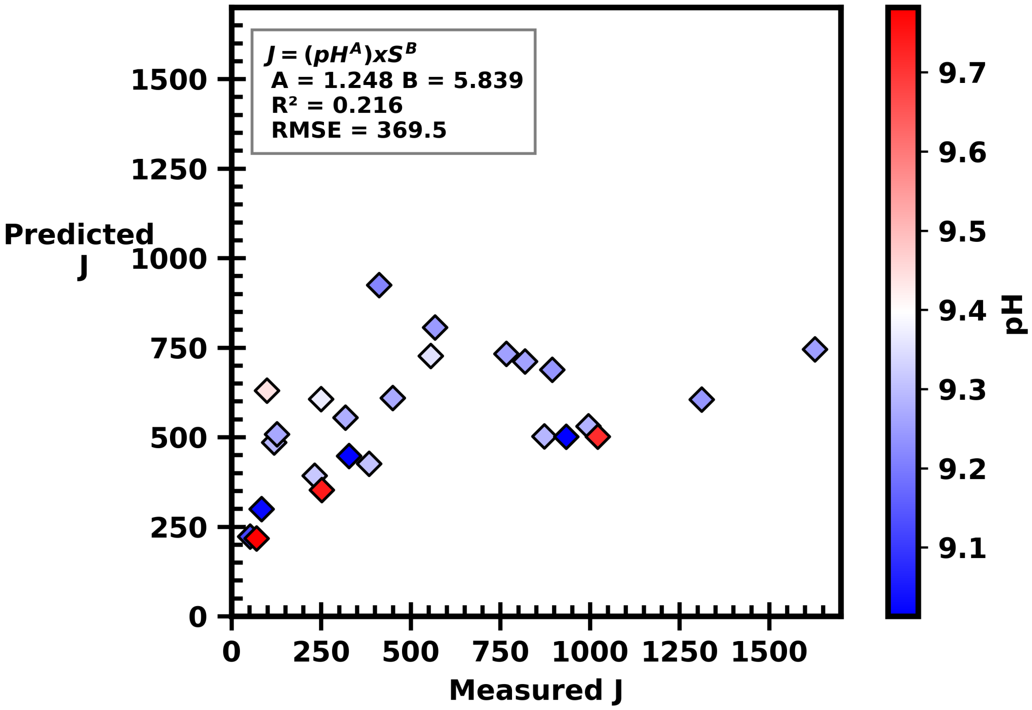

Figure 8.2: pH term included in the power law fitting.

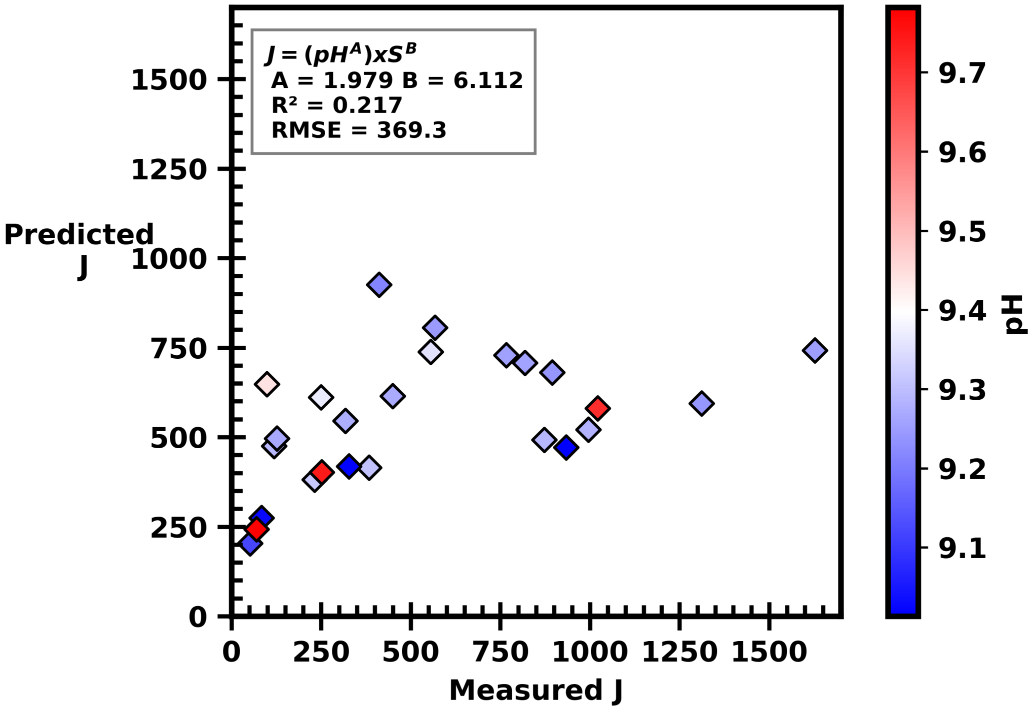

Figure 8.3: pH term included in the power law fitting. $S = S\gamma$

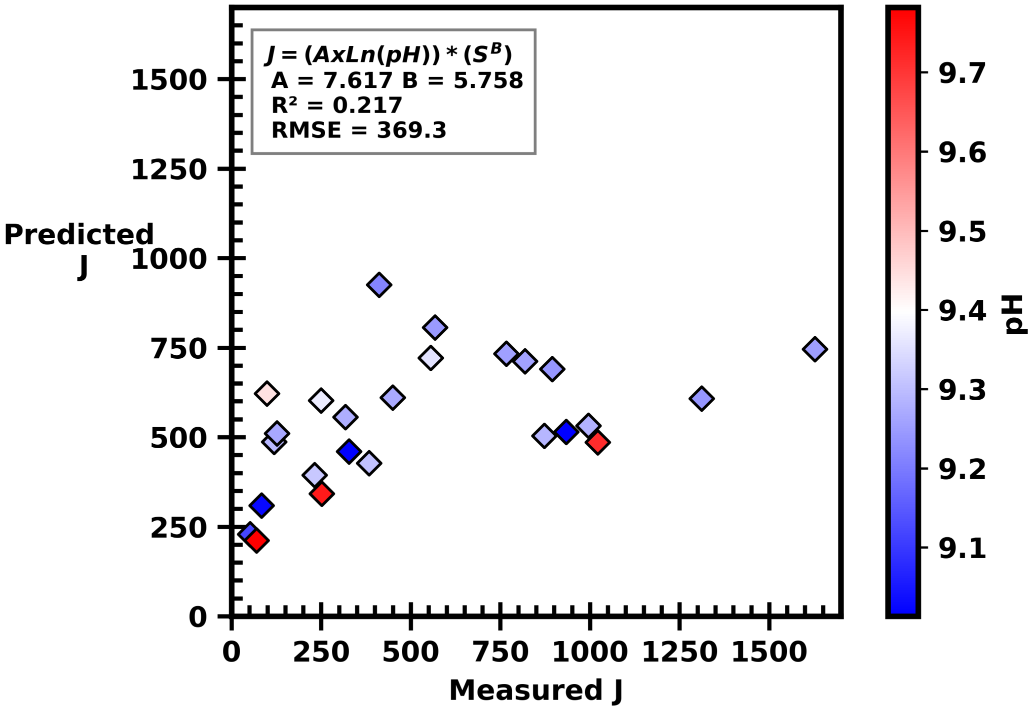

Figure 8.4: Natural log pH term included in the power law fitting.

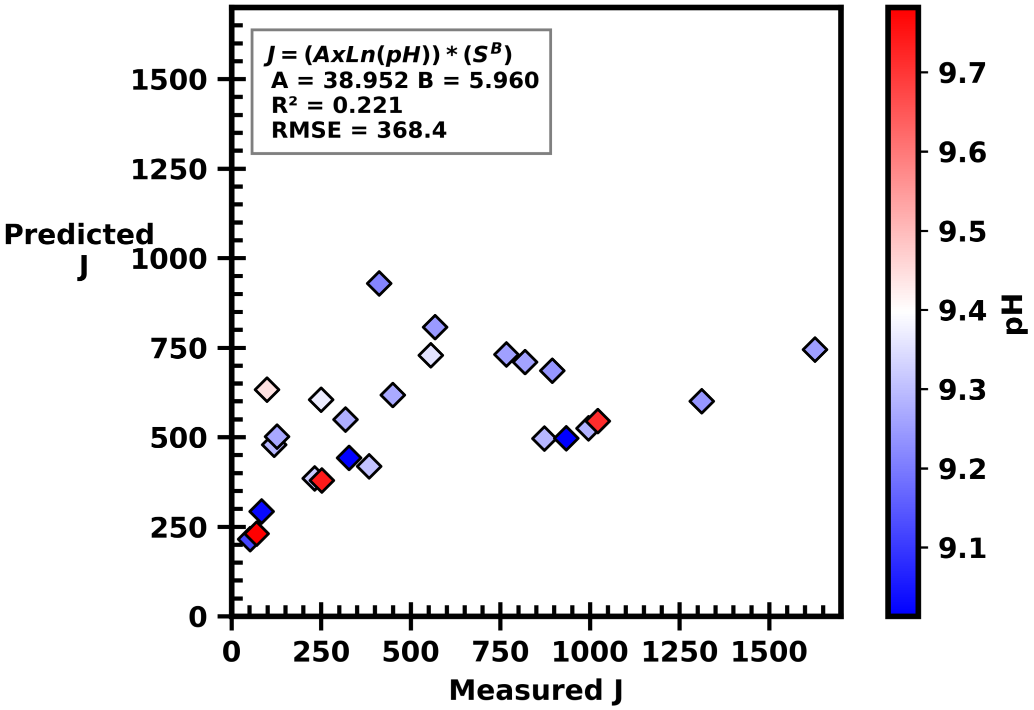

Figure 8.5: Natural log pH term included in the power law fitting. $S = S\gamma$

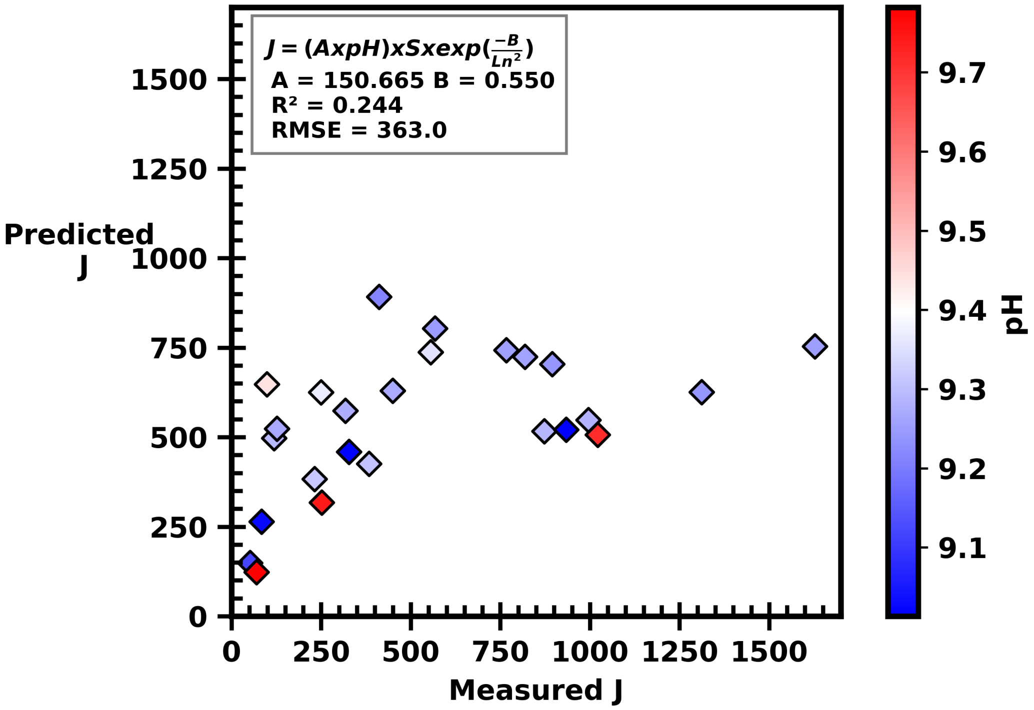

Figure 8.6: KJMA equation directly fitted incorporating pH into the pre-exponential term.

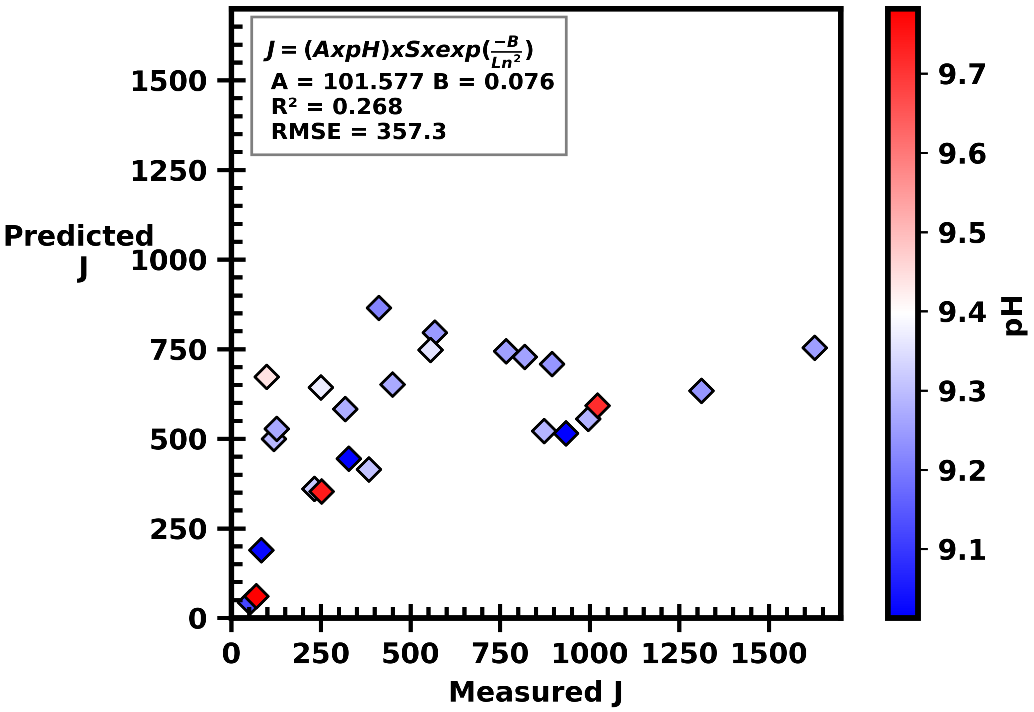

Figure 8.7: KJMA equation directly fitted incorporating pH into the pre-exponential term. $S = S\gamma$

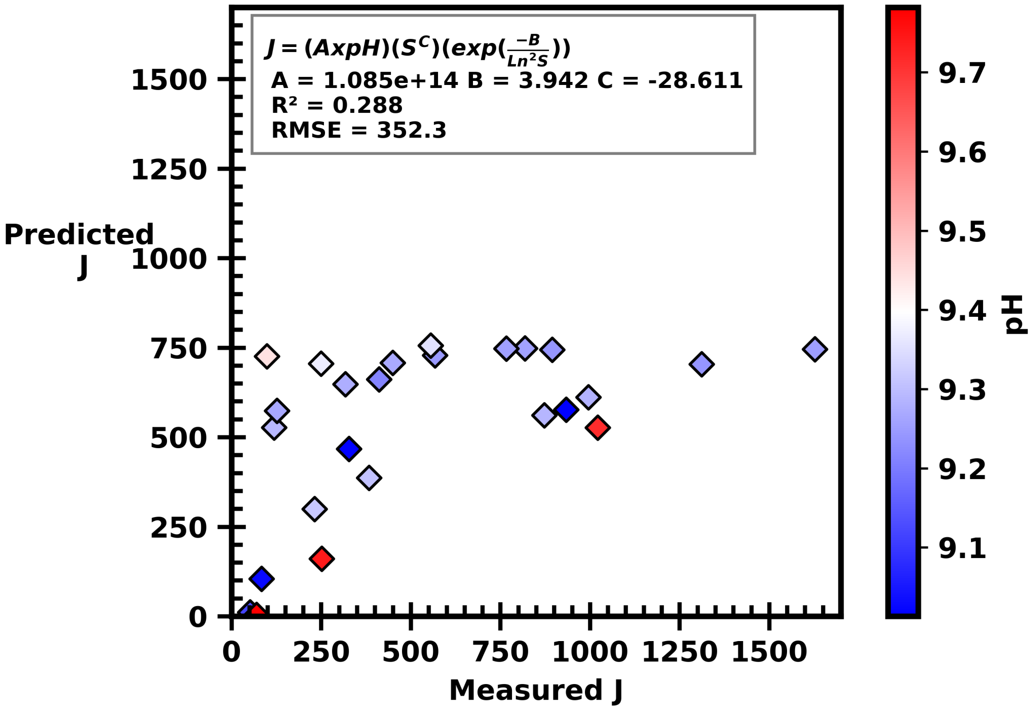

Figure 8.8: MNT equation directly fitted incorporating pH into the pre-exponential term.

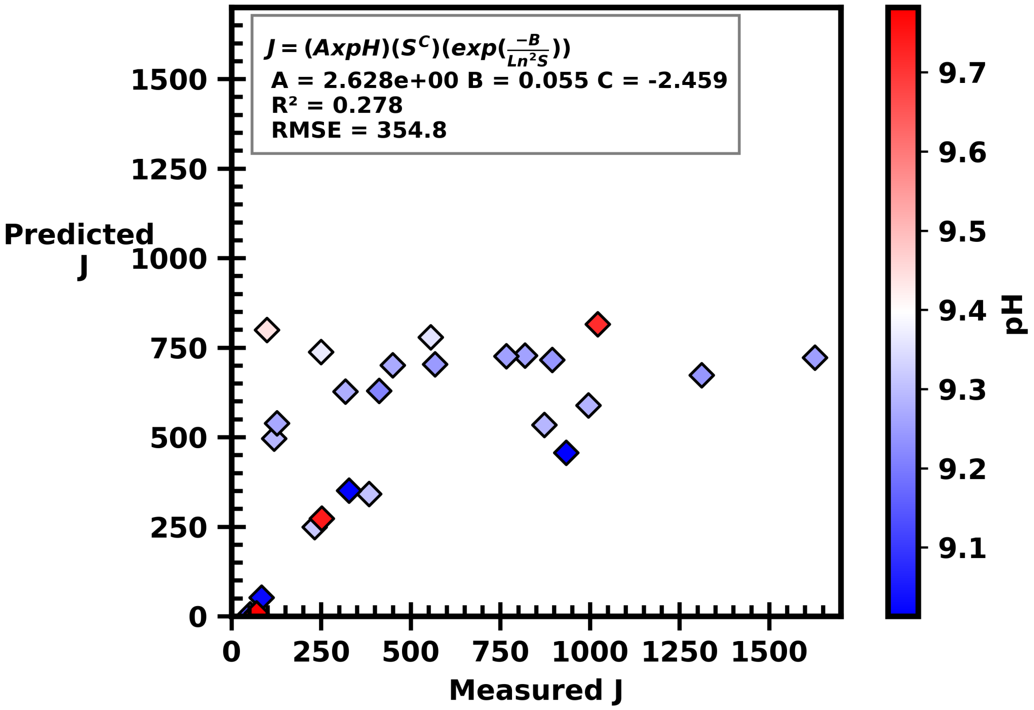

Figure 8.9: MNT equation directly fitted incorporating pH into the pre-exponential term. $S = S\gamma$